NAVAL POSTGRADUATE SCHOOL
MONTEREY, CALIFORNIA

DTIC
S ELECTE D
APR 27 1995
F

THESIS

ANALYTIC AND EXPERIMENTAL INVESTIGATION OF ROTORDYNAMIC RESPONSE AND BACKWARD WHIRL INDUCED BY SPLIT RESONANCE

by

Curtis E. Vejvoda

December, 1994

Thesis Advisor: Knox T. Millsaps Jr.

Approved for public release; distribution is unlimited.

DTIC QUALITY INSPECTED 5

19950426 117

REPORT DOCUMENTATION PAGE

Form Approved OMB No. 0704-0188

Public reporting burden for this collection of information is estimated to average 1 hour per response, including the time for reviewing instruction, searching existing data sources, gathering and maintaining the data needed, and completing and reviewing the collection of information. Send comments regarding this burden estimate or any other aspect of this collection of information, including suggestions for reducing this burden, to Washington Headquarters Services, Directorate for Information Operations and Reports, 1215 Jefferson Davis Highway, Suite 1204, Arlington, VA 22202-4302, and to the Office of Management and Budget, Paperwork Reduction Project (0704-0188) Washington DC 20503.

1. AGENCY USE ONLY *(Leave blank)*

2. REPORT DATE
December 1994

3. REPORT TYPE AND DATES COVERED
Master's Thesis

4. TITLE AND SUBTITLE ANALYTIC AND EXPERIMENTAL INVESTIGATION OF ROTORDYNAMIC RESPONSE AND BACKWARD WHIRL INDUCED BY SPLIT RESONANCE

5. FUNDING NUMBERS

6. AUTHOR(S) Curtis E. Vejvoda

7. PERFORMING ORGANIZATION NAME(S) AND ADDRESS(ES)
Naval Postgraduate School
Monterey CA 93943-5000

8. PERFORMING ORGANIZATION REPORT NUMBER

9. SPONSORING/MONITORING AGENCY NAME(S) AND ADDRESS(ES)

10. SPONSORING/MONITORING AGENCY REPORT NUMBER

11. SUPPLEMENTARY NOTES The views expressed in this thesis are those of the author and do not reflect the official policy or position of the Department of Defense or the U.S. Government.

12a. DISTRIBUTION/AVAILABILITY STATEMENT
Approved for public release; distribution is unlimited.

12b. DISTRIBUTION CODE

13. ABSTRACT *(maximum 200 words)*

Rotordynamic response phenomena, including backward whirl, were investigated both analytically and experimentally. A two degree-of-freedom rotor model was developed to simulate the steady state, lateral vibration characteristics of a simply supported, single disk rotor. This model includes the effects of direct and cross-coupled, linear damping and stiffness coefficients. The computer model was used to quantify the influence of bearing characteristics on rotordynamic response. The presence of split resonance, which appears to be due to separate and distinct natural frequencies in the two orthogonal lateral directions and the occurence of backward whirl between these two frequencies was studied. The effects of geometric imperfections in the bearing sleeve, gravitational forces and bearing support stiffnesses were isolated using the experimental apparatus. It was determined that the split resonance induced backward whirl and the different natural frequencies were caused by asymmetric stiffness of the bearing support structure as well as gravitational forces. Bearing imperfections did not create the backward whirl phenomena. The bearing support characteristics necessary to create the observed rotor orbits were determined.

14. SUBJECT TERMS

15. NUMBER OF PAGES 135

16. PRICE CODE

17. SECURITY CLASSIFICATION OF REPORT
Unclassified

18. SECURITY CLASSIFICATION OF THIS PAGE
Unclassified

19. SECURITY CLASSIFICATION OF ABSTRACT
Unclassified

20. LIMITATION OF ABSTRACT
UL

Approved for public release; distribution is unlimited

ANALYTIC AND EXPERIMENTAL INVESTIGATION OF ROTORDYNAMIC RESPONSE AND BACKWARD WHIRL INDUCED BY SPLIT RESONANCE

Curtis E. Vejvoda
Lieutenant, United States Navy
B.S., California Maritime Academy, 1986

Submitted in partial fulfillment of the
requirements for the degree of

MASTER OF SCIENCE IN MECHANICAL ENGINEERING
AND
MECHANICAL ENGINEER

from the

NAVAL POSTGRADUATE SCHOOL
December 1994

Author: Curtis E. Vejvoda

Approved by: Knox T. Millsaps, Jr., Thesis Advisor

Matthew D. Kelleher, Chairman,
Department of Mechanical Engineering

Accesion For
NTIS CRA&I ☑
DTIC TAB ☐
Unannounced ☐
Justification
By
Distribution /
Availability Codes
Dist | Avail and / or Special
A-1

ABSTRACT

Rotordynamic response phenomena, including backward whirl, were investigated both analytically and experimentally. A two degree-of-freedom rotor model was developed to simulate the steady state, lateral vibration characteristics of a simply supported, single disk rotor. This model includes the effects of direct and cross-coupled, linear damping and stiffness coefficients. The computer model was used to quantify the influence of bearing characteristics on rotordynamic response. The presence of split resonance, which appears to be due to separate and distinct natural frequencies in the two orthogonal lateral directions and the occurence of backward whirl between these two frequencies was studied. The effects of geometric imperfections in the bearing sleeve, gravitational forces and bearing support stiffnesses were isolated using the experimental apparatus. It was determined that the split resonance induced backward whirl and the different natural frequencies were caused by asymmetric stiffness of the bearing support structure as well as gravitational forces. Bearing imperfections did not create the backward whirl phenomena. The bearing support characteristics necessary to create the observed rotor orbits were determined.

TABLE OF CONTENTS

I. INTRODUCTION 1

II. BACKGROUND... 7

III. ANALYTIC MODEL 9

A. $K_{XX} = 495$, $K_{YY} = 495$, $C_{XX} = .025$, $C_{YY} = .025$....................... 14

B. $K_{XX} = 535$, $K_{YY} = 555$, $C_{XX} = .025$, $C_{YY} = .025$....................... 15

C. $K_{XX} = 535$, $K_{YY} = 535$, $C_{XX} = .035$, $C_{YY} = .02$........................ 15

D. $K_{XX} = 535$, $K_{YY} = 555$, $C_{XX} = .04$, $C_{YY} = .02$.......................... 16

E. $K_{XX} = 535$, $K_{YY} = 575$, $C_{XX} = .04$, $C_{YY} = .025$........................ 16

F. $K_{XX}=535$, $K_{YY}=535$, $K_{XY}=40$, $K_{YX}=10$, $C_{XX}=.025$, $C_{YY}=.025$... 16

G. $K_{XX}=535$, $K_{YY}=535$, $K_{XY}=10$, $K_{YX}=40$, $C_{XX}=.025$, $C_{YY}=.025$... 17

H. $K_{XX}=535$, $K_{YY}=535$, $C_{XX}=.025$, $C_{YY}=.025$, $C_{XY}=-.02$, $C_{YX}=-.01$ 17

I. $K_{XX}=535$, $K_{YY}=535$, $C_{XX}=.025$, $C_{YY}=.025$, $C_{XY}=.02$, $C_{YX}=.01$. 18

J. $K_{XX}=535$, $K_{YY}=555$, $K_{XY}=-5$, $K_{YX}=3$, $C_{XX}=.025$, $C_{YY}=.025$..... 18

IV. EXPERIMENTAL INVESTIGATION... 19

A. GOOD BEARING TABLE MOUNT.. 22

1. Good Bearing No Imbalance 22

2. Good Bearing 0.5 Gram Imbalance.. 22

3. Good Bearing 1.0 Gram Imbalance.. 23

4. Good Bearing 1.6 Gram Imbalance.. 23

B. BAD BEARING TABLE MOUNT.. 24

1. Vertical Bad Bearing 1.0 Gram Imbalance............................... 24

2. Horizontal Bad Bearing 1.0 Gram Imbalance 25

        3. 45 Degrees Left Bad Bearing 1.0 Gram Imbalance 25
        4. 45 Degrees Right Bad Bearing 1.0 Gram Imbalance 25
    C. HORIZONTAL SHAFT MOUNT 1.0 GRAM IMBALANCE.............. 26
    D. VERTICAL SHAFT MOUNT 1.0 GRAM IMBALANCE 26

V. DISCUSSION OF RESULTS.. 29

VI. CONCLUSIONS AND RECOMMENDATIONS 33
    A. CONCLUSIONS 33
    B. RECOMMENDATIONS.. 34

APPENDIX A: LIST OF DIMENSIONS AND PROPERTIES 37

APPENDIX B: ANALYTIC ROTOR DATA... 39

APPENDIX C: EXPERIMENTAL ROTOR DATA..................................... 59

LIST OF REFERENCES..115

INITIAL DISTRIBUTION LIST...117

LIST OF FIGURES

Figure 1. Rotor and Disk Assembly in Forward Whirl 3

Figure 2. Rotor and Disk Assembly in Backward Whirl 4

Figure 3. Analytic Lumped Mass and Stiffness Model of Two Degree-of-Freedom Rotating Shaft and Disk Assembly 9

Figure 4. Analytic Pinned-Pinned Model of Shaft and Disk Assembly 13

Figure 5. Configuration of Experimental Rotor System 21

Figure 6. Rotor Orbits and Displacements From Analytic Model For Kxx = 495 lbf/in, Kyy = 495 lbf/in, Kxy = 0 lbf/in, Kyx = 0 lbf/in, Cxx = .025, Cyy = .025, Cxy = 0, Cyx = 0 39

Figure 7. Cascade Plot and Phase Diagram From Analytic Model For Kxx = 495 lbf/in, Kyy = 495 lbf/in, Kxy = 0 lbf/in, Kyx = 0 lbf/in, Cxx = .025, Cyy = .025, Cxy = 0, Cyx = 0 40

Figure 8. Rotor Orbits and Displacements From Analytic Model For Kxx = 535 lbf/in, Kyy = 555 lbf/in, Kxy = 0 lbf/in, Kyx = 0 lbf/in, Cxx = .025, Cyy = .025, Cxy = 0, Cyx = 0 41

Figure 9. Cascade Plot and Phase Diagram From Analytic Model For Kxx = 535 lbf/in, Kyy = 555 lbf/in, Kxy = 0 lbf/in, Kyx = 0 lbf/in, Cxx = .025, Cyy = .025, Cxy = 0, Cyx = 0 42

Figure 10. Rotor Orbits and Displacements From Analytic Model For Kxx = 535 lbf/in, Kyy = 535 lbf/in, Kxy = 0 lbf/in, Kyx = 0 lbf/in, Cxx = .035, Cyy = .02, Cxy = 0, Cyx = 0 43

Figure 11. Cascade Plot and Phase Diagram From Analytic Model For Kxx = 535 lbf/in, Kyy = 535 lbf/in, Kxy = 0 lbf/in, Kyx = 0 lbf/in, Cxx = .035, Cyy = .02, Cxy = 0, Cyx = 0 44

Figure 12. Rotor Orbits and Displacements From Analytic Model For Kxx = 535 lbf/in, Kyy = 555 lbf/in, Kxy = 0 lbf/in, Kyx = 0 lbf/in, Cxx = .04, Cyy = .02, Cxy = 0, Cyx = 0 45

Figure 13. Cascade Plot and Phase Diagram From Analytic Model For Kxx = 535 lbf/in, Kyy = 555 lbf/in, Kxy = 0 lbf/in, Kyx = 0 lbf/in, Cxx = .04, Cyy = .02, Cxy = 0, Cyx = 0 46

Figure 14. Rotor Orbits and Displacements From Analytic Model For Kxx = 535 lbf/in, Kyy = 575 lbf/in, Kxy = 0 lbf/in, Kyx = 0 lbf/in, Cxx = .04, Cyy = .025, Cxy = 0, Cyx = 0 47

Figure 15. Cascade Plot and Phase Diagram From Analytic Model For Kxx = 535 lbf/in, Kyy = 575 lbf/in, Kxy = 0 lbf/in, Kyx = 0 lbf/in, Cxx = .04, Cyy = .025, Cxy = 0, Cyx = 0 48

Figure 16. Rotor Orbits and Displacements From Analytic Model For Kxx = 535 lbf/in, Kyy = 535 lbf/in, Kxy = 40 lbf/in, Kyx = 10 lbf/in, Cxx = .025, Cyy = .025, Cxy = 0, Cyx = 0 49

Figure 17. Cascade Plot and Phase Diagram From Analytic Model For Kxx = 535 lbf/in, Kyy = 535 lbf/in, Kxy = 40 lbf/in, Kyx = 10 lbf/in, Cxx = .025, Cyy = .025, Cxy = 0, Cyx = 0 50

Figure 18. Rotor Orbits and Displacements From Analytic Model For Kxx = 535 lbf/in, Kyy = 535 lbf/in, Kxy = 10 lbf/in, Kyx = 40 lbf/in, Cxx = .025, Cyy = .025, Cxy = 0, Cyx = 0 51

Figure 19. Cascade Plot and Phase Diagram From Analytic Model For Kxx = 535 lbf/in, Kyy = 535 lbf/in, Kxy = 10 lbf/in, Kyx = 40 lbf/in, Cxx = .025, Cyy = .025, Cxy = 0, Cyx = 0 52

Figure 20. Rotor Orbits and Displacements From Analytic Model For Kxx = 535 lbf/in, Kyy = 535 lbf/in, Kxy = 0 lbf/in, Kyx = 0 lbf/in, Cxx = .025, Cyy = .025, Cxy = -.02, Cyx = -.01 53

Figure 21. Cascade Plot and Phase Diagram From Analytic Model For Kxx = 535 lbf/in, Kyy = 535 lbf/in, Kxy = 0 lbf/in, Kyx = 0 lbf/in, Cxx = .025, Cyy = .025, Cxy = -.02, Cyx = -.01 54

Figure 22. Rotor Orbits and Displacements From Analytic Model For Kxx = 535 lbf/in, Kyy = 535 lbf/in, Kxy = 0 lbf/in, Kyx = 0 lbf/in, Cxx = .025, Cyy = .025, Cxy = .02, Cyx = .01 55

Figure 23. Cascade Plot and Phase Diagram From Analytic Model For Kxx = 535 lbf/in, Kyy = 535 lbf/in, Kxy = 0 lbf/in, Kyx = 0 lbf/in, Cxx = .025, Cyy = .025, Cxy = .02, Cyx = .01 56

Figure 24. Rotor Orbits and Displacements From Analytic Model For Kxx = 535 lbf/in, Kyy = 555 lbf/in, Kxy = -5 lbf/in, Kyx = 3 lbf/in, Cxx = .025, Cyy = .025, Cxy = 0, Cyx = 0 57

Figure 25. Cascade Plot and Phase Diagram From Analytic Model For Kxx = 535 lbf/in, Kyy = 555 lbf/in, Kxy = -5 lbf/in, Kyx = 3 lbf/in, Cxx = .025, Cyy = .025, Cxy = 0, Cyx = 0 58

Figure 26. Rotor Orbits No Imbalance Good Bearing. Speeds from 2760 to 2900 rpm. 59

Figure 27. Rotor Orbits No Imbalance Good Bearing. Speeds from 2920 to 3200 rpm. 60

Figure 28. Rotor Orbits No Imbalance Good Bearing. Speeds from 5600 to 6200 rpm. 61

Figure 29. Maximum Displacements and Bode Plot No Imbalance Good Bearing 62

Figure 30. Cascade Plot No Imbalance Good Bearing 63

Figure 31. Rotor Orbits 0.5 Gram Imbalance Good Bearing. Speeds from 2760 to 2900 rpm.......... 64

Figure 32. Rotor Orbits 0.5 Gram Imbalance Good Bearing. Speeds from 2920 to 3200 rpm.......... 65

Figure 33. Rotor Orbits 0.5 Gram Imbalance Good Bearing. Speeds from 5600 to 6200 rpm.......... 66

Figure 34. Maximum Displacements and Bode Plot 0.5 Gram Imbalance Good Bearing........ 67
Figure 35. Cascade Plot 0.5 Gram Imbalance Good Bearing........ 68
Figure 36. Rotor Orbits 1.0 Gram Imbalance Good Bearing. Speeds from 2760 to 2860 rpm........ 69
Figure 37. Rotor Orbits 1.0 Gram Imbalance Good Bearing. Speeds from 2880 to 3200 rpm........ 70
Figure 38. Rotor Orbits 1.0 Gram Imbalance Good Bearing. Speeds from 5600 to 5900 rpm........ 71
Figure 39. Rotor Orbits 1.0 Gram Imbalance Good Bearing. Speeds from 6000 to 6200 rpm........ 72
Figure 40. Maximum Displacements and Bode Plot 1.0 Gram Imbalance Good Bearing........ 73
Figure 41. Cascade Plot 1.0 Gram Imbalance Good Bearing........ 74
Figure 42. Rotor Orbits 1.6 Gram Imbalance Good Bearing. Speeds from 2600 to 2830 rpm........ 75
Figure 43. Rotor Orbits 1.6 Gram Imbalance Good Bearing. Speeds from 2860 to 2940 rpm........ 76
Figure 44. Rotor Orbits 1.6 Gram Imbalance Good Bearing. Speeds from 3000 to 3200 rpm........ 77
Figure 45. Rotor Orbits 1.6 Gram Imbalance Good Bearing. Speeds from 5600 to 5900 rpm........ 78
Figure 46. Rotor Orbits 1.6 Gram Imbalance Good Bearing. Speeds from 6000 to 6200 rpm........ 79
Figure 47. Maximum Displacements and Bode Plot 1.6 Gram Imbalance Good Bearing........ 80
Figure 48. Cascade Plot 1.6 Gram Imbalance Good Bearing........ 81
Figure 49. Rotor Orbits 1.0 Gram Imbalance Elongated Bearing with Elongation In the Vertical Direction. Speeds from 2780 to 2860 rpm........ 82
Figure 50. Rotor Orbits 1.0 Gram Imbalance Elongated Bearing with Elongation In the Vertical Direction. Speeds from 2900 to 3200 rpm........ 83
Figure 51. Rotor Orbits 1.0 Gram Imbalance Elongated Bearing with Elongation In the Vertical Direction. Speeds from 5000 to 5800 rpm........ 84
Figure 52. Rotor Orbits 1.0 Gram Imbalance Elongated Bearing with Elongation In the Vertical Direction. Speeds from 5900 to 6000 rpm........ 85
Figure 53. Maximum Displacements and Bode Plot 1.0 Gram Imbalance Elongated Bearing with Elongation In the Vertical Direction........ 86
Figure 54. Cascade Plot 1.0 Gram Imbalance Elongated Bearing with Elongation In the Vertical Direction........ 87

Figure 55. Rotor Orbits 1.0 Gram Imbalance Elongated Bearing with Elongation In the Horizontal Direction. Speeds from 2780 to 2860 rpm. 88

Figure 56. Rotor Orbits 1.0 Gram Imbalance Elongated Bearing with Elongation In the Horizontal Direction. Speeds from 2900 to 3200 rpm. 89

Figure 57. Rotor Orbits 1.0 Gram Imbalance Elongated Bearing with Elongation In the Horizontal Direction. Speeds from 5000 to 5800 rpm. 90

Figure 58. Maximum Displacements and Bode Plot 1.0 Gram Imbalance Elongated Bearing with Elongation In the Horizontal Direction............ 91

Figure 59. Cascade Plot 1.0 Gram Imbalance Elongated Bearing with Elongation In the Horizontal Direction.. 92

Figure 60. Rotor Orbits 1.0 Gram Imbalance Elongated Bearing with Elongation In the Direction of the Resonant Displacement (45 Degrees off vertical). Speeds from 2780 to 2860 rpm. 93

Figure 61. Rotor Orbits 1.0 Gram Imbalance Elongated Bearing with Elongation In the Direction of the Resonant Displacement (45 Degrees off vertical). Speeds from 2900 to 3200 rpm. 94

Figure 62. Rotor Orbits 1.0 Gram Imbalance Elongated Bearing with Elongation In the Direction of the Resonant Displacement (45 Degrees off vertical). Speeds from 5600 to 5800 rpm. 95

Figure 63. Rotor Orbits 1.0 Gram Imbalance Elongated Bearing with Elongation In the Direction of the Resonant Displacement (45 Degrees off vertical). Speeds from 5900 to 6200 rpm. 96

Figure 64. Maximum Displacements and Bode Plot for 1.0 Gram Imbalance Elongated Bearing with Elongation In the Direction of the Resonant Displacement (45 Degrees off vertical).. 97

Figure 65. Cascade Plot 1.0 Gram Imbalance Elongated Bearing with Elongation In the Direction of the Resonant Displacement (45 Degrees off vertical).. 98

Figure 66. Rotor Orbits 1.0 Gram Imbalance Elongated Bearing with Elongation Perpendicular to Direction of Resonant Displacement (45 Degrees off Vertical). Speeds from 2780 to 2860 rpm.................................... 99

Figure 67. Rotor Orbits 1.0 Gram Imbalance Elongated Bearing with Elongation Perpendicular to Direction of Resonant Displacement (45 Degrees off Vertical). Speeds from 2900 to 3200 rpm...................................100

Figure 68. Rotor Orbits 1.0 Gram Imbalance Elongated Bearing with Elongation Perpendicular to Direction of Resonant Displacement (45 Degrees off Vertical). Speeds from 5600 to 6000 rpm...................................101

Figure 69. Maximum Displacements and Bode Plot for 1.0 Gram Imbalance Elongated Bearing with Elongation Perpendicular to Direction of Resonant Displacement (45 Degrees off Vertical)..........................102

Figure 70. Cascade Plot 1.0 Gram Imbalance Elongated Bearing with Elongation Perpendicular to Direction of Resonant Displacement (45 Degrees off Vertical)...103

Figure 71. Rotor Orbits 1.0 Gram Imbalance Shaft Mounted Horizontal. Speeds from 2760 to 2880 rpm. 104
Figure 72. Rotor Orbits 1.0 Gram Imbalance Shaft Mounted Horizontal. Speeds from 2900 to 3200 rpm. 105
Figure 73. Rotor Orbits 1.0 Gram Imbalance Shaft Mounted Horizontal. Speeds from 5600 to 6000 rpm. 106
Figure 74. Maximum Displacements and Bode Plot for 1.0 Gram Imbalance Shaft Mounted Horizontal. 107
Figure 75. Cascade Plot 1.0 Gram Imbalance Shaft Mounted Horizontal. 108
Figure 76. Rotor Orbits 1.0 Gram Imbalance Shaft Mounted Vertical. Speeds from 2400 to 2800 rpm. 109
Figure 77. Rotor Orbits 1.0 Gram Imbalance Shaft Mounted Vertical. Speeds from 2900 to 3100 rpm. 110
Figure 78. Rotor Orbits 1.0 Gram Imbalance Shaft Mounted Vertical. Speeds from 5400 to 6000 rpm. 111
Figure 79. Maximum Displacements and Bode Plot for 1.0 Gram Imbalance Shaft Mounted Vertical. 112
Figure 80. Cascade Plot 1.0 Gram Imbalance Shaft Mounted Vertical. 113

LIST OF SYMBOLS

SYMBOL	DEFINITION (units, U.S. Customary)
E	Modulus of elasticity of the rotor shaft. (psi)
I	First moment of inertia of the rotor shaft. (in^4)
L	Length of the rotor shaft. (in)
M	Mass of the imbalance. (lbm)
M_{disk}	Mass of the rotor disk. (lbm)
M_{shaft}	Mass of the rotor shaft. (lbm)
PSD	Power spectral density. (mils/HZ)
$\{q\}$	Linear displacement vector. (in)
$\{\dot{q}\}$	Linear velocity vector. (in/sec)
$\{\ddot{q}\}$	Linear Acceleration vector. (in/sec^2)
e	Distance from shaft centerline to center of mass imbalance (in)
K_{xx}	x direction stiffness of bearing plus shaft caused by x direction displacement. (lbf/in)
K_{yy}	y direction stiffness of bearing plus shaft caused by y direction displacement. (lbf/in)
K_{xy}	x direction stiffness of bearing plus shaft caused by y direction displacement. (lbf/in)
K_{yx}	y direction stiffness of bearing plus shaft caused by x direction displacement. (lbf/in)
C_{xx}	x direction damping of bearing plus shaft caused by x direction velocity. (dimensionless)

C_{yy}	y direction damping of bearing plus shaft caused by y direction velocity. (dimensionless)
C_{xy}	x direction damping of bearing plus shaft caused by y direction velocity. (dimensionless)
C_{yx}	y direction damping of bearing plus shaft caused by x direction velocity. (dimensionless)
$\bar{F}$	Force caused by mass imbalance. (lbf)
F_x	Component of imbalance force in x direction. (lbf)
F_y	Component of imbalance force in y direction. (lbf)
Ω	Rotational speed of shaft and disk assembly. (rad/sec)
t	Time (secs)
$\phi(z)$	Axial displacement shape function (dimensionless)
x,y,z	Cartesian coordinates.

I. INTRODUCTION

Rotating machinery is widely used throughout the world in various applications. Such devices include gas turbines, steam turbines, pumps, compressors and fans. Rotating devices are subjected to numerous external and internal forces. These forces can be categorized as either steady or time varying. The time varying, or vibratory motions create alternating stresses, which tend to decrease the operational life of the equipment, due to wear and high cycle fatigue. Proper prediction of the machine dynamics, during the design phase, along with an appropriate condition monitoring program, during the life cycle, is imperative if sufficient component life is to be ensured. Smooth operation of rotating machines is critical to all users of these machines including the U.S. Navy.

Rotating machines can undergo many types of vibrations which are induced from a variety of sources. Axial compressor and turbine airfoils, excited primarily by upstream wakes, may undergo bending and torsional vibration loads. The shaft and disks can vibrate in axial, torsional and lateral modes. All of these vibrations may occur due to either external forcing or various self-excitation mechanisms.

Lateral vibrations, due primarily to residual imbalance in rotating members, is the most common type of vibration encountered in practice. Rotors tend to be designed to operate at speeds in excess of their first lateral critical speed. This is termed supercritical operation. This type of operation provides low vibration levels at the operating speed and light weight devices leading to less expensive machinery. One major problem with operating a rotor supercritically is that the rotor must proceed through the resonance speed, where high vibratory stresses occur, prior to reaching its operating speed. Transition through the critical speed should be done as quickly as possible in order to prevent such resonant conditions or to reduce the time at which the equipment experiences the high vibration levels. To reduce the lateral bending forced response, which is due to residual imbalance, many balancing techniques are employed. However, even when the device is in balance to a specific grade the radial response near the resonant speed can be quite high. The vibration problems encountered in rotating machinery can lead to significant equipment damage due to the close tolerances encountered in the rotating device. The alternating stresses generated by these vibrations can also create bearing distress, which can lead to premature failure.

The major design considerations relating to lateral shaft vibrations are to determine the critical frequencies and the radial response magnitudes as a function of rotor speed (and possibly rotor angular acceleration) as well as any potential regimes of rotordynamic instability.

Rotating equipment design can be improved by having a better understanding of the various rotordynamic phenomena which relate to machinery vibration problems. Understanding the dynamics of the various components in a rotating machine can lead to much improved designs and hence longer operating lives and lower life-cycle costs.

An ideal, symmetric rotor with symmetric bearings and supports will typically have circular orbits of the shaft center which get progressively larger until the critical speed is reached. After the rotor transitions through the critical speed the orbits remain circular and decrease in size. The orbits remain in the same direction as the rotation of the shaft (forward whirl), as shown in Figure 1. Maximum displacements from the shaft centerline are observed at or near the critical speed (resonance).

However, in a recent experimental investigation by Simei [Ref. 1], a much more complex lateral response was observed from a simply supported single disk rotor. The orbits started in a small amplitude, circular forward procession at low speeds. As the rotor speed was increased the orbits became elliptical. At an initial critical speed, the orbit "collapsed" into a line. At a slightly higher speed the rotor executed a whirl orbit in the reverse direction of shaft spin. This phenomena is termed "backward whirl" and is shown in Figure 2. There was a small range of rotor speeds where the backward whirl phenomena occurred. At a slightly higher speed a second resonant peak occurred along with another collapsed orbit. As the speed was further increased the orbits again proceeded in the forward direction and became more circular (less elliptical).

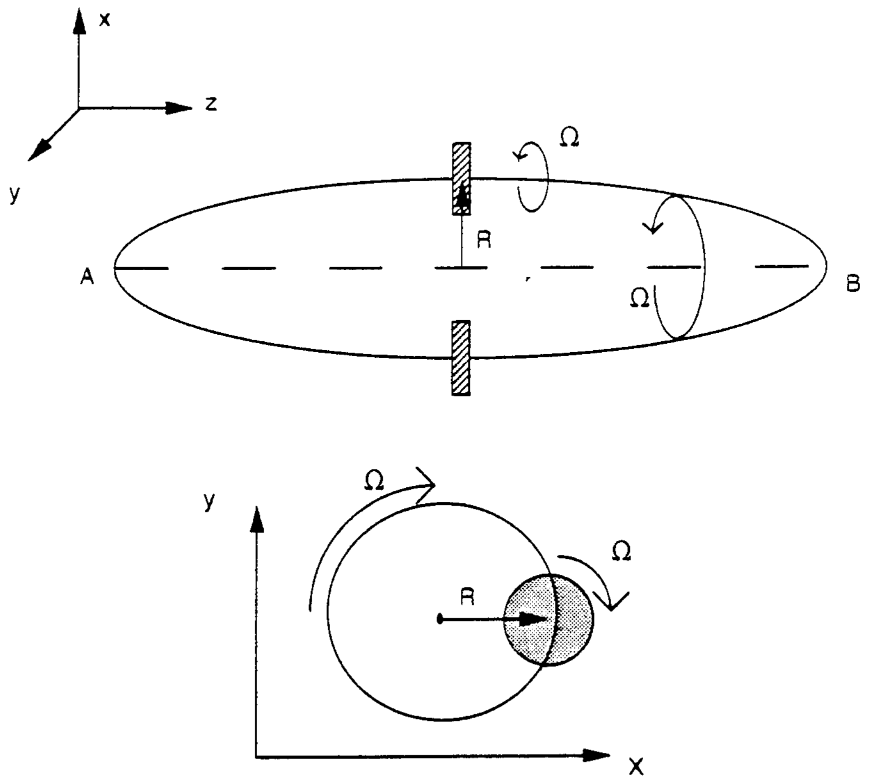

Figure 1. Rotor and Disk Assembly in Forward Whirl

The backward whirl phenomena is believed to be caused by distinctly different natural frequencies of the rotor system in the two orthogonal lateral directions. [Ref. 2] The two (split resonant) frequencies cause x and y displacement curves to have peak values at separate rotational speeds.

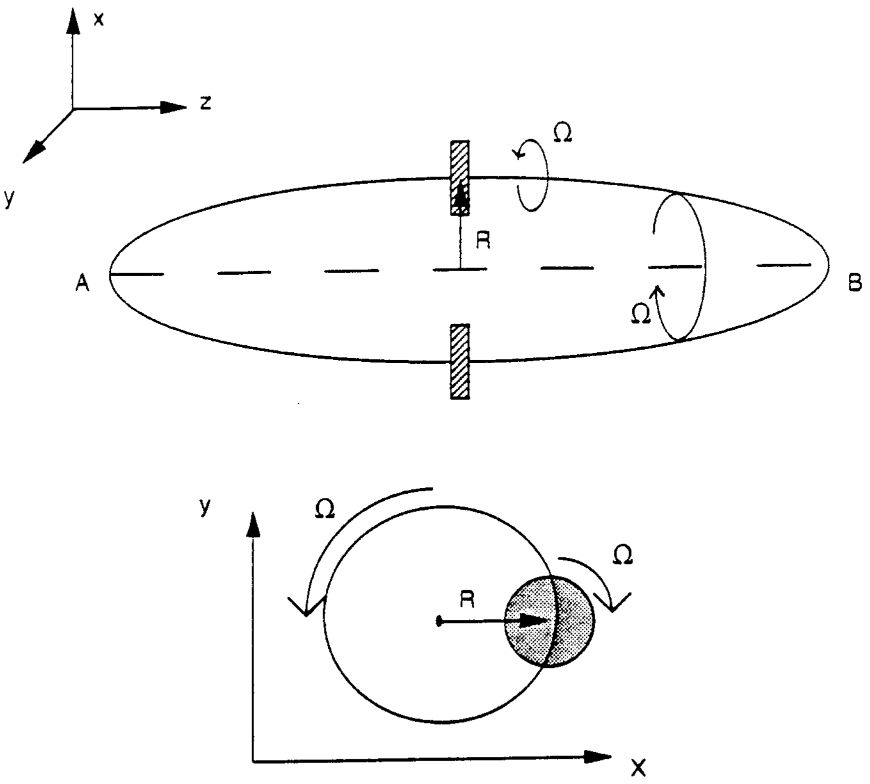

Figure 2. Rotor and Disk Assembly in Backward Whirl

The objectives of this research were to identify the cause of the split resonance and backward whirl phenomena. To determine if, in fact, these two phenomena are caused by different natural frequencies in the two directions created by non-symmetric bearing rotordynamic coefficients and, if this was determined to be the cause of backward whirl, to identify the specific cause of the asymmetry.

In Chapter II a review of the pertinent literature is given to provide sufficient background information concerning this research.

In an attempt to identify the causes for the complex behavior noticed in the simple rotor configuration an analytic model is developed in Chapter III and the major parameters varied to influence rotor responses. The analytic solutions are compared to experimental results obtained in a closely controlled environment.

In Chapter IV experiments, which were conducted, are described and show the effects of gravity, bearing eccentricity and imbalance. In generating experimental data a variety of rotor bearing configurations was employed, however the shaft remained in the simply supported configuration

To determine the effect of imbalance, the rotor was purposely placed out of balance using known weights. The amount of imbalance was gradually increased. To determine the effect of bearings on rotor response, elongated bearings (eccentric) were used and oriented in various relative positions on the bearing mounts. The shaft was then positioned in orthogonal directions with respect to the gravitational field to determine the effects of gravity and bearing support structure on rotor response.

A modal test to determine static natural frequencies of the experimental apparatus in the two lateral directions was conducted by installing accelerometers on the rotor assembly and applying a known impulsive force with the use of a precision hammer. The vertical natural frequency was found to be slightly higher than the horizontal natural frequency implying asymmetric stiffness properties in these two directions.

A discussion of results from both the experimental and analytic models is contained in Chapter V and recommendations and conclusions are provided in Chapter VI.

II. BACKGROUND

The first documented rotordynamic analysis was submitted by Rankine [Ref. 3] in 1869. He considered a simply supported rotating shaft and proposed that the deflection of the shaft is caused by the centrifugal force due to some nominal shaft deflection. Opposing this force is the shaft bending rigidity (stiffness). In the analysis he came to the erroneous conclusion that supercritical operation was statically unstable in the rotating reference frame and hence not possible for rotating machines. In Rankine's analysis, the Coriolis forces in the rotating reference frame were not considered. If purely radial motion of the shaft is considered this would be the case, however, the orbiting motion creates additional forces which stabilize the shaft.

In 1919 Jeffcott [Ref. 4] published an article analyzing the effects of imbalance on rotating machines. This analysis, which is considered the classical reference on the subject, provides the simplest and most accurate model of the dynamics of a simply supported rotating shaft. Jeffcott corrected the basic mistake made by Rankine. The Jeffcott rotor is comprised of a long shaft with a concentrated mass disk. This is a two degree-of-freedom model for transverse motion. Jeffcott described the phenomena of "whirling" and was the first to notice, and correctly assess, the effect of natural frequencies on rotordynamic response. Damping was neglected in his analysis and a pronounced change in phase was observed as the rotor transitions from subcritical speeds through resonance to supercritical speeds. In addition, Jeffcott showed the advantages of supercritical operation of rotating machinery.

Subsequent to Jeffcott's work, many authors have developed analytical models for rotors and compared the predicted results to those obtained experimentally. The influence of bearing dynamics, gyroscopic effects (from the disk), support flexibility and many other phenomena have been investigated. In 1986 Muszynska [Ref. 5] published an article detailing the fundamental response of rotating machines. Muszynska expressed an analytic model of rotor imbalance which included damping forces to predict rotor dynamic response for a wide range of unbalanced rotors.

In 1988 Vance [Ref. 2] proposed that the backward whirl phenomena is caused by the rotor imbalance when the rotational speed is between to natural frequency splits caused by bearing stiffness asymmetry. He also surmised that increased damping would cause the backward whirl phenomena to "disappear." He had, in fact, observed the backward whirl phenomena in his experimental results.

Simei [Ref. 1], in a Masters Thesis at the Naval Postgraduate School, obtained a rotor analysis kit from the Bentley Nevada Corporation and installed software for data acquisition and signal processing. Under certain shaft loading conditions backward whirl was observed and documented, however an explanation as to the cause of this phenomena was not provided. Simei used brass oil impregnated (oilite) bearings for all of his experiments and configured the rotor assembly as simply supported with a single disk arrangement. The backward whirl phenomena was observed to occur between to distinct maximum displacement peaks in the two orthogonal lateral directions.

III. ANALYTIC MODEL

In order to determine the cause of the split resonance and backward whirl and to predict rotordynamic response, a simple analytic model was developed. The model had to be capable of incorporating non-symmetric bearing characteristics, both stiffness and damping, which was hypothesized to be the cause of the observed split resonance and backward whirl. In this model the rotor shaft was modeled as a two degree-of-freedom (x and y) lumped mass and stiffness shaft and disk assembly as shown in Figure 3.

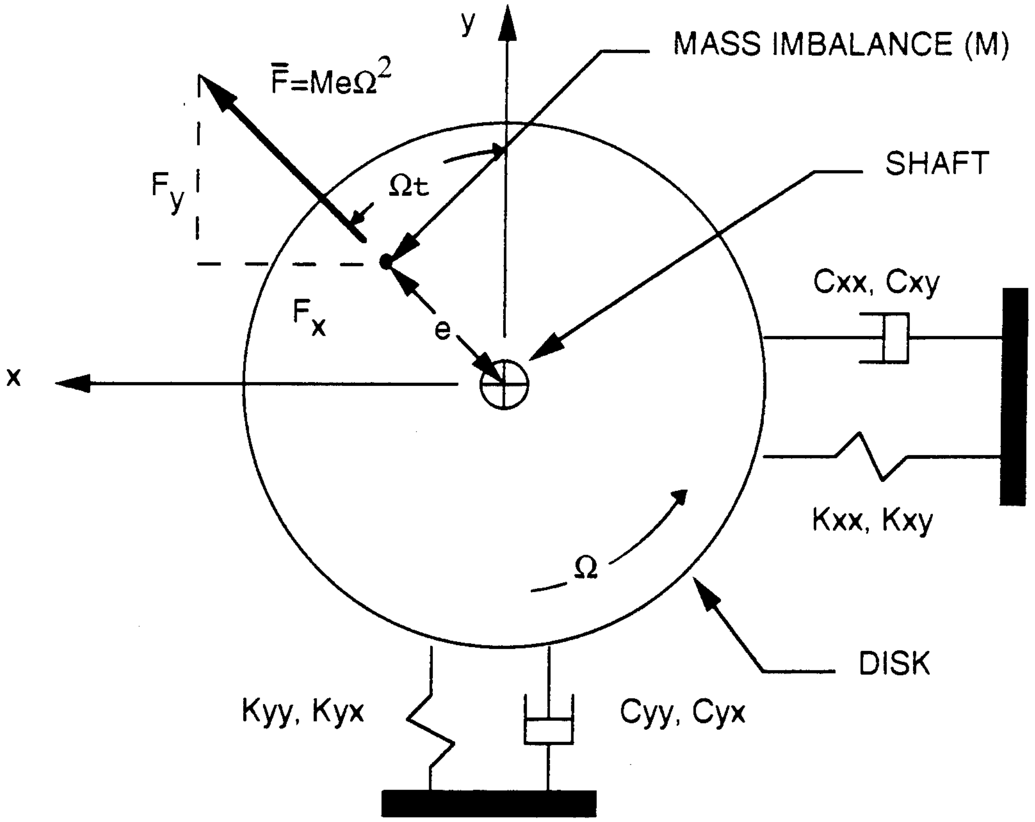
y
MASS IMBALANCE (M)
$\bar{F}=Me\Omega^2$
SHAFT
F_y
Ωt
Cxx, Cxy
F_x
e
x
Kxx, Kxy
Ω
DISK
Kyy, Kyx
Cyy, Cyx

Figure 3. Analytic Lumped Mass and Stiffness Model of Two Degree-of-Freedom Rotating Shaft and Disk Assembly.

The model includes bearing and shaft forces which are linearly related to the displacements and velocities of the rotor only. The variations in the axial direction have been ignored. All of the properties have effectively been concentrated into the single axial plane. The mass is the algebraic sum of the disk and the shaft masses. The direct stiffnesses, K_{xx} and K_{yy}, are a combination of the rotor shaft and the bearings stiffness. The cross stiffness terms, K_{xy} and K_{yx}, are due to any self excitation interfacial forces provided by the bearings. These are non-conservative forces. The direct damping terms, C_{xx} and C_{yy}, are from both material damping of the shaft as well as bearing and support proportional damping.

This model treats those cases when the two bearings are identical, but not necessarily symmetric. This means that the x and y displacements along the shaft follow the functional form of:

$$x(t,z) = x(t : z = z_o)\phi(z) \tag{1}$$

and

$$y(t,z) = y(t : z = z_o)\phi(z) \tag{2}$$

Where, x(t,z) and y(t,z) are the x and y displacements along the shaft, z is the axial direction, z_o is a particular location along the length of the shaft and $\phi(z)$ is the whirling mode shape.

The equation of motion for this model system, in terms of q, which represents the radial displacement of the shaft centerline, can be written in matrix form as:

$$[M]\left\{\ddot{q}\right\} + [C]\left\{\dot{q}\right\} + [K]\{q\} = \{F(t)\} \tag{3}$$

with,

$$q = \begin{Bmatrix} x \\ y \end{Bmatrix}$$

$$\dot{q} = \frac{dq}{dt} \qquad (4)$$

$$\ddot{q} = \frac{d^2q}{dt^2}$$

and the mass, damping and stiffness matrices respectively, are given by:

$$[M] = \begin{bmatrix} M_{tot} & 0 \\ 0 & M_{tot} \end{bmatrix}$$

$$[C] = \begin{bmatrix} C_{xx} & C_{xy} \\ C_{yx} & C_{yy} \end{bmatrix} \qquad (5)$$

$$[K] = \begin{bmatrix} K_{xx} & K_{xy} \\ K_{yx} & K_{yy} \end{bmatrix}$$

where,

$M_{tot} = M_{shaft} + M_{disk}$;

$K_{xx} = K_{xx(shaft)} + K_{xx(bearing)}$; $K_{yy} = K_{yy(shaft)} + K_{yy(bearing)}$;

K_{xy} and K_{yx} = coupling or cross stiffness ;

$C_{xx} = C_{xx(shaft)} + C_{xx(bearing)}$; $C_{yy} = C_{yy(shaft)} + C_{yy(bearing)}$;

C_{xy} and C_{yx} = coupling or cross damping

and, since the force on the shaft, F(t), is created by a mass imbalance and is periodic in time it can be expressed in exponential notation as:

$$\{F(t)\} = \overline{F}e^{j\Omega t} \qquad (6)$$

where $j = \sqrt{-1}$, Ω is the rotational speed of the shaft in rad/sec and t is time. From Figure 3 the force magnitude is:

$$\bar{F} = F = Me\Omega^2 \tag{7}$$

where, M is the mass of the imbalance, e is the radial distance from the shaft centerline to the location of the mass imbalance and Ω is the rotational speed of the shaft.

x and y displacements are known to be sinusoidal and the absolute displacements in the x and y directions are orthogonal, therefore, assume q is of the form:

$$\{q\} = \bar{q}e^{j\Omega t} \tag{8}$$

where $\bar{q}$ is a radial displacement : $\sqrt{(x^2 + y^2)}$. Taking derivatives with respect to time:

$$\begin{aligned} \left\{\dot{q}\right\} &= \bar{q}(j\Omega)e^{j\Omega t} \\ \left\{\ddot{q}\right\} &= \bar{q}(-\Omega^2)e^{j\Omega t} \end{aligned} \tag{9}$$

Substituting Equations (7) (8) and (9) into Equation (3) gives

$$[M]\bar{q}(-\Omega^2)e^{j\Omega t} + [C]\bar{q}(j\Omega)e^{j\Omega t} + [K]\bar{q}e^{j\Omega t} = \bar{F}e^{j\Omega t} \tag{10}$$

but $e^{j\Omega t} \neq 0$ for finite time and solving Equation (10) for $\bar{q}$ leads to,

$$\bar{q} = \left[[K] - \Omega^2[M] + j\Omega[C]\right]^{-1}\bar{F} \tag{11}$$

Now the displacements x and y can be determined by selectively substituting Equations (4) and (5) into Equation (11) which provides for a direct solution for the displacements:

$$\begin{Bmatrix} x \\ y \end{Bmatrix} = \left[\begin{bmatrix} K_{xx} & K_{xy} \\ K_{yx} & K_{yy} \end{bmatrix} - \Omega^2 \begin{bmatrix} M_{tot} & 0 \\ 0 & M_{tot} \end{bmatrix} + j\Omega \begin{bmatrix} C_{xx} & C_{xy} \\ C_{yx} & C_{yy} \end{bmatrix} \right]^{-1} \{\overline{F}e^{j\Omega t}\} \tag{12}$$

Equation (12) is limited to steady state (constant speed) response, symmetric shaft configurations, and linear stiffness and damping. This equation does not apply to cases where the rotor is accelerating or configured with two different types of bearings.

To obtain an approximation for the stiffness terms, the shaft and disk assembly can be modeled as a pinned-pinned beam as shown in Figure 4. Where the force P is the weight of the disk.

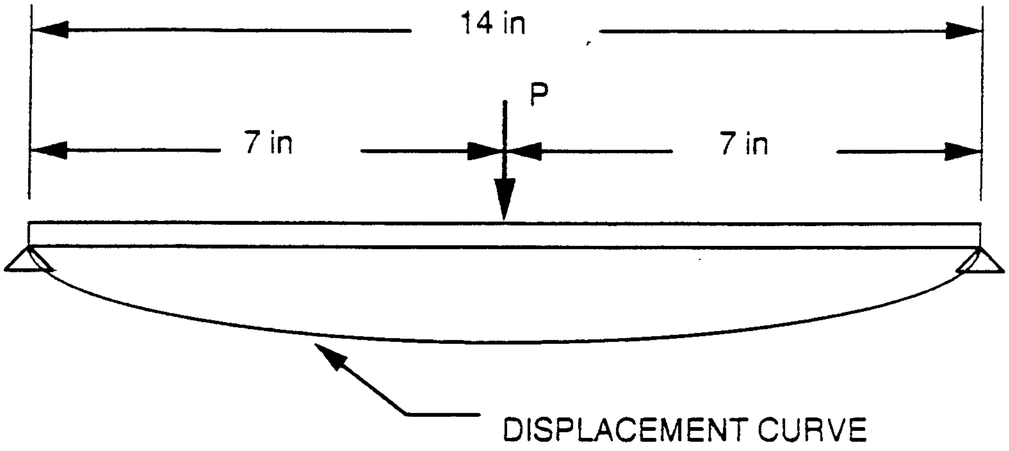

Figure 4. Analytic Pinned-Pinned Model of Shaft and Disk Assembly.

From [Ref. 6] the stiffness of the shaft is:

$$K_{shaft} = \frac{48EI}{L^3} \tag{13}$$

Using the shaft data in Appendix A, the shaft and disk mass can be determined and the shaft stiffness is found to be 495 lbf/in. The bearing stiffness and all of the damping terms must be selectively chosen since no hard data is available and modeling it is non-trivial.

The displacements obtained using Equation (12) are for the disk position and a straight line extrapolation can be performed to obtain the displacements anywhere along the length of the shaft.

To quantify the effects of the various parameters in Equation (12) values were chosen for stiffness and damping with a 1.0 gram mass imbalance imposed and the equation was solved. The model was used to see the effects on rotor response caused by separately imposed analytic conditions. The first solution only considers the stiffness of the shaft and uses symmetric damping and stiffness. A comparison was made to the results obtained in [Ref. 1]. The procedure was repeated many times with varying coefficients in an attempt to isolate the effects of asymmetric stiffness, asymmetric damping, cross stiffness and cross damping. The results of some of these analyses are contained as plots in Appendix B and an explanation of each solution is provided in the following subsections (stiffnesses are in lbf/in and damping coefficients are dimensionless).

It may be possible to optimize Equation (12) to match observed data, however, this was not done. The sequential progression through each of the imposed analytic responses lead to an increased understanding of rotordynamic response phenomena.

The rotational speed of the shaft is termed (1x), twice rotational speed is (2x) and one half rotational speed is (1/2x). This terminology follows that contained in the reference material discussed in Chapter II.

A. $K_{XX} = 495$, $K_{YY} = 495$, $C_{XX} = .025$, $C_{YY} = .025$

The rotor orbits and displacements are shown in Figure 6. The orbits are circular, as expected, with a resonant speed of approximately 2720 rpm. The displacements in the x and y directions are symmetric with a maximum value of 32 mils. The phase diagram and cascade plot are shown in Figure 7. A smooth transition from subcritical to supercritical speed is observed on the phase diagram at the resonant speed. The cascade plot indicates the energy content of the system is contained at the operating speed of the shaft with no indication of (1/2x) or (2x) vibrations. This is to be expected since sub-harmonic and super-harmonic responses are due to nonlinearities which this model does not contain. The observed resonant speed is lower than that obtained in [Ref. 1] which leads to the conclusion that a bearing stiffness term exists.

B. $K_{XX} = 535$, $K_{YY} = 555$, $C_{XX} = .025$, $C_{YY} = .025$

The bearing stiffness is assumed to be 40 lbf/in where the disk is located along the shaft and 20 lbf/in asymmetric stiffness is imposed. The rotor orbits and displacements are shown in Figure 8. The orbits begin in a circular pattern at slow speeds and proceed into elliptical patterns and exhibit the backward whirl condition at 2840 rpm. This closely matches the resonant speed found in [Ref. 1]. Two distinct resonant speeds are evidenced from the displacement plots which is indicative of the asymmetric stiffness in the x and y directions, however the magnitudes of the displacements are similar. The phase diagram and cascade plot are shown in Figure 9. The phase shift for the x direction remains smooth and the cascade plot is similar to symmetric stiffness.

C. $K_{XX} = 535$, $K_{YY} = 535$, $C_{XX} = .035$, $C_{YY} = .02$

The rotor orbits and displacements are shown in Figure 10 for symmetric stiffness and asymmetric damping. The orbits are circular at slow speeds and become elliptical as the resonant speed is reached, however, backward whirl is not observed. The resonant speed is the same in both the x and y directions but the y displacement magnitude is greater due to the lower damping coefficient. The phase diagram and cascade plot are shown in Figure

11. The phase transition is smooth while the cascade plot shows the increased amplitude of vibration in the y direction.

D. $K_{XX} = 535$, $K_{YY} = 555$, $C_{XX} = .04$, $C_{YY} = .02$

For asymmetric stiffness and asymmetric damping the rotor orbits and displacement plots are shown in Figure 12. The orbits are circular at slow speeds and become elliptical near resonance. Backward whirl is evidenced at 2860 rpm which is approximately the midpoint of the maximum x and maximum y displacements. The phase diagram and cascade plot, Figure 13, show a smooth transition through resonance and a lower spectral amplitude due to the interaction of stiffness and damping.

E. $K_{XX} = 535$, $K_{YY} = 575$, $C_{XX} = .04$, $C_{YY} = .025$

To investigate the decreased cascade spectral amplitude the stiffness asymmetry is increased while the damping asymmetry is decreased. The rotor orbits and displacement plots are shown in Figure 14. The orbits begin circular and proceed into elliptical patterns as resonance is approached. The backward whirl condition remains through a wider range of speeds, between 2840 and 2920 rpm. The displacement peaks are further separated due to the increase in stiffness asymmetry. The cascade plot, Figure 15, shows no marked change in spectral magnitude and the phase diagram remains smooth throughout resonant transition.

F. $K_{XX}=535$, $K_{YY}=535$, $K_{XY}=40$, $K_{YX}=10$, $C_{XX} = .025$, $C_{YY} = .025$

The rotor orbit and displacement plots for symmetric stiffness and symmetric damping with cross stiffness terms are shown in Figure 16. The orbits begin circular but quickly become elliptical as shaft rotational speed is increased. In the region of the y displacement dip, backward whirl is observed with the elliptical orbits perpendicular to those of Figure 14. The magnitude of the x displacement is almost twice that of the y displacement. The cascade plot for the y direction is shown in Figure 17 and the low amplitude of response is depicted. The phase diagram, Figure 17, indicates a 180 degree phase shift at the first resonant peak, another 180 degree phase shift at the base of the first resonant peak and a final 180 degree phase shift at the second resonant peak.

G. $K_{XX}=535$, $K_{YY}=535$, $K_{XY}=10$, $K_{YX}=40$, $C_{XX} = .025$, $C_{YY} = .025$

The rotor orbits and displacement plots illustrating the effect of reversing the cross stiffness amplitudes are shown in Figure 18. The orbits are similar, however the axis of orbit elongation is perpendicular to those of Figure 16. Backward whirl is evidenced through the same speed range. The y displacement is now nearly twice the magnitude of the x displacement. The phase diagram and cascade plots are shown in Figure 19. The phase begins to shift as the first resonant speed is approached but is delayed by the large decrease in x displacement amplitude at 2800 rpm. The phase shift then proceeds smoothly through the rest of the transition zone. The cascade plot shows the increased spectral magnitude in the y direction.

H. $K_{XX}=535$, $K_{YY}=535$, $C_{XX}=.025$, $C_{YY}=.025$, $C_{XY}=-.02$, $C_{YX}=-.01$

The rotor orbits and displacements for symmetric stiffness and symmetric damping with negative cross damping terms are illustrated in Figure 20. The rotor orbits are slightly elliptical near resonant speeds and circular elsewhere. The large magnitude of displacements in both the x and y directions stem from the negative cross damping terms. The magnitude of the x displacement is greater than the y displacement. The phase diagram and cascade plot, Figure 21, show a steep phase shift through resonance due to the negative cross damping and the cascade plot shows a large spectral amplitude at the resonant speed.

I. $K_{XX}=535$, $K_{YY}=535$, $C_{XX}=.025$, $C_{YY}=.025$, $C_{XY}=.02$, $C_{YX}=.01$

The rotor orbits and displacement plots for symmetric stiffness and damping with positive cross damping are shown in Figure 22. The rotor orbits become elliptical near resonance but remain in the forward whirl condition and the major axis of the elliptical orbits is perpendicular to those shown in Figure 20. The x displacement has a small area where the curve flattens (near 2800 rpm) and the y displacement magnitude is greater than the x displacement. The phase diagram and cascade plots are shown in Figure 23. The phase diagram shows a small region (at approximately 2800 rpm) where the phase curve flattens. This is the same region with the flattened displacement curve. The cascade plot indicates the spectral energy content.

J. $K_{XX}=535$, $K_{YY}=555$, $K_{XY}=-5$, $K_{YX}=3$, $C_{XX} = .025$, $C_{YY} = .025$

The rotor orbits and displacement plots for asymmetric stiffness, symmetric damping and imposed opposite cross stiffnesses are shown in Figure 24. The orbits begin circular and become elliptical as the rotor approaches resonant speed. The shaft does not achieve the backward whirl condition. The displacement plot shows a small double peak near the resonant speed. The phase diagram and cascade plot, Figure 25, shows a small overshoot in the phase transition. Spectral peaks are located near the resonant speed and at the forced response speed (operating speed) of the rotor.

In conclusion, the analytic model, previously developed, does predict the split resonance and backward whirl phenomena noticed in [Ref. 1]. Distinctly different types of responses are generated depending on the type of stiffness and damping terms employed in the solution. The asymmetric stiffness model matches most closely to the experimental results obtained by Simei. [Ref. 1]

IV. EXPERIMENTAL INVESTIGATION

The analytic results provided in Chapter III showed that asymmetric stiffness (difference in K_{xx} and K_{yy} terms) created the split resonance and backward whirl phenomena similar to that experienced by Simei. [Ref. 1]

To determine the physical cause of the stiffness asymmetry the rotor assembly hardware, used in [Ref. 1], was investigated.

Finally as a direct measurement, accelerometers were positioned on the rotor assembly and a precision hammer (load cell) was used to provide a known impulsive force to the rotor. The horizontal (x direction) static natural frequency was found to be 46.00 cycles per second (cps), while that of the vertical (y direction) was 46.75 cps. The disparity in the two frequencies leads to the possibility of asymmetric supports or bearings as a cause of the split resonance.

The lubrication regime within the bearing during the split resonance and backward whirl phenomena is unknown. Since the bearing is manufactured with oil impregnated brass, the lubrication may be hydrodynamic (either full or partial oil film), metal to metal rub or the shaft may actually lift off of the surface and be in aerodynamic lubrication.

Possible causes were divided into four broad categories: non-circularity of the bearings, gravity effects, degree of imbalance and bearing support asymmetry.

1. Non-Circularity of Bearings

The shaft diameter is 0.375 inches with a design radial bearing clearance of 1 mil. The bearings were removed from the experimental hardware used in [Ref. 1] and one of the bearings was found to be 2 mils out-of-round (non-circular). The physical condition of the bearing and its orientation with respect to the two orthogonal lateral directions may lead to unequal stiffness terms in the x and y directions. This would, in effect, create different K_{xx} and K_{yy} terms as used in the analytic model.

2. Gravity Effects

The position of the shaft journal in the bearing may constrain the motion of the shaft within the bearing, thus increasing the magnitude of force necessary to cause the rotor to move in that direction. This type of situation can be directly related to stiffness variations in the two lateral directions.

3. Degree of Imbalance

The magnitude of the mass imbalance may generate a forcing function F(t) which is large enough to overcome the constraints of gravity and rotor centrifugal force and produce backward whirl.

4. Support Asymmetry

The bearing support structure is itself asymmetric. The vertical (y) direction is bolted to the assembly base plate, which may make the stiffness greater in the vertical direction. The horizontal (x) direction of the support is not hard mounted and may have more flexibility (less stiffness) as a result.

Of the four possible physical causes presented only gravity effects, non-circularity of the bearings or bearing support asymmetry can create asymmetric direct stiffness.

In order to determine the actual physical cause of the asymmetric stiffness, the experimental facility developed in [Ref. 1] was used to provide data for a variety of rotor imbalances and bearing and shaft orientations. The ROTOR.VI program developed in [Ref. 1] was used to collect the time trace data which was processed and plotted using a MATLAB computer program.

The rotor assembly is shown in Figure 5 and a variety of mounting configurations and bearing arrangements was used to determine the effect of various parameters on rotordynamic responses. The data obtained from the various rotor configurations is tabulated at the end of this Chapter. The plotted results from the experimental investigations are contained in Appendix C.

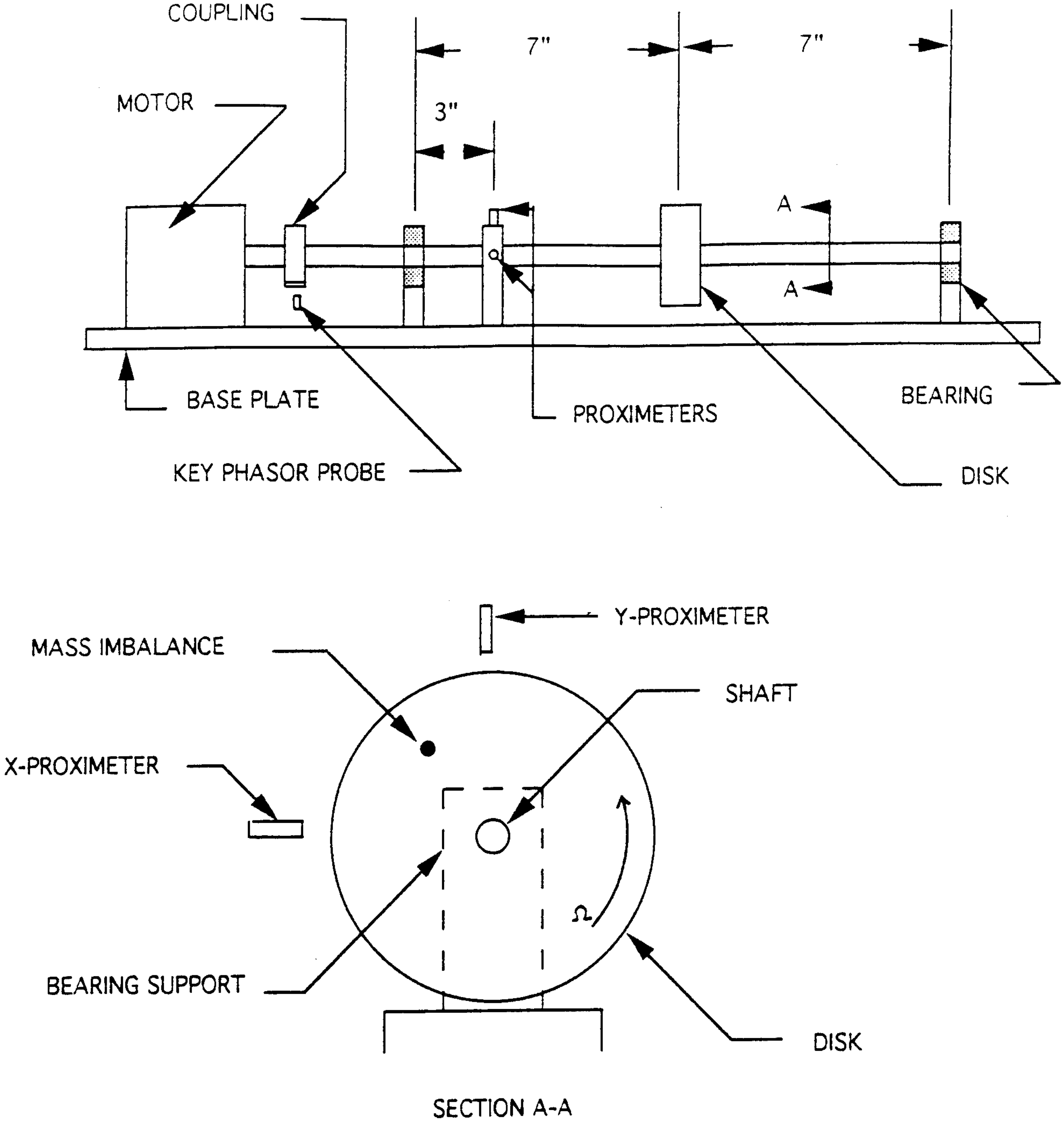
COUPLING
MOTOR
7"
7"
3"
A
A
BASE PLATE
PROXIMETERS
BEARING
KEY PHASOR PROBE
DISK
Y-PROXIMETER
MASS IMBALANCE
SHAFT
X-PROXIMETER
Ω
BEARING SUPPORT
DISK
SECTION A-A

Figure 5. Configuration of Experimental Rotor System.

A. GOOD BEARING TABLE MOUNT

The rotor assembly was mounted on a table with a soft foam pad under the base plate. Both the inboard and outboard bearings, with respect to the drive motor, were replaced with circular bearings (good bearings) of 1 mil clearance between the shaft journal and the bearing. The foam pad acts as a low pass filter, thus eliminating any high frequency unwanted inputs to the system. The x direction is horizontal and the y direction is vertical, or in the direction of gravitational force as shown in Figure 5.

1. Good Bearing No Imbalance

The rotor orbits for a good bearing (circular with 1 mil radial clearance; tolerance of 0.5 mil) with no shaft imbalance are shown in Figures 26, 27 and 28. The originally circular orbits become elliptical and collapse into a line at a resonant speed of 2840 rpm. Backward whirl is not observed. The orbits at twice critical speed (5600-6200 rpm) remain circular. The radial displacement and phase diagrams are shown in Figure 29. The phase shift is abrupt through the resonant speed while the displacement plot has a wide frequency range in which resonance occurs. The cascade plot shown in Figure 30 indicates the frequency corresponding to the maximum amplitude. A slight amount of spectral energy is evidenced in the (2x) and (3x) regions of the plot.

2. Good Bearing 0.5 Gram Imbalance

The rotor orbits for a good bearing with a 0.5 gram imbalance are shown in Figures 31, 32 and 33. The resonant speed is much less abrupt, but a large amplitude response exists between 2800 and 2900 rpm. The orbits begin circular then become elliptical and collapse into a line at 2800 rpm. The orbits then become elliptical again, in the forward whirl direction, and again collapse at 2900 rpm. From this speed onward the orbits revert back into a circular pattern and remain circular at twice the critical speed. The radial displacement shows a slight double peak and the phase diagram indicates higher damping is evident by the gradual transition through resonance, Figure 34. The cascade plot, Figure

35, indicates a higher spectral energy content at resonance and (2x) and (3x) vibration levels are observed.

3. Good Bearing 1.0 Gram Imbalance

The rotor orbits for a good bearing with 1.0 gram imbalance are shown in Figures 36, 37, 38 and 39. The orbits are circular at slow speeds and become elliptical as the resonant speed is approached. The orbits collapse into a line at 2800 rpm and then proceed into elliptical orbits in the backward whirl condition. The orbits remain in backward whirl until 2890 rpm when the orbits collapse into a line again. The orbits leave this condition in forward whirl and remain forward throughout the rest of the experimental speeds. At twice the resonant speed two distinct orbits are evidenced. The radial displacement and phase diagrams, Figure 40, show an increase in split resonance range and a higher displacement in the y direction than the x direction. The phase plot continues to show slightly increased damping, however, the transition through critical speed remains abrupt. Figure 41 depicts the cascade or spectral information and indicates increased spectral content at the (1/2x) speed when the rotor is at twice the critical speed corresponding to the two distinct orbits at these speeds.

4. Good Bearing 1.6 Gram Imbalance

The rotor orbits for critical and super-critical speeds for 1.6 gram imbalance are shown in Figures 42, 43, 44, 45 and 46. The orbits collapse at 2760 rpm and proceed into a much more pronounce backward whirl condition through 2880 rpm. The orbits collapse again at 2890 rpm and proceed into another backward whirl orbit with the major axis shifted to a more vertical direction. The orbits abruptly change to forward whirl at approximately 3125 rpm and remain forward and circular through 7000 rpm. The orbits at twice critical speed again exhibit the dual orbit phenomena. Two very distinct peaks are noticed in Figure 47. The magnitudes of the x and y displacements are almost identical, however, the speed at which they occur is more widely separated. The phase transition, in Figure 47, shows a decrease in the phase slope as the rotor approaches resonance. The peak displacement remains for a longer speed duration which causes the phase to remain at 90 degrees for a short while. Figure 48 shows the cascade plot and indicates spectral energy content at (1/2x) when the rotor is at twice resonant speed but also indicates high energy content at (2x), (3x) and (4x) frequencies when the rotor is at critical speed.

B. BAD BEARING TABLE MOUNT

To test the effect of a non-circular bearing on rotor response and particularly split resonance and backward whirl, a spare bearing was machined into an elliptical shape. The major axis was measured to be 0.3810 inches while the minor axis was 0.3760 inches. This represents a very non-circular bearing.

Only one bad bearing was used in the experimental apparatus and positioned in the inboard bearing support (closest to the proximeters). The use of two bad bearings would have resulted in much higher vibrational displacements than can be measured with the proximeters in the positions illustrated in Figure 5. The outboard bearing was kept as a circular bearing.

1. Vertical Bad Bearing 1.0 Gram Imbalance

The bearing was positioned with the major axis of elongation in the vertical (y direction). The rotor orbits for this configuration are shown in Figures 49, 50, 51 and 52. The orbits begin circular at slow rotor speeds and proceed into elliptical patterns as resonant speed is approached. The rotor reaches resonance at 2840 rpm as the orbits collapse into a line. A slight backward whirl is observed until the rotor reaches 2940 rpm at which point the orbits collapse again then proceed in a forward whirl motion and elliptical patterns. The orbits become circular again at 3200 rpm. At twice the resonant speed very large deflection amplitudes are present along with peculiar rotor orbits. The orbits become normal at 6000 rpm. The radial displacement and phase diagrams, Figure 53, show a very wide split peak near the resonant speed and a second double peak near twice the resonant speed. The rotor exhibits a phase shift at each of these speeds. The cascade plot, Figure 54, shows the increased (1/2x) energy content at twice resonance and high vibration levels at (2x) and (3x) frequencies through all rotor speeds.

2. Horizontal Bad Bearing 1.0 Gram Imbalance

The rotor orbits with the elongated bearing positioned with the major axis in the horizontal (or x direction) are shown in Figures 55, 56, and 57. The orbits near resonant speed are similar to those for the vertical position, however, the orbits at twice resonant speed are much less erratic. The radial displacement and phase diagrams, Figure 58, again show a split peak near resonance and another at twice resonant speed and the phase again shifts twice. The cascade plot is shown in Figure 59.

3. 45 Degrees Left Bad Bearing 1.0 Gram Imbalance

The elongated bearing was positioned with the major axis in the general direction of the resonant displacement (approximately 45 degrees off the vertical). The rotor orbits are shown in Figures 60, 61, 62 and 63. The near resonance orbits are again similar to those for the vertical bearing direction and the twice resonance speed orbits are similar as well except that they occur at slower rotational speeds. The radial displacement and phase diagrams, shown in Figure 64, indicate a split displacement peak near resonant speed and at twice resonant speed, however the phase shift is less pronounced at the higher speeds. The cascade plot, Figure 65, indicates less spectral energy content at the (2x) and (3x) frequencies.

4. 45 Degrees Right Bad Bearing 1.0 Gram Imbalance

The elongated bearing was positioned with the major axis perpendicular to the direction of resonant displacement (approximately 45 degrees off the vertical). The rotor orbits are shown in Figures 66, 67 and 68. The amount of backward whirl exhibited in this configuration is slightly reduced near the resonant speed. The orbits at twice resonant speed are much more similar to the good bearing configuration with a 1.0 gram imbalance. The radial displacement and phase diagrams, Figure 69, more closely resembles the good bearing plots depicted in Figure 40. The elongated bearing causes the phase shift to become erratic at speeds above resonant speed. The cascade plot in Figure 70 shows no indication of energy in (1/2x) frequency range when the rotor is at twice resonant speed, however (2x) and (3x) frequency levels are observed.

C. HORIZONTAL SHAFT MOUNT 1.0 GRAM IMBALANCE

The rotor assembly was wall mounted with the shaft in the horizontal (longitudinal) direction with rubber mounts installed between the base plate and the wall board. The x direction for this configuration remains horizontal and the y direction is in the vertical direction (direction of gravitational forces). Good bearings were installed at both the inboard and outboard positions.

The rotor orbits are shown in Figures 71, 72 and 73. The rotor orbits begin circular at slow rotational speeds then proceed into elliptical orbits. The orbits never collapse, however they rotate about the shaft centerline axis and at higher speeds the orbits are tilted off the vertical in a configuration which resembles a normal fluid lubricated bearing position. The displacement plots, Figure 74, show the decreased amplitude in the x direction due to the rubber isolation mounts and the effect of the wall board. The phase shift is very gradual, indicative of increased system damping. The cascade plot shown in Figure 75 shows the decrease in spectral energy at resonant speeds and a decrease in (2x) and (3x) vibration levels.

D. VERTICAL SHAFT MOUNT 1.0 GRAM IMBALANCE

With the rotor assembly wall mounted with the long axis of the shaft in the direction of gravitational force (vertically) the rotor orbits are depicted in Figures 76, 77 and 78. The orbits are circular at slow speeds and become elliptical near resonance. The collapse of the orbits near 2600 rpm indicate a decrease in the resonant speed and at higher speeds the orbits exhibit characteristics very similar to the analytic orbits obtained using slight asymmetric direct stiffness in Chapter III. Since the rotor is mounted with the y direction in the direction of the wall mounts the displacements are smaller in that direction, Figure 79. The phase diagram shows a more conventional transition through the resonant speed. The cascade plot, Figure 80, shows a very low energy content in the (1/2x), (2x) and (3x) regions indicative of low vibration levels.

The results of all of the previously listed experiments are provided in Table 1. The degree of backward whirl was significantly affected by the magnitude of the mass imbalance, but not significantly affected by the relative position of the elongated (non-circular) bearing. The responses obtained from the elongated bearing matched closely to the good bearing response at 1.0 gram imbalance except for the (1/2x) vibration levels and rotor orbits at twice the critical speed. The position of the rotor shaft, disk and mounting assembly relative to the gravitational force greatly affected the rotor response, however backward whirl was not evidenced in either of these configurations.

BEARING CONFIGURATION	IMBALANCE	1 X RESPONSE	1/2 X RESPONSE
BAD BEARING (TABLE MOUNT)	1.0 gram	BW/SR	YES
GOOD BEARING (TABLE MOUNT)	0.0 gram	NO BW/SR	NO
	0.5 gram	NO BW/SR	NO
	1.0 gram	BW/SR	YES
	1.6 gram	BW/SR	VERY MUCH
VERY BAD BEARING HORIZONTAL (TABLE MOUNT)	1.0 gram	BW/SR	VERY MUCH
VERY BAD BEARING VERTICAL (TABLE MOUNT)	1.0 gram	BW/SR	VERY MUCH
VERY BAD BEARING ⊥ RESONANT DISP. (TABLE MOUNT)	1.0 gram	BW/SR	YES
VERY BAD BEARING ǁ RESONANT DISP. (TABLE MOUNT)	1.0 gram	BW/SR	VERY MUCH
GOOD BEARING HORIZONTAL (WALL MOUNT)	1.0 gram	NO BW/SR	NO
GOOD BEARING VERTICAL (WALL MOUNT)	1.0 gram	NO BW/SR	NO

Table 1. Results From Experimental Investigation

V. DISCUSSION OF RESULTS

The previous analyses will be discussed as well as possible causes which produce the split resonance and backward whirl rotordynamic response phenomena. As expected, the experimental data is not as smooth as the analytic solutions generated by the model but a general insight into the overall characteristics of the rotor shaft and bearing system can be attained and useful information can be gleaned from the results. In all cases the response is greatly influenced by the forcing function F(t) which is created by imbalance.

By varying the characteristic parameters (K_{xx}, K_{xy}, K_{yx}, K_{yy}, C_{xx}, C_{xy}, C_{yx}, and C_{yy}) in the analytic model the rotor response can be significantly altered. In the first analysis, circular orbits were evident throughout the range of speeds of interest. The natural frequency of the system occurred at 2720 rpm which is lower than that obtained in the experimental analyses. The addition of a bearing stiffness term in the analytic model raised the resonant speed to 2840 rpm. The existence of asymmetric direct stiffnesses in the model caused elliptical orbits and the backward whirl phenomena. The addition of asymmetric stiffness terms caused a split peak in the x and y response amplitudes (split resonance). Asymmetric damping also caused elliptical orbits, however the rotor remained in forward whirl throughout the resonant speed range.

Bearing cross stiffness terms lead to split peaks and elliptical orbits and the direction of the highest cross stiffness affects the direction of the rotor resonant response. Small amounts of opposite cross stiffness cause a phase shift overshoot which is also evidenced in the 1.6 gram imbalance experimental results. Cross damping terms provide increased amplitude response if the terms are negative and cause elliptical orbits with forward whirl if the terms are small and positive.

The magnitude of the imbalance affects the response of the rotor in a variety of ways. Increased imbalance magnitude causes increased x and y deflections. Increased imbalance magnitude causes increased spectral energy in the (1/2x) region at high speeds and increased spectral content in the (2x) and (3x) range through all operating speeds. The cascade plots show that the dominant energy is contained at the operating speed of the shaft. Even with no imbalance imposed, the shaft will have relatively high vibration levels at the resonant speed of the rotor/bearing system. The 1.6 gram imbalance causes unexpected responses at the resonant speed and at multiples of the resonant speed, as evidenced by the increased energy level at the (2x), (3x) and (4x) frequencies. The unorthodox orbits exhibited under this loading are possibly caused by a non-linear response generated by this imbalance.

The elongated bearing provided increased response amplitudes in all cases except when the bearing was positioned to oppose the resonant displacement. The orbits at twice the resonant speed show marked differences in appearance and orientation. The supercritical orbits with the bearing positioned with the elongation in the direction of resonant displacement closely match those with the bearing positioned vertically. The long axes of the orbits are rotated 45 degrees and the speed at which they appear is slightly less but similarities do exist. The response of the rotor with the elongated bearing positioned perpendicular to the direction of resonant displacement is more similar to the good bearing response with 1.0 gram imbalance. The cascade plot for this configuration shows the decrease in energy content at the operating speed and the low energy levels at the (1/2x), (2x) and (3x) regions.

Mounting the shaft in the horizontal position, in effect, changed the gravitational effect on the shaft caused by the bearing support structure. The y displacements remained similar to the table mount experiment, however the x displacement amplitude decreased due to rubber isolation mounts being installed between the base plate and wall board. The phase transition was very gradual indicative of high damping in the system. The orbits follow a more conventional, fluid lubricated, bearing orbit as the rotor speed is increased.

With the shaft mounted vertically the effect of gravity on the bearing and bearing support structure was removed. The displacement in the y direction was damped out by the isolation mounts and wall board, however the orbits showed a pronounced resonance at 2720 rpm. This resonant speed corresponds to that achieved with only the shaft stiffness term in the analytic model.

VI. CONCLUSIONS AND RECOMMENDATIONS

A. CONCLUSIONS

Using the experimental facility developed in [Ref. 1] and an analytic model to predict rotordynamic phenomena, a deeper understanding of the physical mechanisms that create split resonance and backward whirl was obtained. Analytic variables can be altered to change the rotor output, in effect altering the transfer function which converts the forcing function input to the rotor response output.

The analytic model strongly suggests that the K_{xx} and K_{yy} (direct stiffness) difference is responsible for the split resonance and backward whirl phenomena

The modal test confirmed that K_{yy} is greater than K_{xx} on the experimental rotor assembly, at least statically.

The effect of mass imbalance on the experimental aparatus was shown as well as the effects of non-circular bearings.

The rotor system orientation with respect to the gravitational force coupled with the installation of rubber isolation mounts causes rotor responses to change.

Backward whirl can be induced by split resonance caused by a mass imbalance or gravitational force in the bearing. The effect of bearing support structure stiffnesses may also cause split resonance. If the bearing is more rigidly mounted in the direction of the bearing support bolts, the y stiffness may be greater than the x stiffness. This asymmetry may cause higher forces in the y direction leading to elliptical orbits and backward whirl.

Asymmetric damping within the bearing does not cause the backward whirl phenomena but does produce elliptical orbits.

Backward whirl is not caused by bearing non-circularity.

The vibrations of the rotor shaft differ depending on the orientation of the elongated bearing. The response amplitudes are higher if the elongation is in the direction of the resonant displacement of the rotor. The orientation of the non-circular bearing does not significantly alter the backward whirl orbits.

The bearing stiffness values are a function of the force applied, therefore the bearing stiffnesses change with rotor speed and with rotor orientation with respect to the gravitational field. Vertically mounted rotating assemblies will have a critical speed near the natural frequency of the shaft since bearing stiffness is negligible. At higher speeds, however the effect of bearing stiffness must be included in the analysis of the machine.

B. RECOMMENDATIONS

There are many areas yet to be investigated using the rotor kit and data acquisition software. The most prevalent include:

1. Developing an analytic/experimental procedure for rotordynamic parameter identification. This would entail solving for the coefficients in the analytic model using known experimental rotor responses.

2. Developing an optimization technique for determining the analytic model parameters (K_{ij} and C_{ij}). Given a rotor orbit a mathmatical equation for the response could be written.

3. Study in detail the physical mechanism through which gravity influences the stiffnesses in the lateral directions. This would most likely require a structurally sturdy but configureable mount to position the rotor assembly in any position in three dimensional space.

4. Conduct a detailed analysis of the lubrication regime within the bearing during backward whirl. The forces acting on the shaft journal at the bearing interface would need to be quantified along with lift and drag forces generated by the rotation of the shaft.

Additional areas of research include the investigation and determination of the dependence of bearing stiffness on shaft rotational speed, investigation of fluid lubricated bearing dynamics, roller bearing dynamics, and the effect of different isolation mounts on vibrational characteristics.

The analytic model developed herein should be modified to allow for the bearing stiffnesses to change as shaft speed increases. This will provide a more realistic rotor response.

The rotor kit is provided with two translucent fluid lubricated bearings. The wide use of fluid lubricated bearings in rotating machinery installations warrants research in this area. Use of the translucent bearings will provide both visual and time trace data to evaluate the rotor dynamic characteristics based on hydrodynamic and possibly hydrostatic bearings. The rotor can be configured with one or two fluid lubricated bearings.

The use of roller bearings on marine gas turbine installations motivates the research into roller bearing induced shaft vibrations. The amplitudes of response are expected to be higher than the brass oilite bearing since the stiffness of these bearings is higher. The rotor kit is provided with a roller bearing which is mounted between four adjustable springs. This will provide for increased control of the bearing influence on rotor response.

The rotor assembly should be hard mounted on a sturdy base which can be adjusted to configure the rotor in a variety of positions with respect to the gravitational field. Additional types of shock mounts should be obtained (with different stiffness values) and sequentially installed to determine their affect on rotor response.

APPENDIX A. LIST OF DIMENSIONS AND PROPERTIES

Rotor Shaft:

Material:	4140 Low Alloy Steel	
Modulus of Elasticity:	200 GPa	29.2(10^6) psi
Length:	45.7 cm	18.0 in
Diameter	0.9525 cm	0.375 in
Mass	0.253 kg	0.558 lbm
Density	7766 kg/m^3	0.281 lbm/in^3

Rotor Disk:

Material:	316 Stainless Steel	
Width:	2.54 cm	1.0 in
Inner Diameter	0.9525 cm	0.375 in
Outer Diameter	1.18 cm	3.0 in
Mass	0.816 kg	1.8 lbm

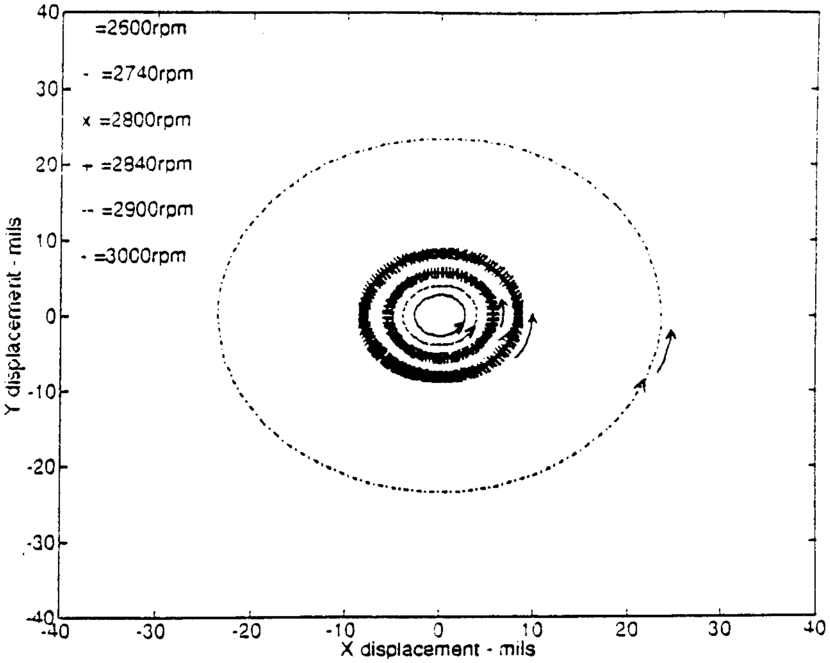

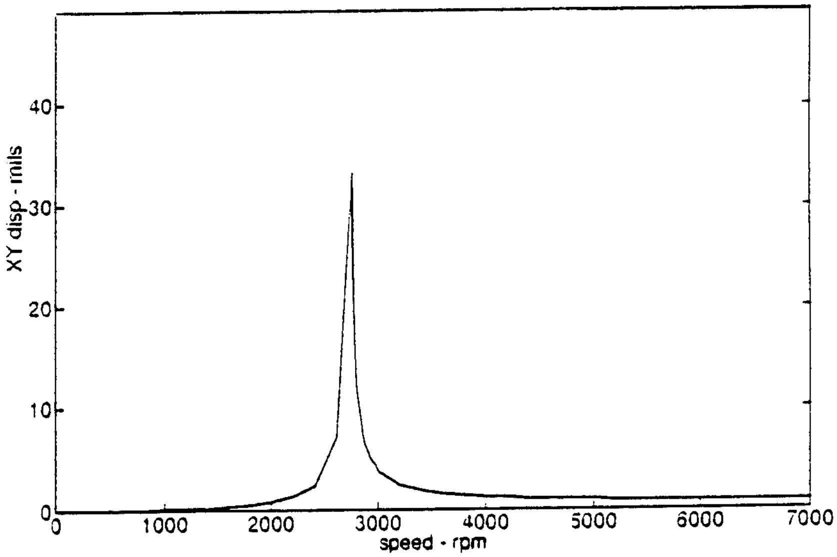

Figure 6. Rotor Orbits and Displacements From Analytic Model For Kxx = 495 lbf/in, Kyy = 495 lbf/in, Kxy = 0 lbf/in, Kyx = 0 lbf/in, Cxx = .025, Cyy = .025, Cxy = 0, Cyx = 0

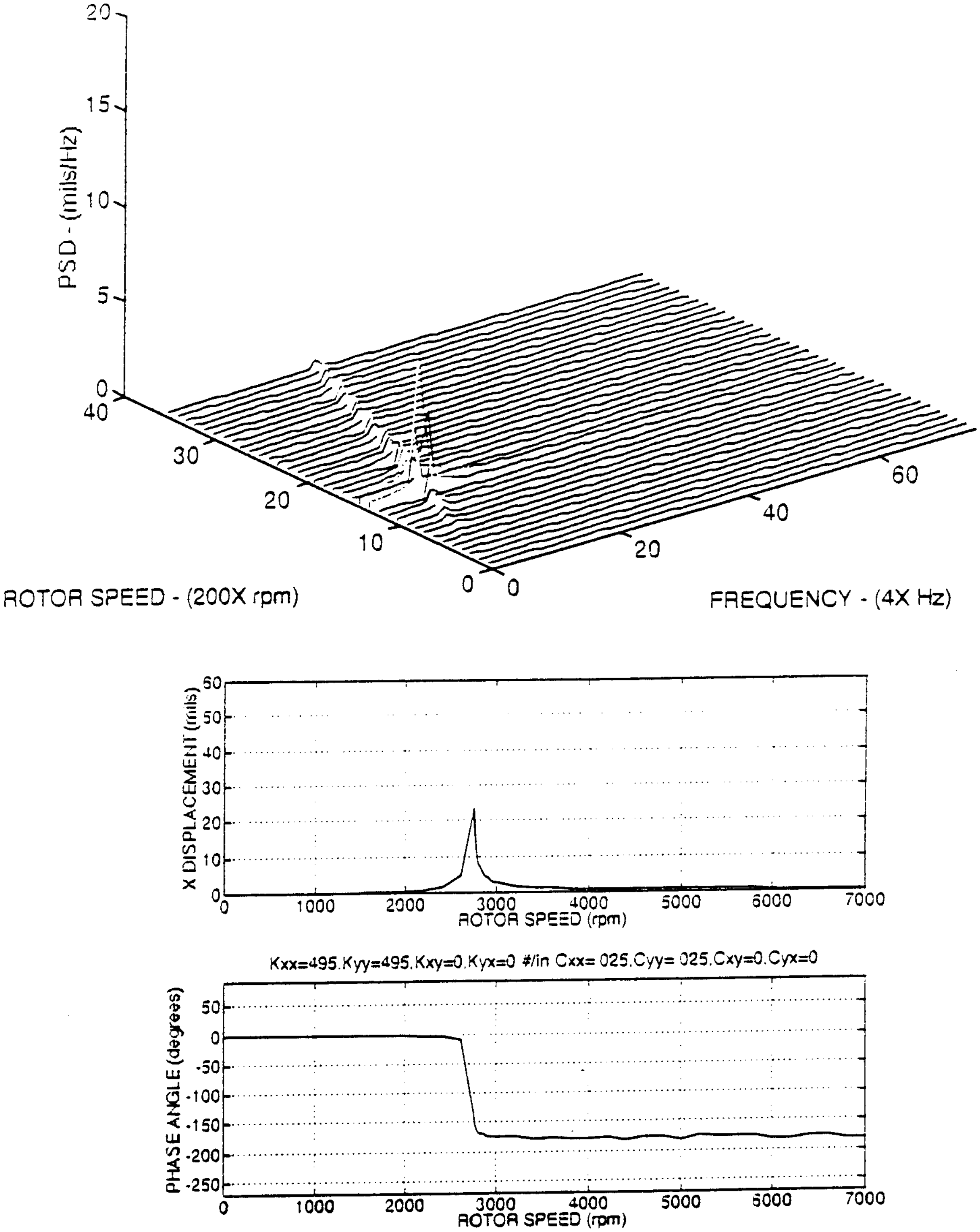

Figure 7. Cascade Plot and Phase Diagram From Analytic Model For Kxx = 495 lbf/in, Kyy = 495 lbf/in, Kxy = 0 lbf/in, Kyx = 0 lbf/in, Cxx = .025, Cyy = .025, Cxy = 0, Cyx = 0

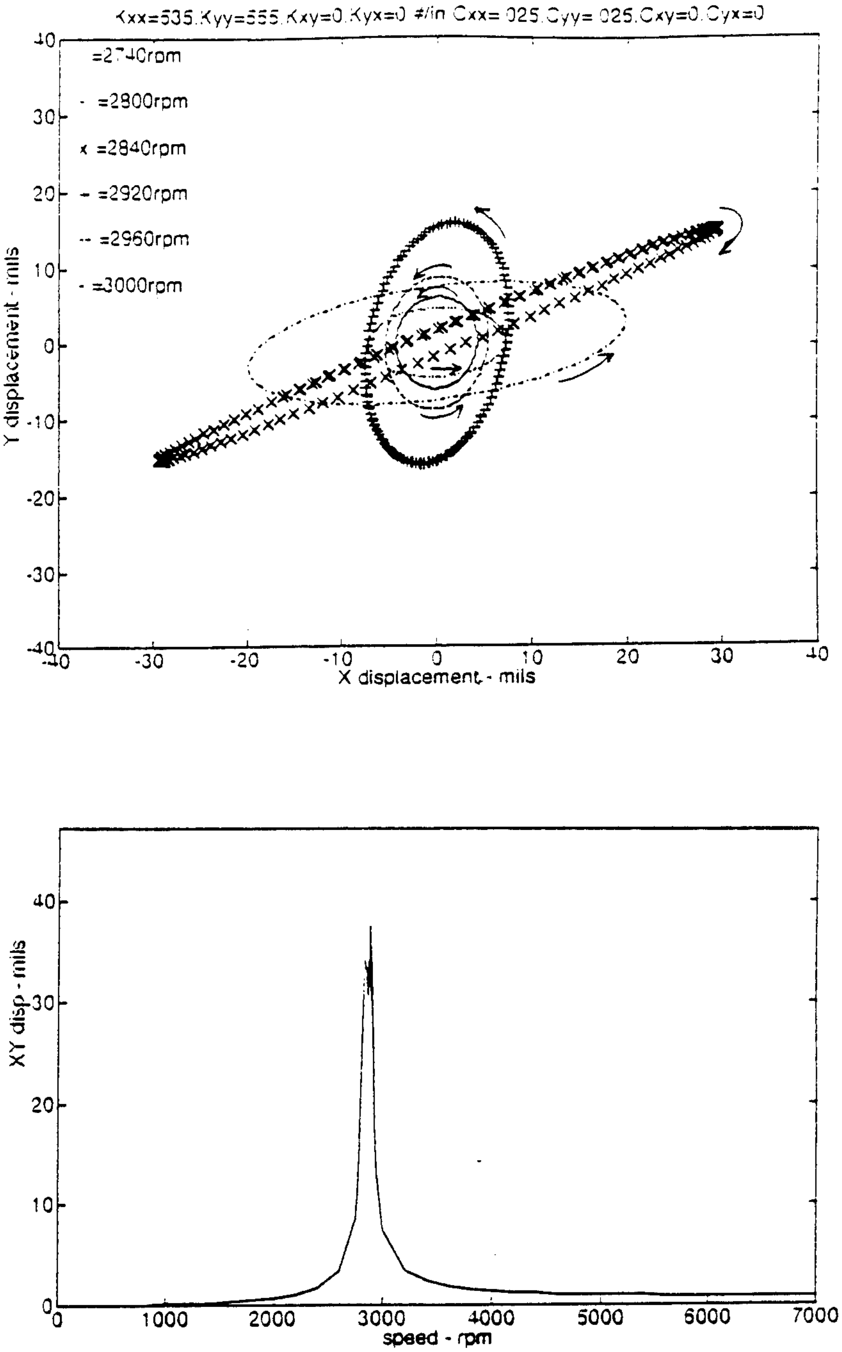

Figure 8. Rotor Orbits and Displacements From Analytic Model For Kxx = 535 lbf/in, Kyy = 555 lbf/in, Kxy = 0 lbf/in, Kyx = 0 lbf/in, Cxx = .025, Cyy = .025, Cxy = 0, Cyx = 0

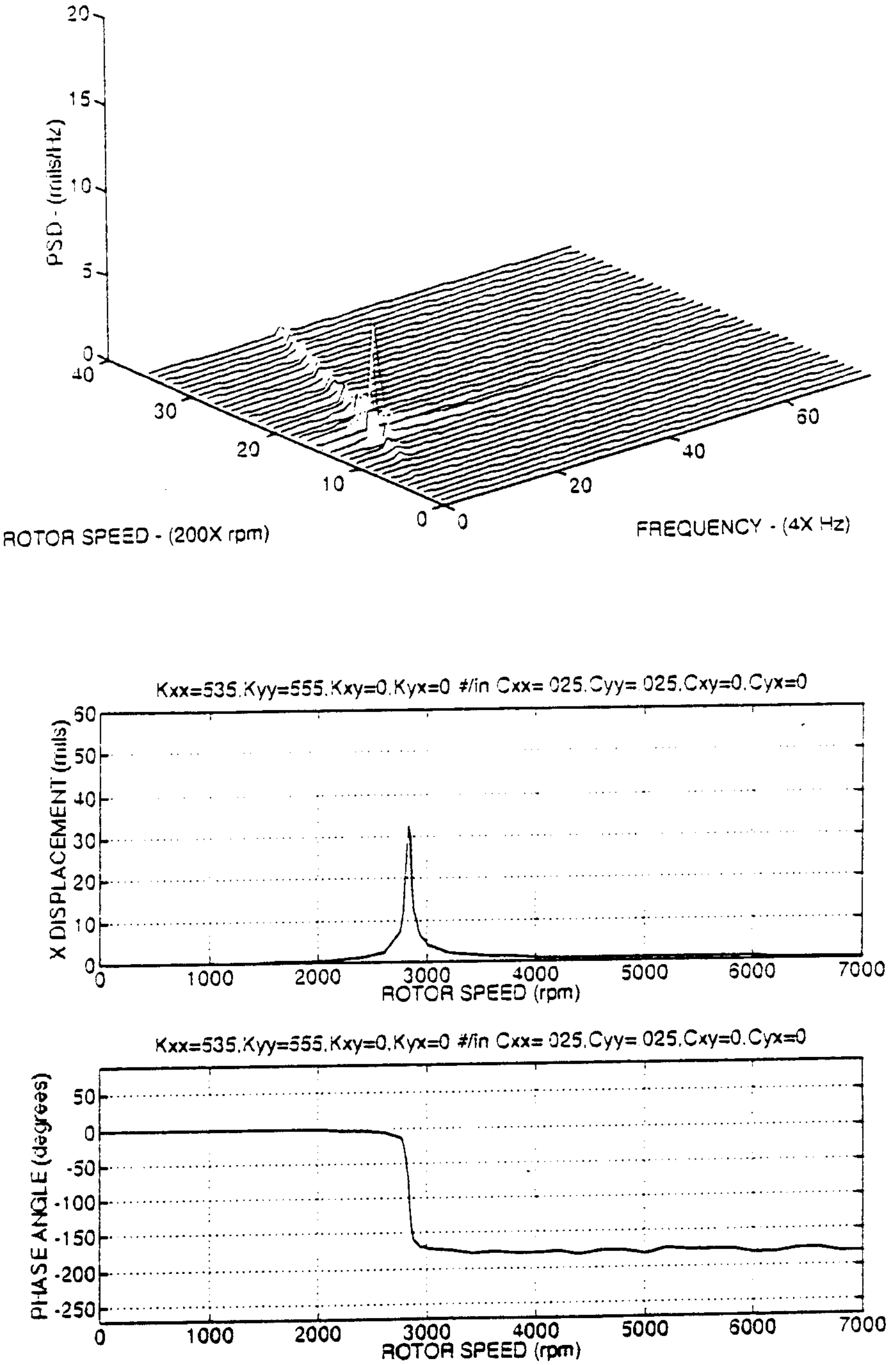

Figure 9. Cascade Plot and Phase Diagram From Analytic Model For Kxx = 535 lbf/in, Kyy = 555 lbf/in, Kxy = 0 lbf/in, Kyx = 0 lbf/in, Cxx = .025, Cyy = .025, Cxy = 0, Cyx = 0

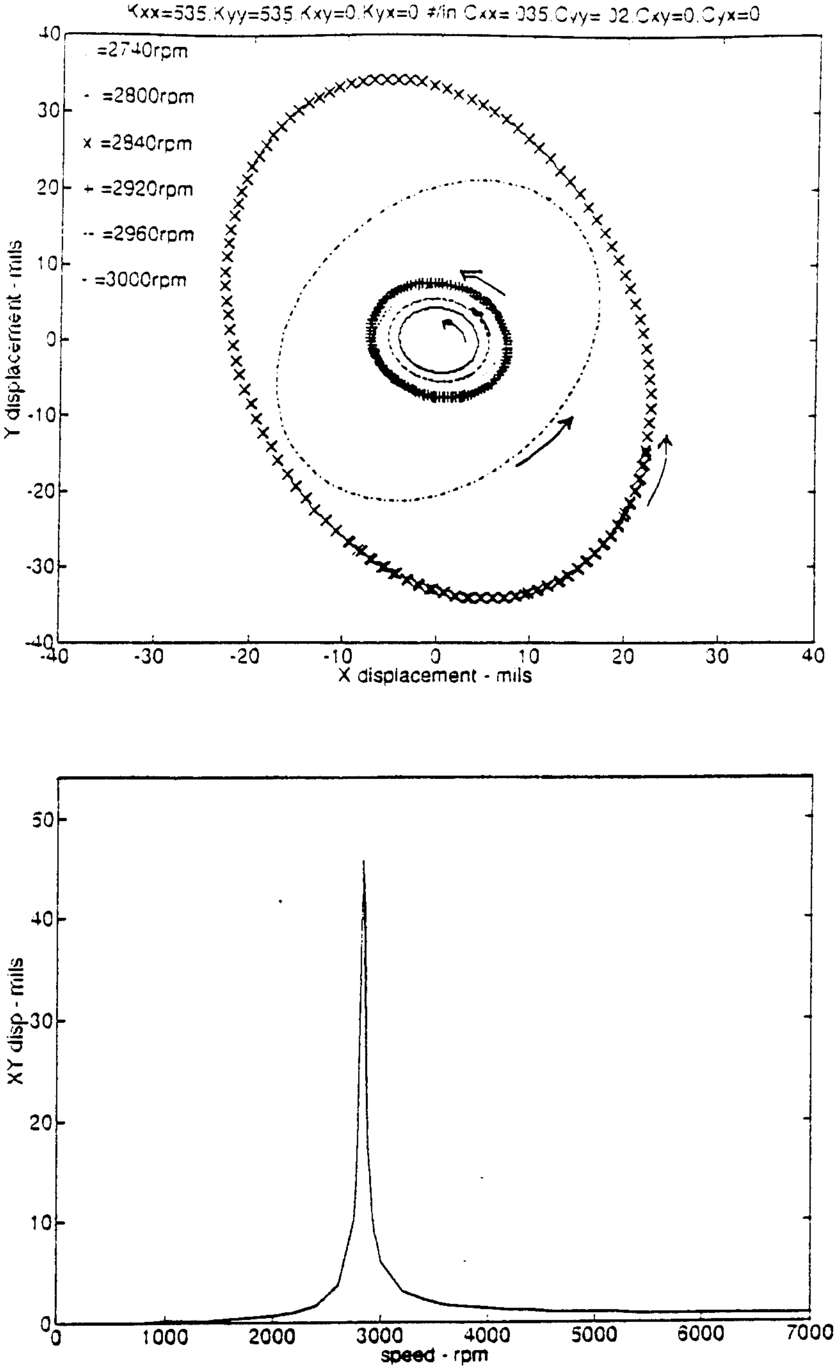

Figure 10. Rotor Orbits and Displacements From Analytic Model For Kxx = 535 lbf/in, Kyy = 535 lbf/in, Kxy = 0 lbf/in, Kyx = 0 lbf/in, Cxx = .035, Cyy = .02, Cxy = 0, Cyx = 0

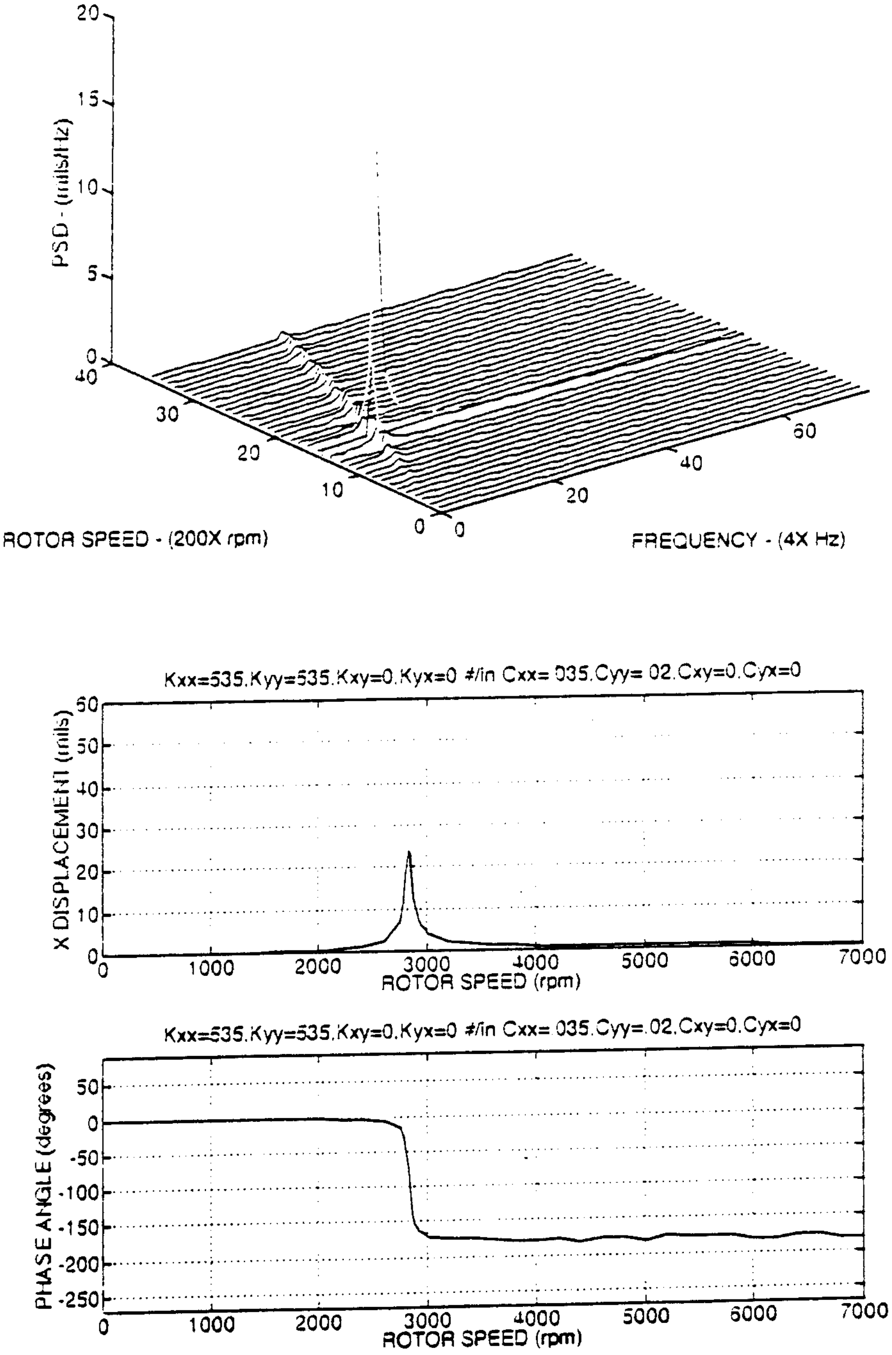

Figure 11. **Cascade Plot and Phase Diagram From Analytic Model For Kxx = 535 lbf/in, Kyy = 535 lbf/in, Kxy = 0 lbf/in, Kyx = 0 lbf/in, Cxx = .035, Cyy = .02, Cxy = 0, Cyx = 0**

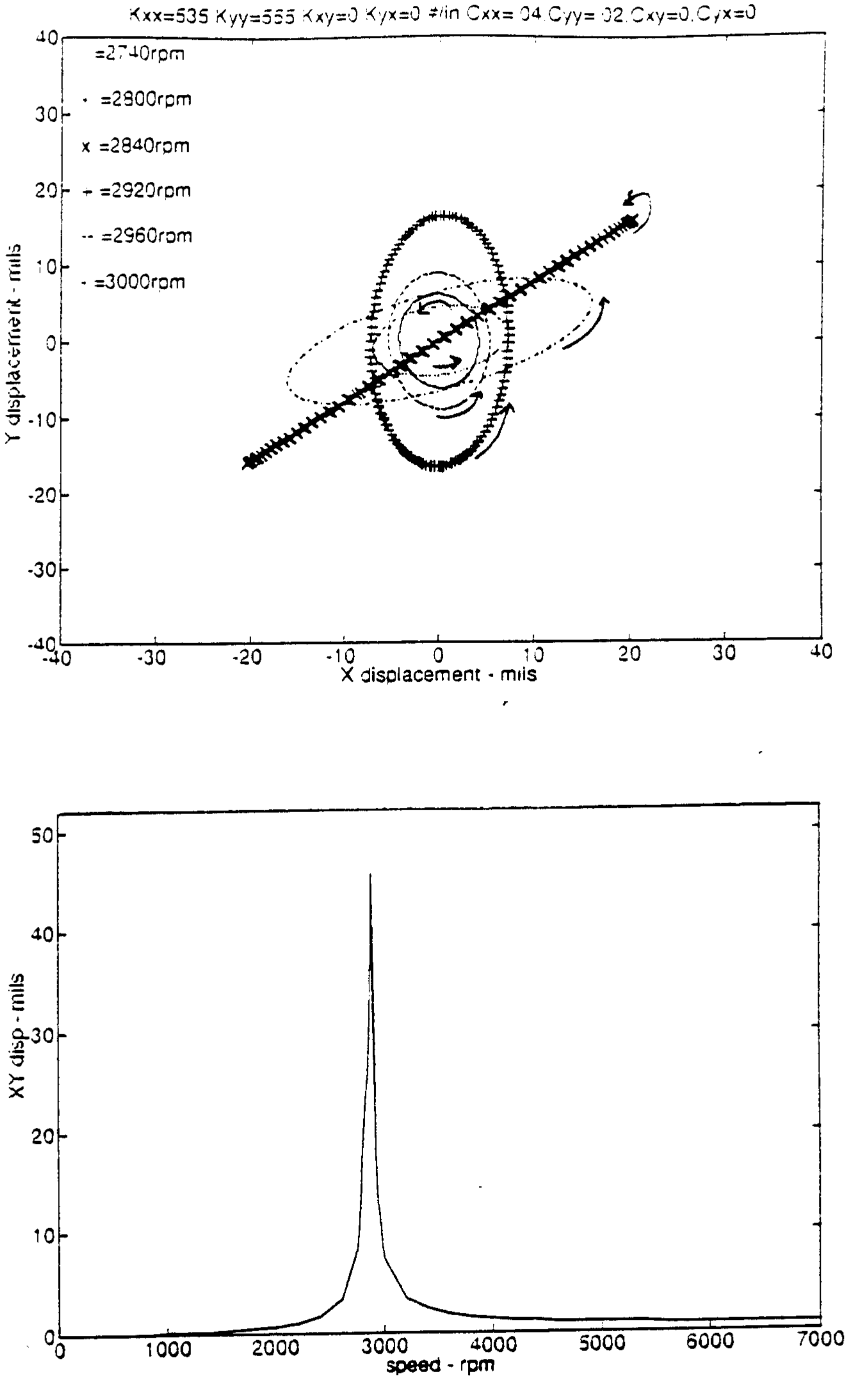

Figure 12. Rotor Orbits and Displacements From Analytic Model For Kxx = 535 lbf/in, Kyy = 555 lbf/in, Kxy = 0 lbf/in, Kyx = 0 lbf/in, Cxx = .04, Cyy = .02, Cxy = 0, Cyx = 0

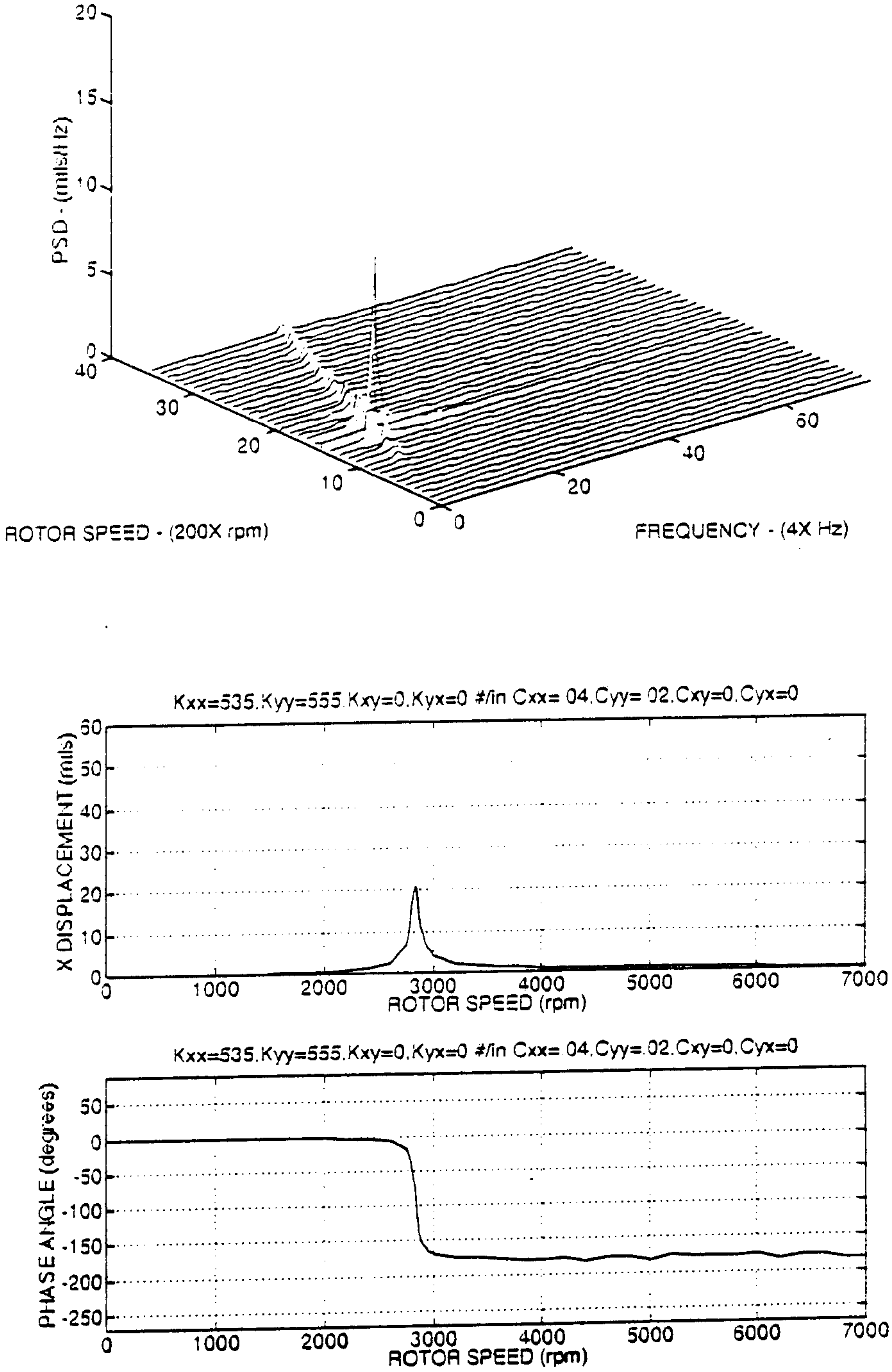

Figure 13. Cascade Plot and Phase Diagram From Analytic Model For Kxx = 535 lbf/in, Kyy = 555 lbf/in, Kxy = 0 lbf/in, Kyx = 0 lbf/in, Cxx = .04, Cyy = .02, Cxy = 0, Cyx = 0

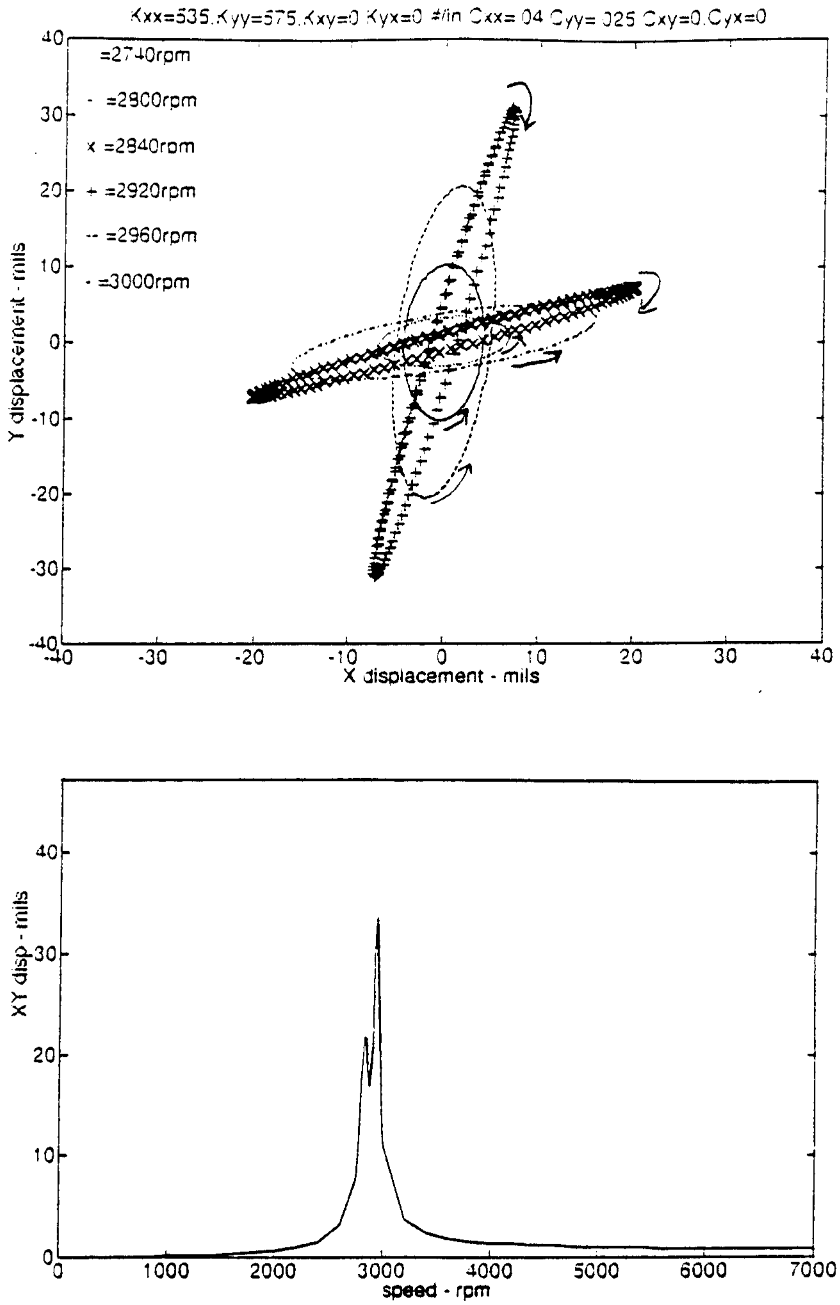

Figure 14. Rotor Orbits and Displacements From Analytic Model For Kxx = 535 lbf/in, Kyy = 575 lbf/in, Kxy = 0 lbf/in, Kyx = 0 lbf/in, Cxx = .04, Cyy = .025, Cxy = 0, Cyx = 0

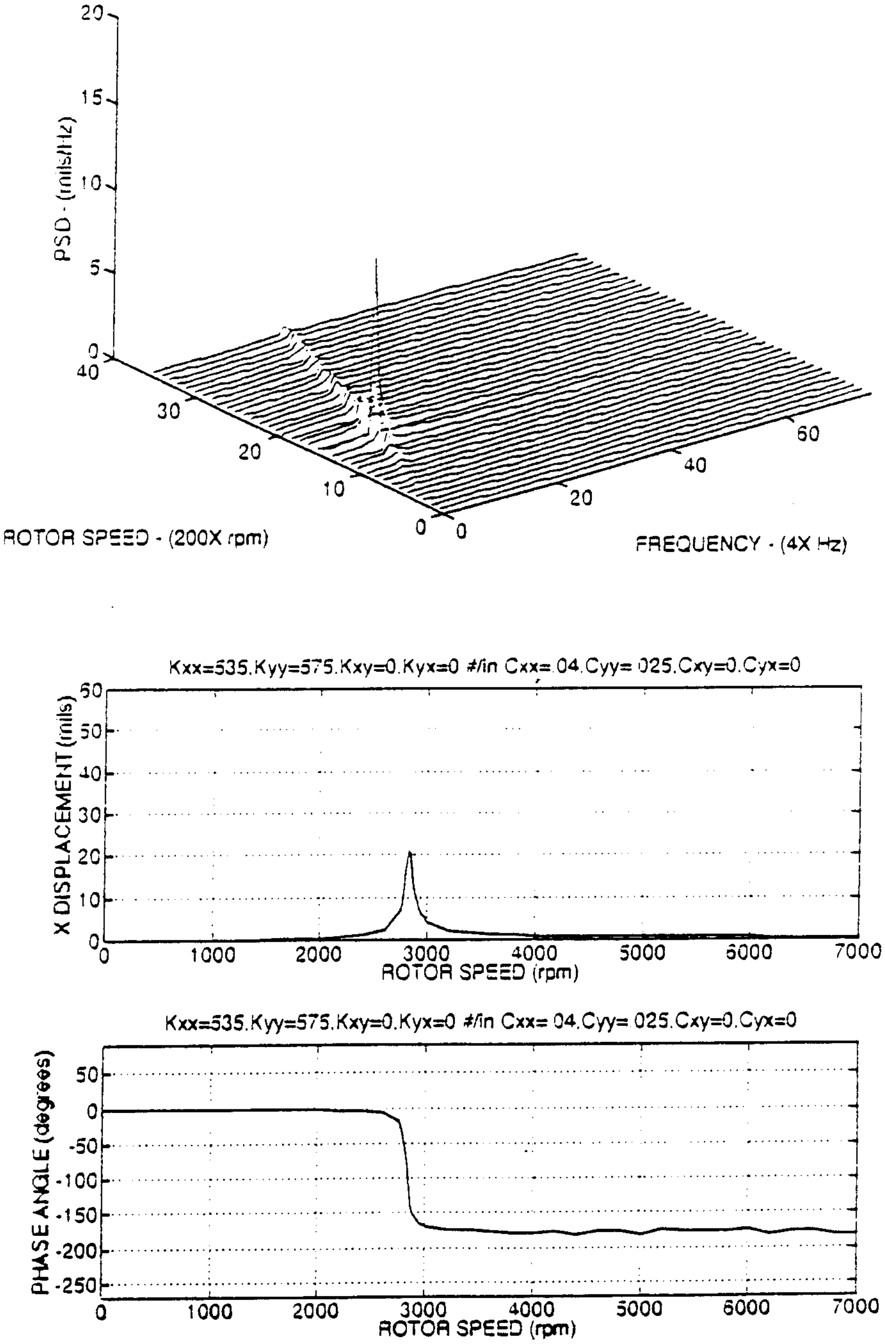

Kxx=535.Kyy=575.Kxy=0.Kyx=0 #/in Cxx=.04.Cyy=.025.Cxy=0.Cyx=0

Kxx=535.Kyy=575.Kxy=0.Kyx=0 #/in Cxx=.04.Cyy=.025.Cxy=0.Cyx=0

Figure 15. Cascade Plot and Phase Diagram From Analytic Model For Kxx = 535 lbf/in, Kyy = 575 lbf/in, Kxy = 0 lbf/in, Kyx = 0 lbf/in, Cxx = .04, Cyy = .025, Cxy = 0, Cyx = 0

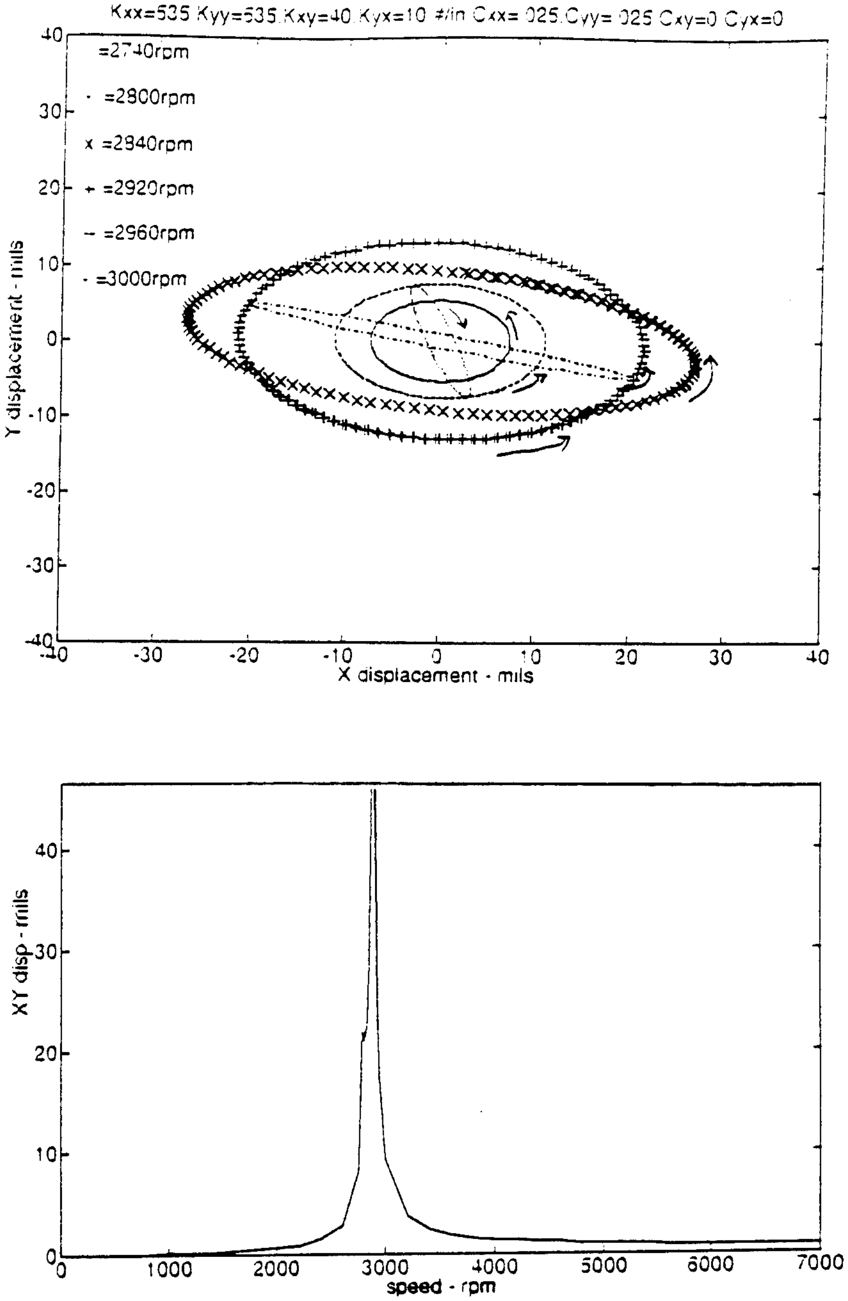

Figure 16. Rotor Orbits and Displacements From Analytic Model For Kxx = 535 lbf/in, Kyy = 535 lbf/in, Kxy = 40 lbf/in, Kyx = 10 lbf/in, Cxx = .025, Cyy = .025, Cxy = 0, Cyx = 0

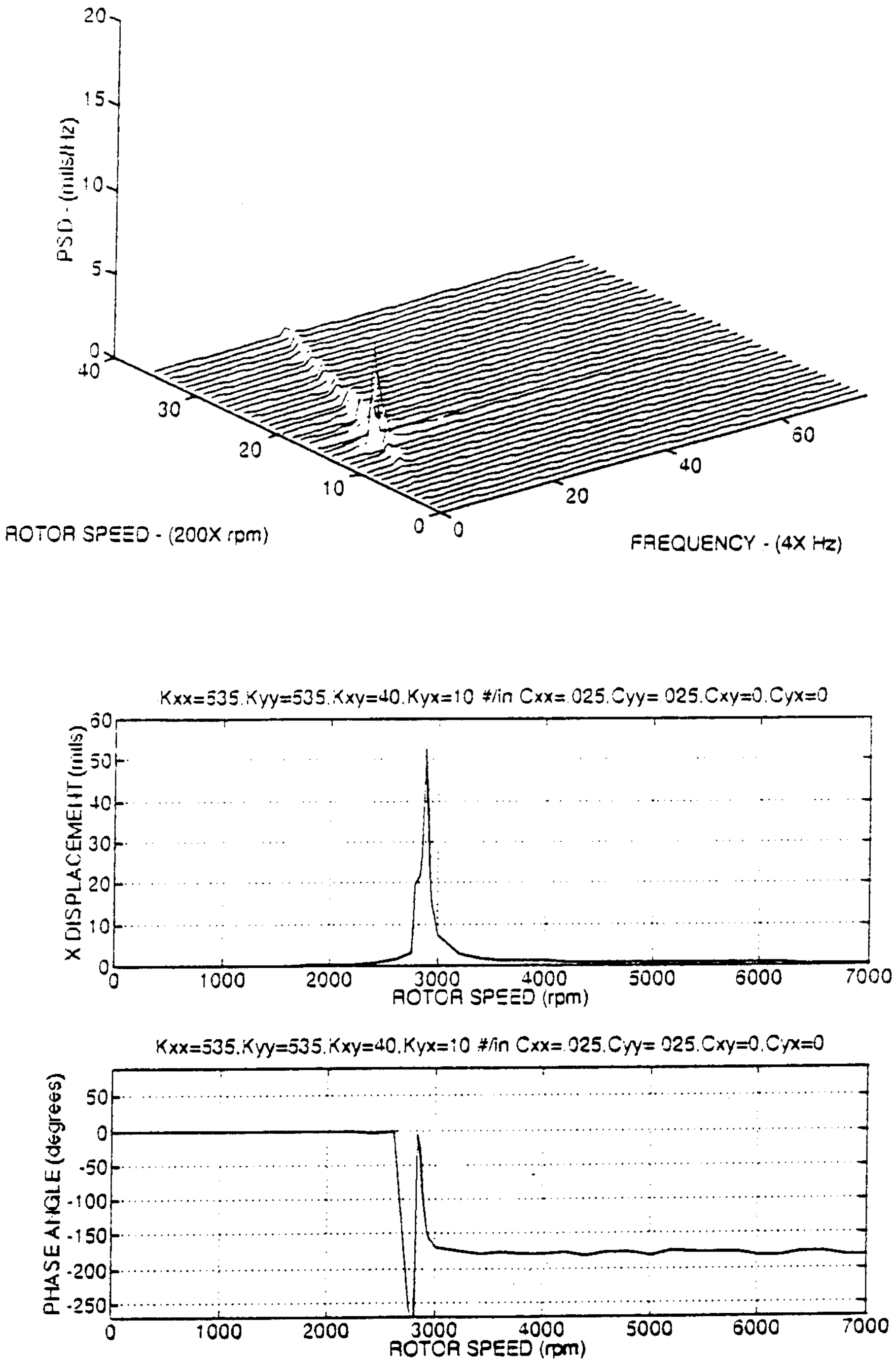

Figure 17. Cascade Plot and Phase Diagram From Analytic Model For Kxx = 535 lbf/in, Kyy = 535 lbf/in, Kxy = 40 lbf/in, Kyx = 10 lbf/in, Cxx = .025, Cyy = .025, Cxy = 0, Cyx = 0

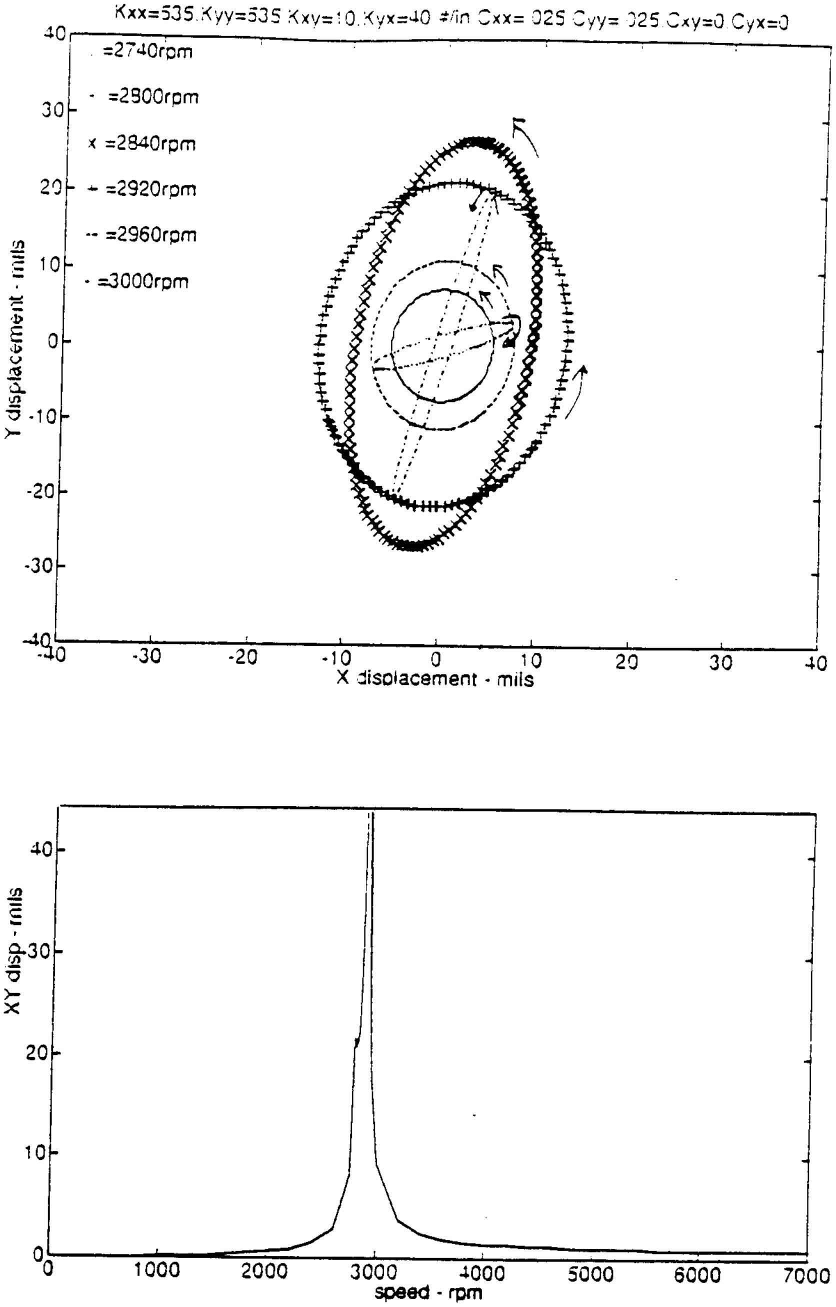

Figure 18. Rotor Orbits and Displacements From Analytic Model For Kxx = 535 lbf/in, Kyy = 535 lbf/in, Kxy = 10 lbf/in, Kyx = 40 lbf/in, Cxx = .025, Cyy = .025, Cxy = 0, Cyx = 0

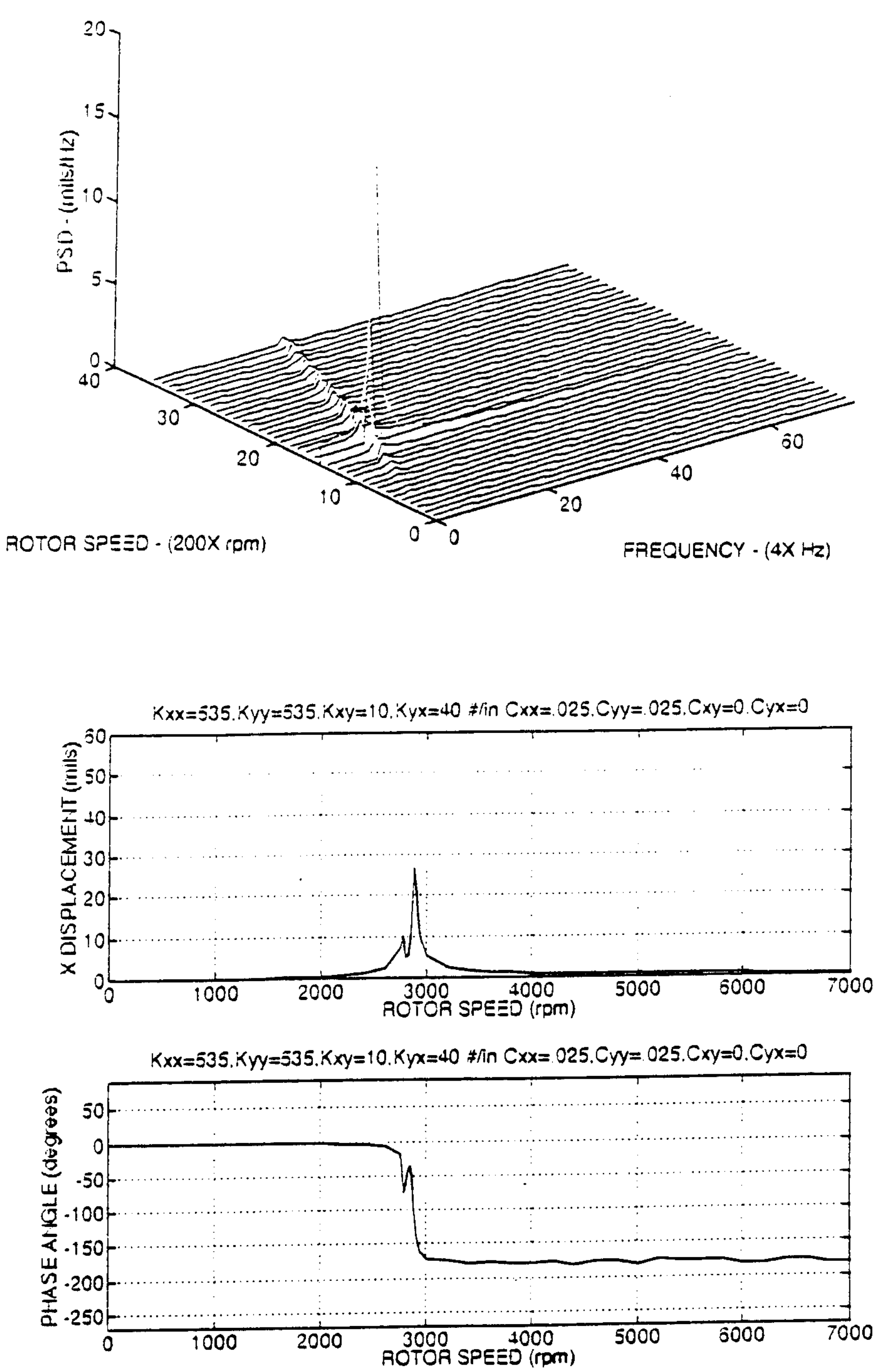

Figure 19. **Cascade Plot and Phase Diagram From Analytic Model For Kxx = 535 lbf/in, Kyy = 535 lbf/in, Kxy = 10 lbf/in, Kyx = 40 lbf/in, Cxx = .025, Cyy = .025, Cxy = 0, Cyx = 0**

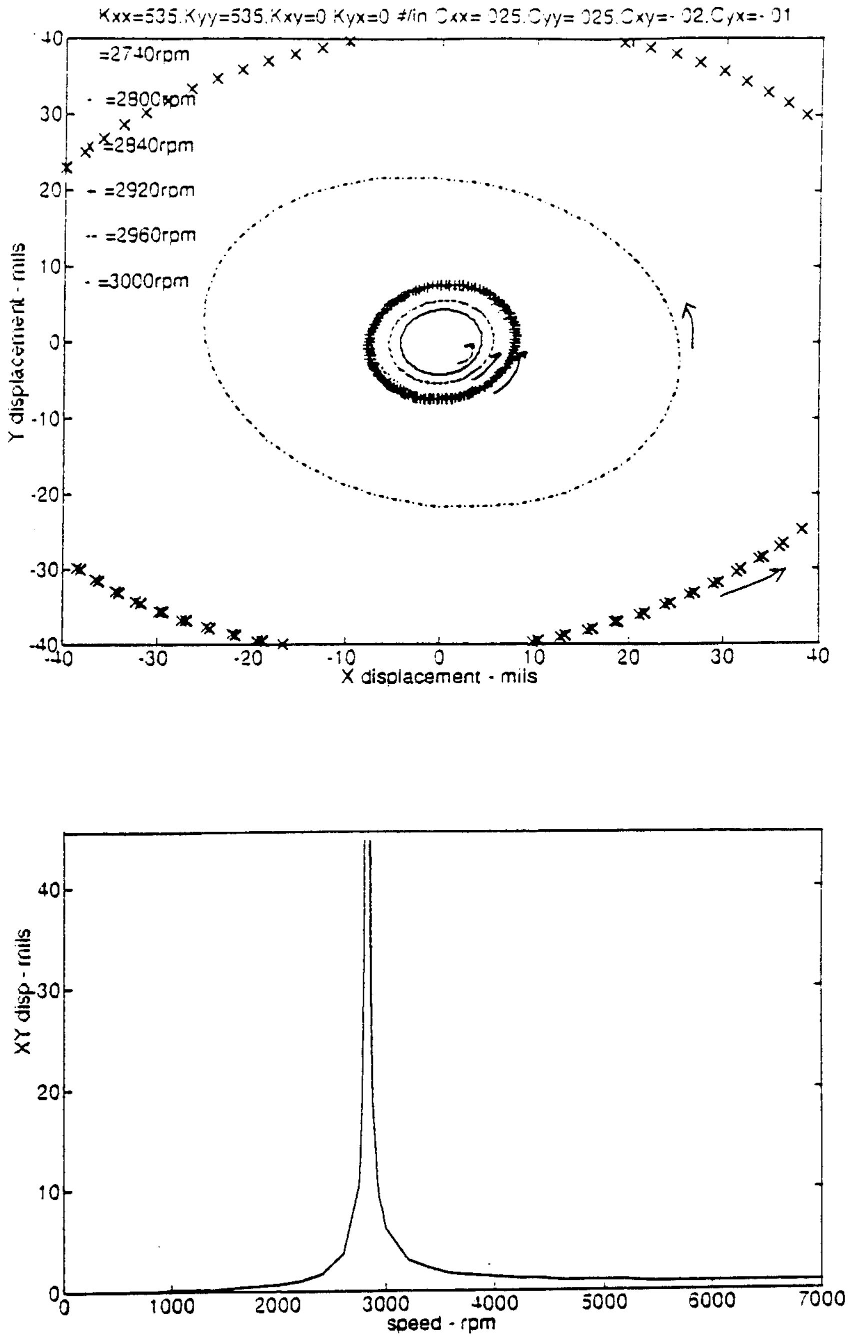

Figure 20. Rotor Orbits and Displacements From Analytic Model For Kxx = 535 lbf/in, Kyy = 535 lbf/in, Kxy = 0 lbf/in, Kyx = 0 lbf/in, Cxx = .025, Cyy = .025, Cxy = -.02, Cyx = -.01

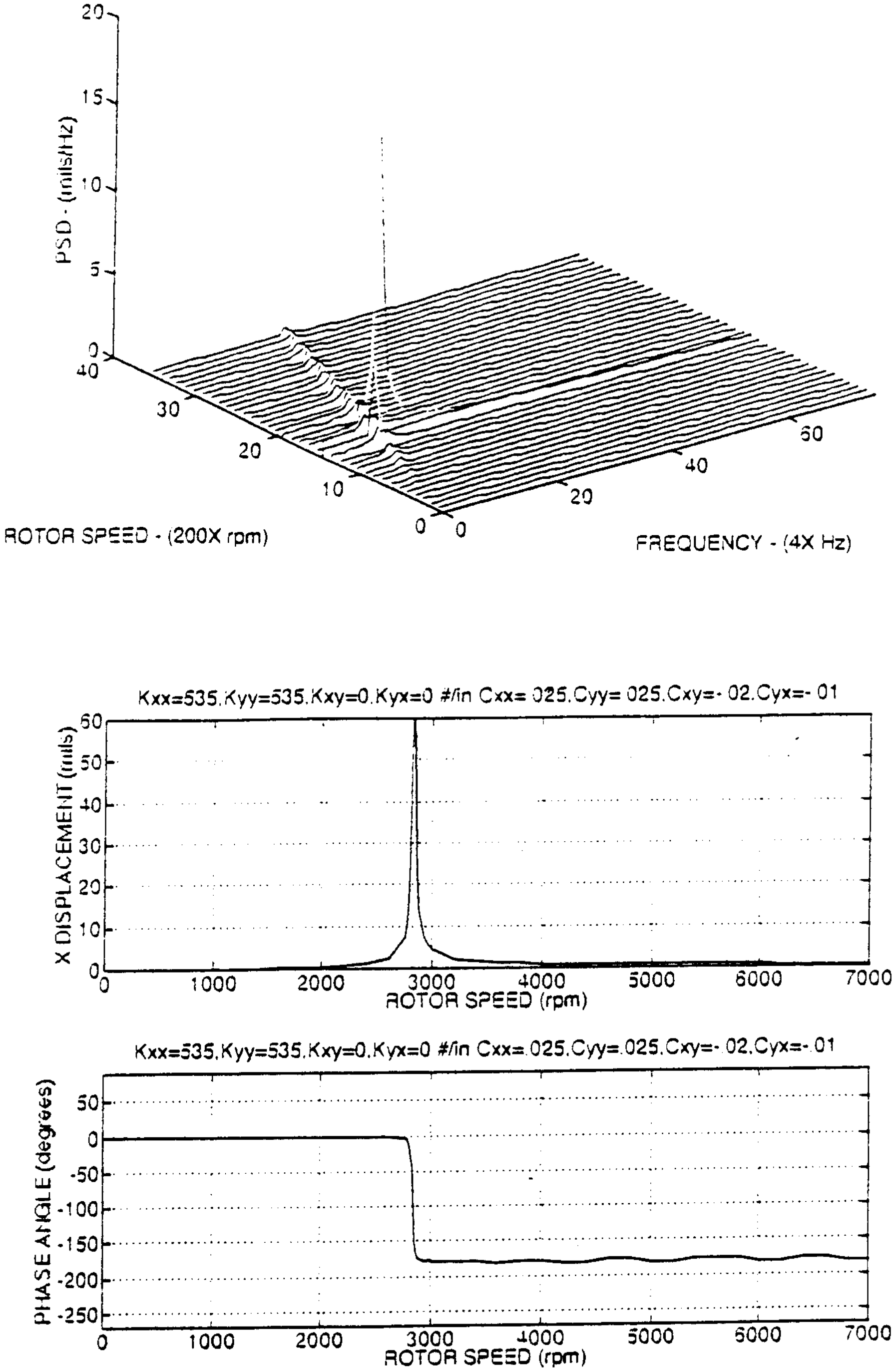

Figure 21. Cascade Plot and Phase Diagram From Analytic Model For Kxx = 535 lbf/in, Kyy = 535 lbf/in, Kxy = 0 lbf/in, Kyx = 0 lbf/in, Cxx = .025, Cyy = .025, Cxy = -.02, Cyx = -.01

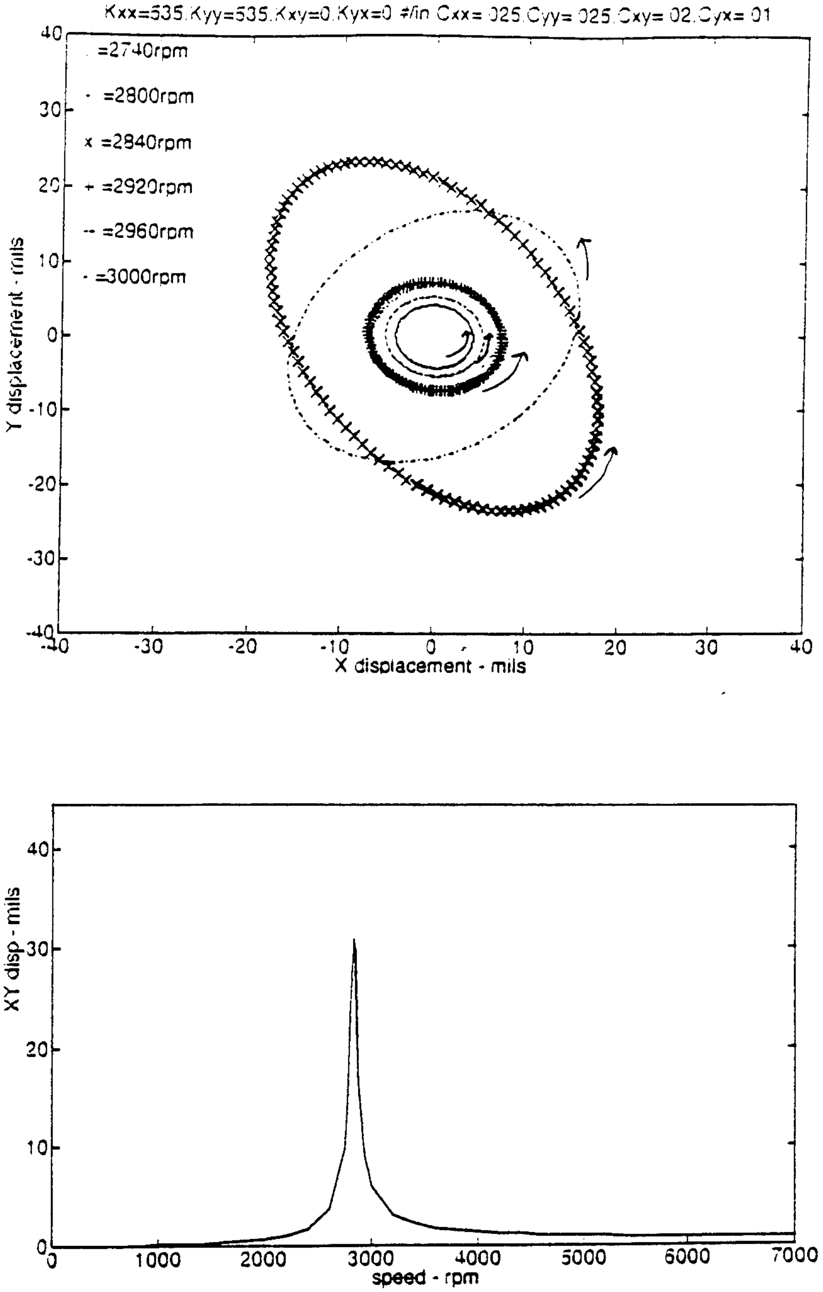

Figure 22. **Rotor Orbits and Displacements From Analytic Model For Kxx = 535 lbf/in, Kyy = 535 lbf/in, Kxy = 0 lbf/in, Kyx = 0 lbf/in, Cxx = .025, Cyy = .025, Cxy = .02, Cyx = .01**

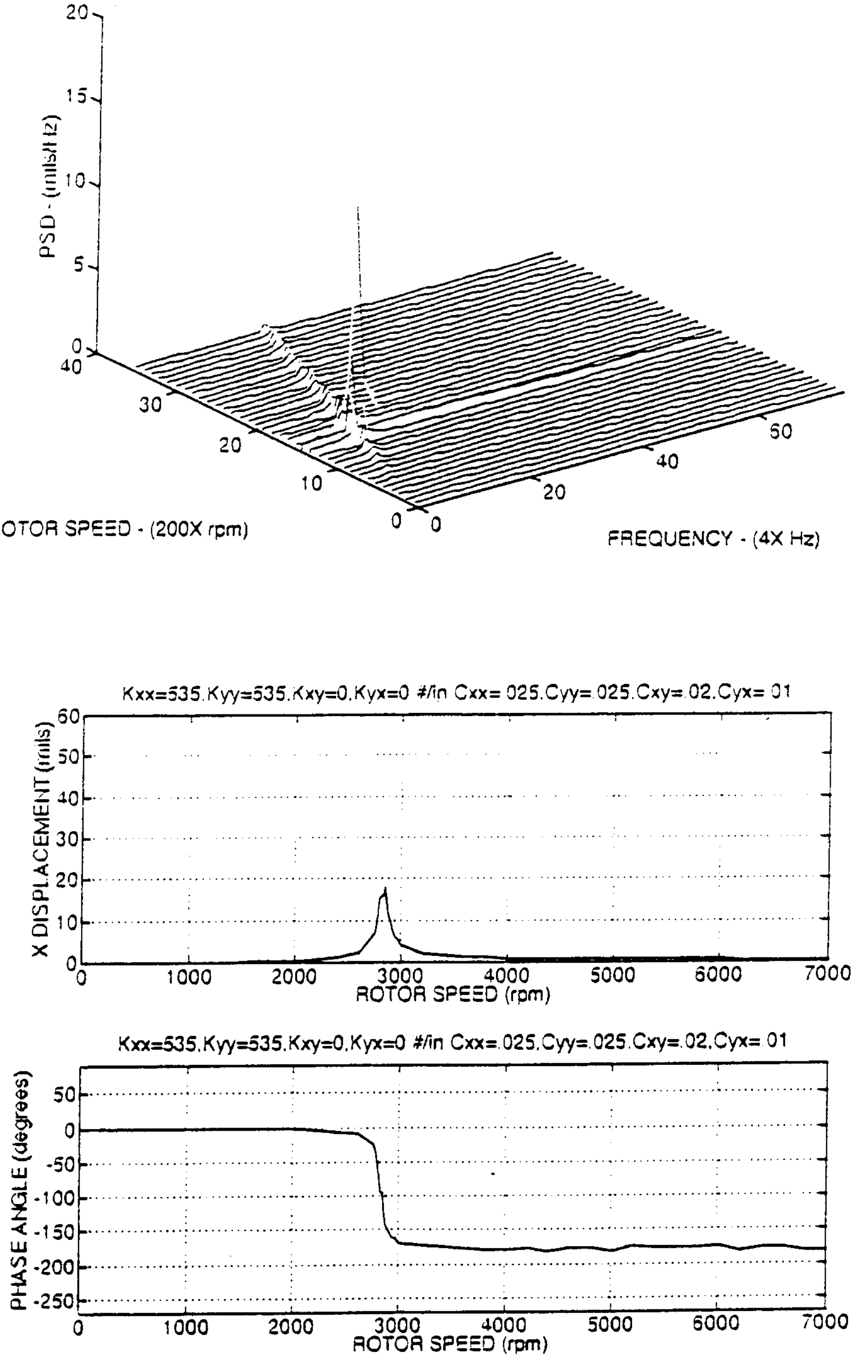

Figure 23. Cascade Plot and Phase Diagram From Analytic Model For Kxx = 535 lbf/in, Kyy = 535 lbf/in, Kxy = 0 lbf/in, Kyx = 0 lbf/in, Cxx = .025, Cyy = .025, Cxy = .02, Cyx = .01

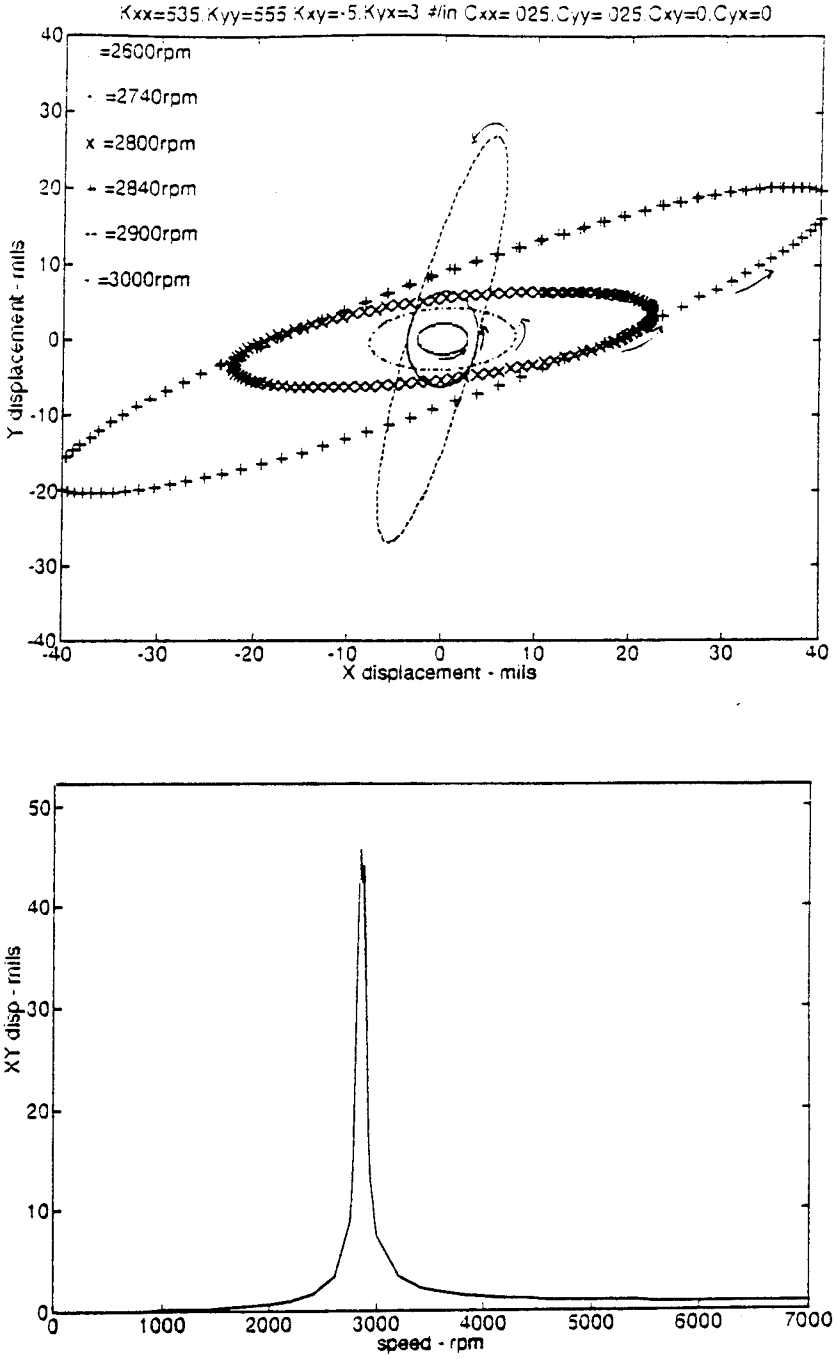

Figure 24. Rotor Orbits and Displacements From Analytic Model For Kxx = 535 lbf/in, Kyy = 555 lbf/in, Kxy = -5 lbf/in, Kyx = 3 lbf/in, Cxx = .025, Cyy = .025, Cxy = 0, Cyx = 0

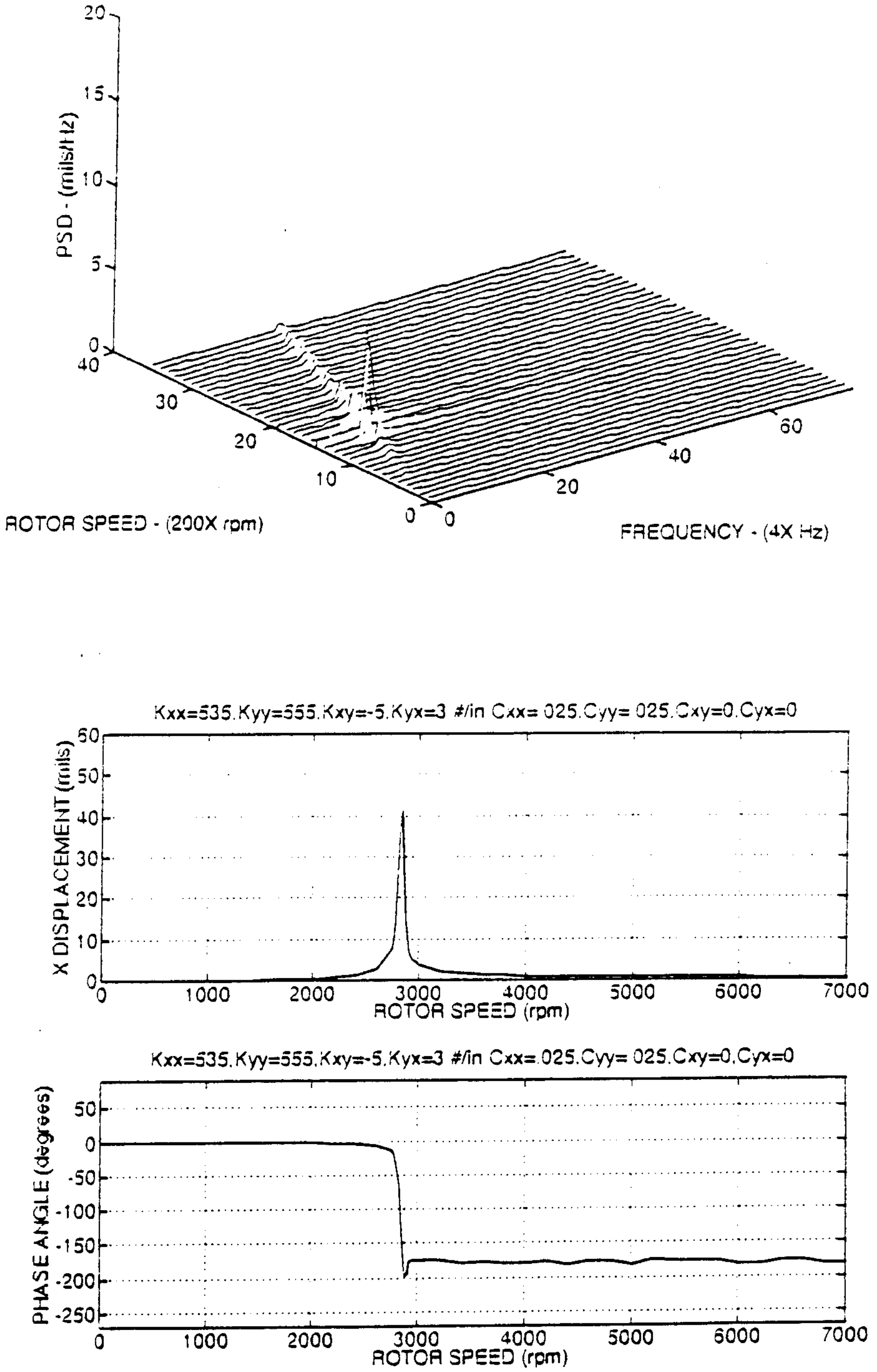

Figure 25. **Cascade Plot and Phase Diagram From Analytic Model For Kxx = 535 lbf/in, Kyy = 555 lbf/in, Kxy = -5 lbf/in, Kyx = 3 lbf/in, Cxx = .025, Cyy = .025, Cxy = 0, Cyx = 0**

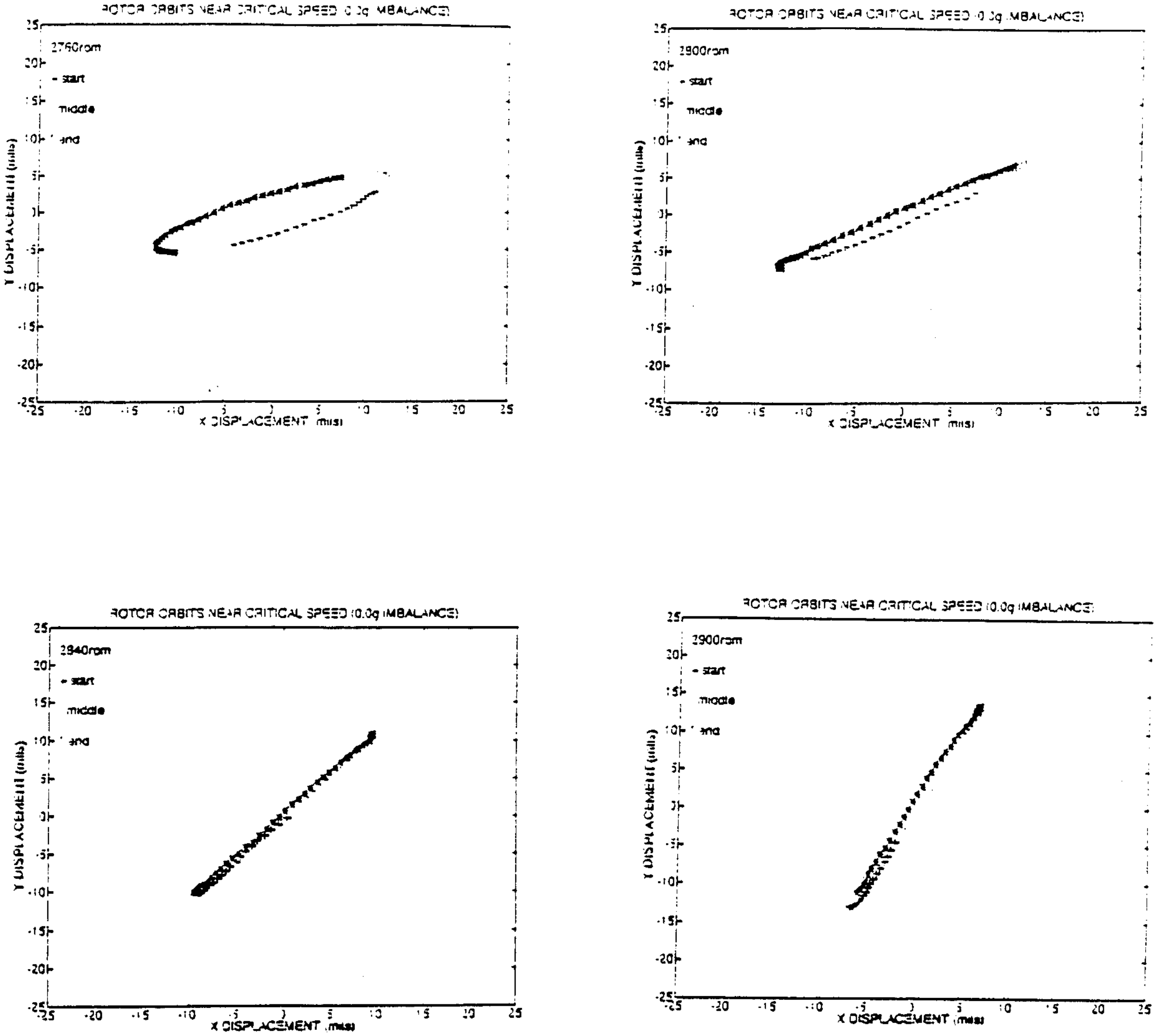

Figure 26. Rotor Orbits No Imbalance Good Bearing. Speeds from 2760 to 2900 rpm.

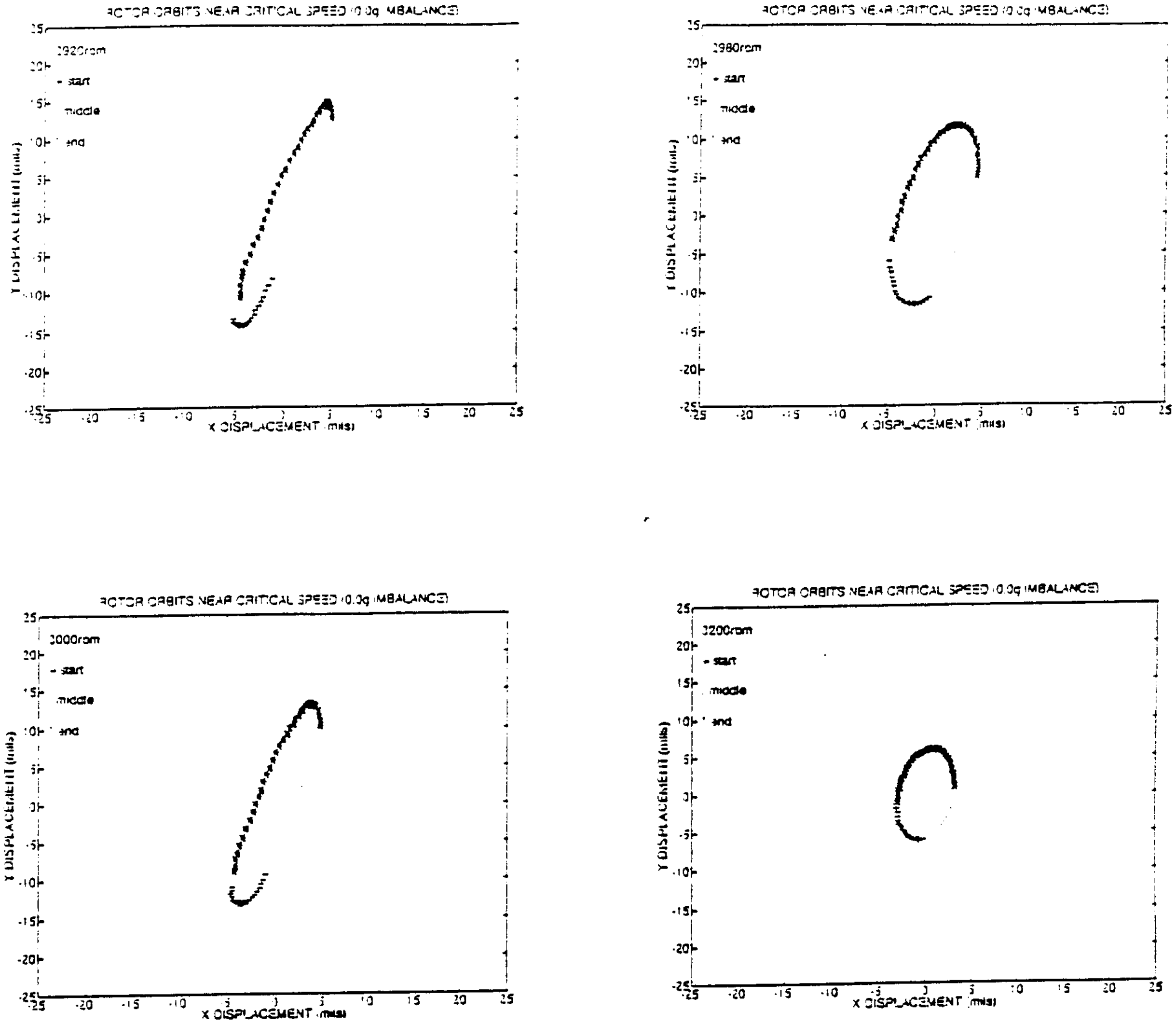

Figure 27. Rotor Orbits No Imbalance Good Bearing. Speeds from 2920 to 3200 rpm.

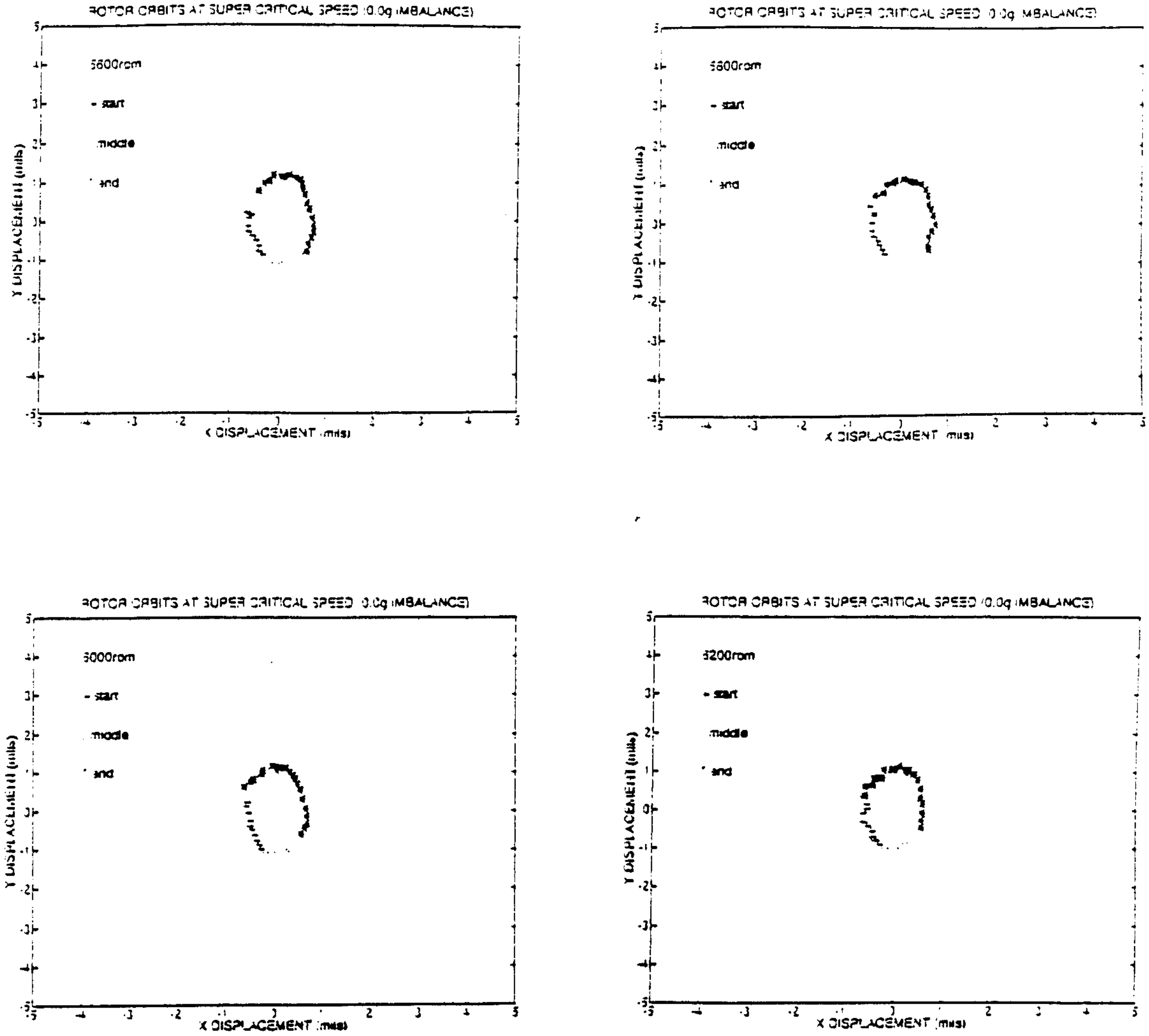

Figure 28. Rotor Orbits No Imbalance Good Bearing. Speeds from 5600 to 6200 rpm.

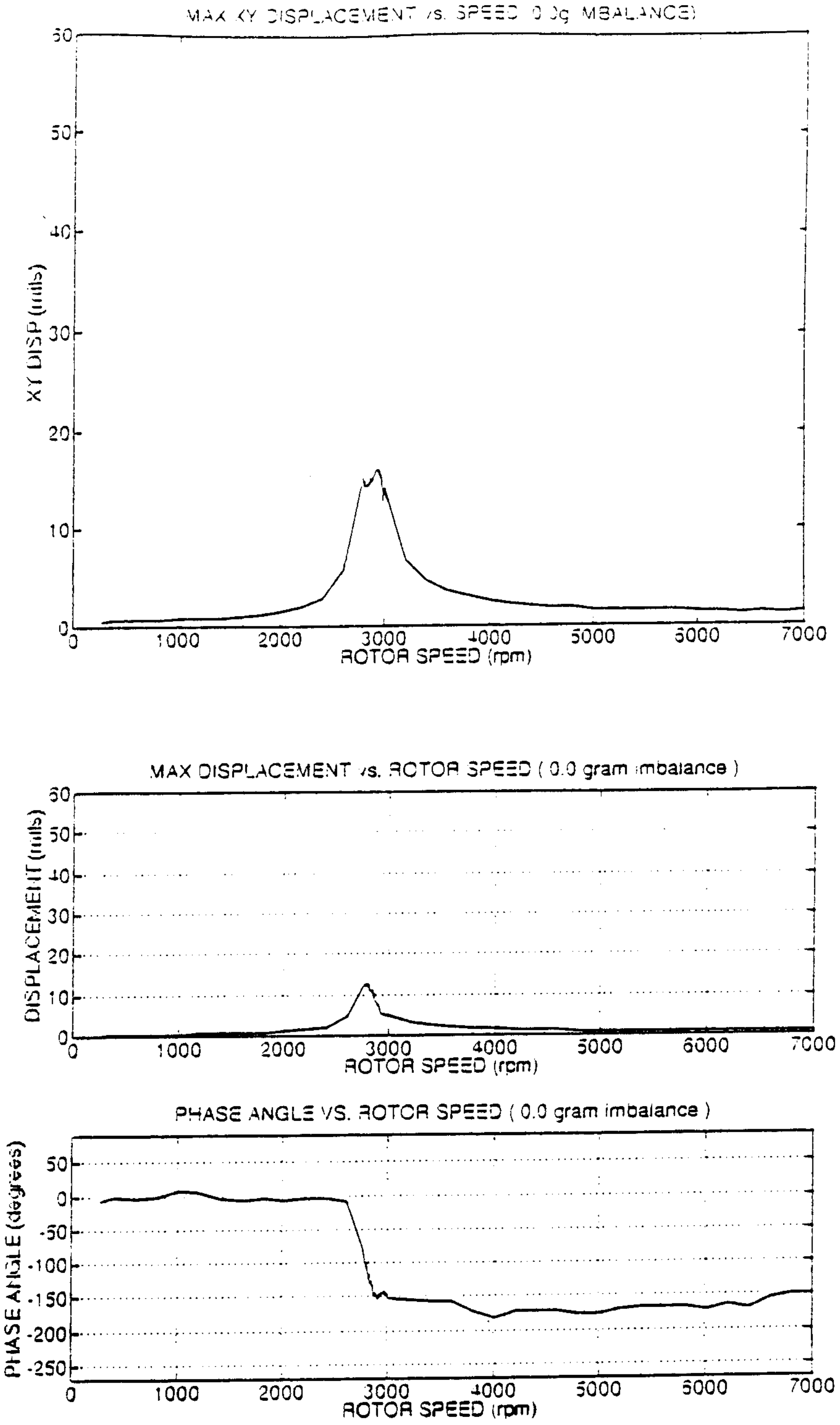

Figure 29. Maximum Displacements and Bode Plot No Imbalance Good Bearing

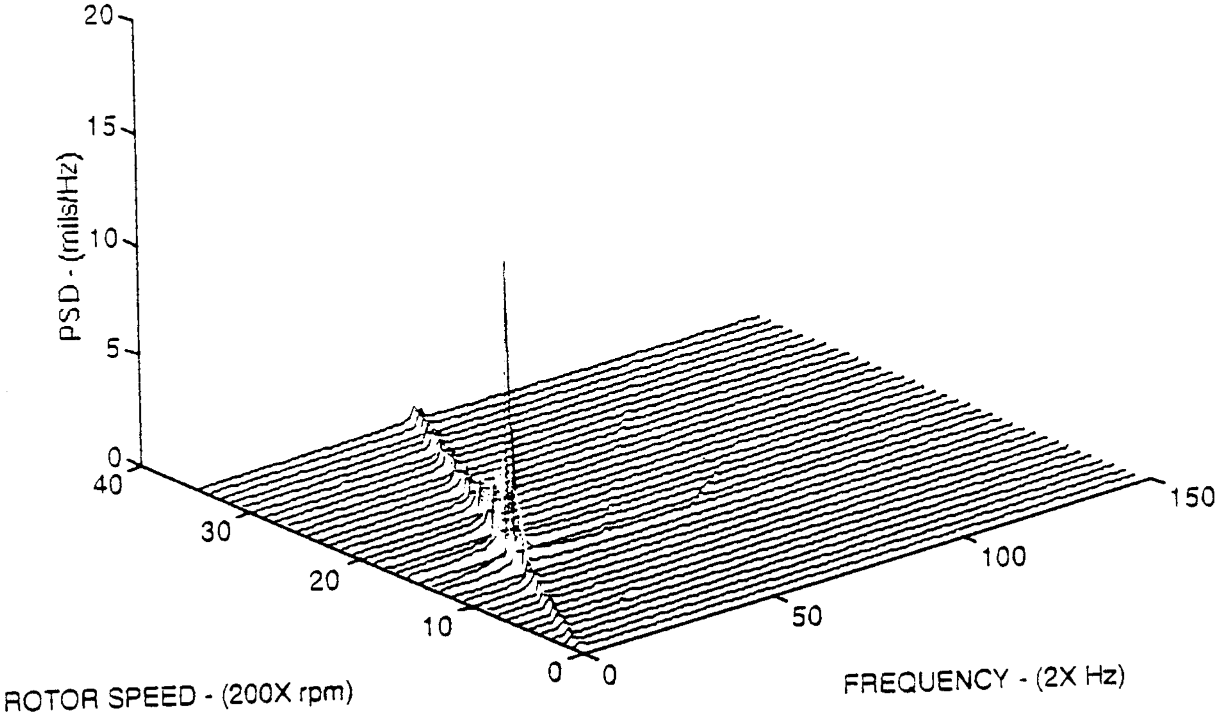

Figure 30. Cascade Plot No Imbalance Good Bearing

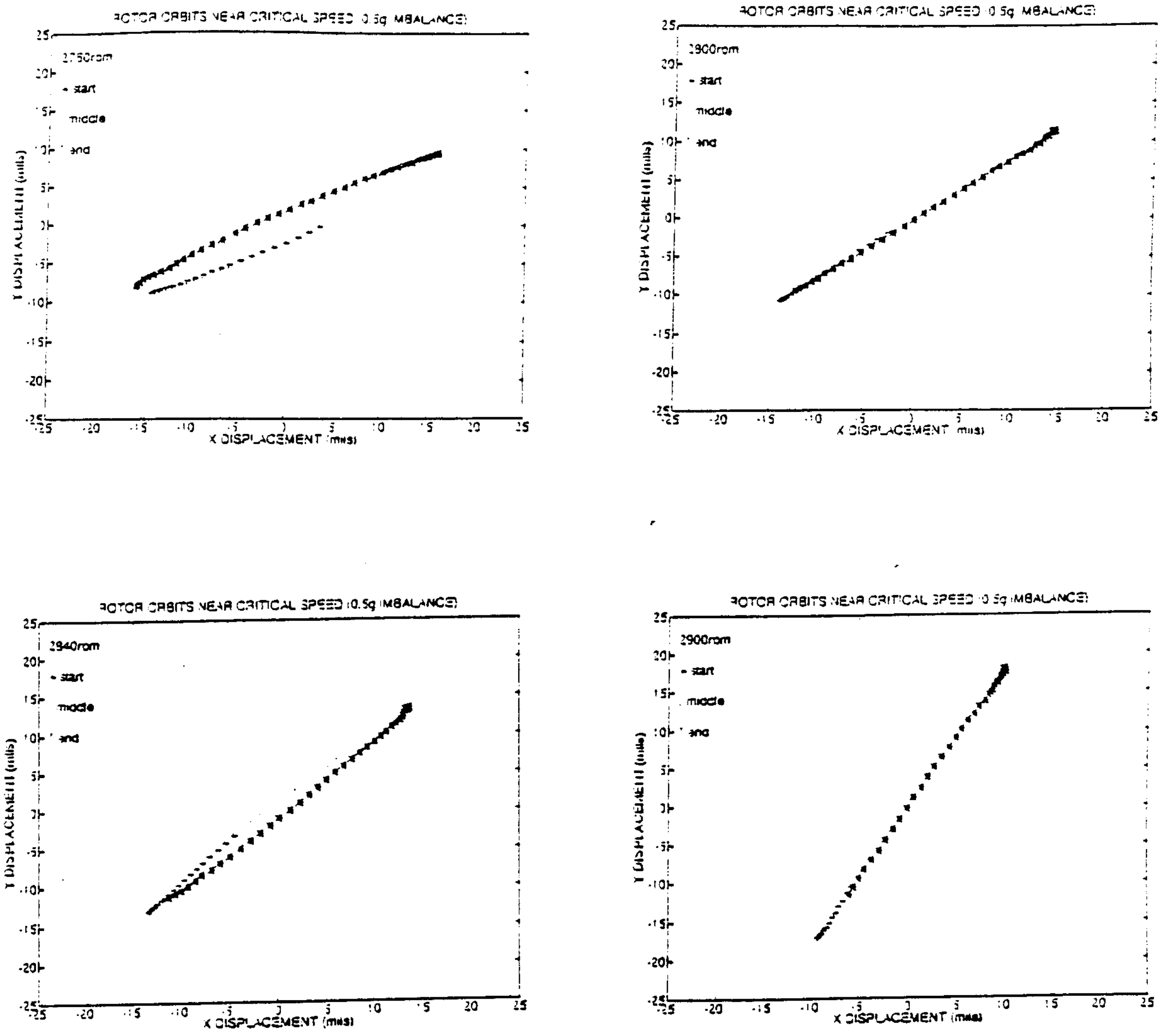

Figure 31. Rotor Orbits 0.5 Gram Imbalance Good Bearing. Speeds from 2760 to 2900 rpm.

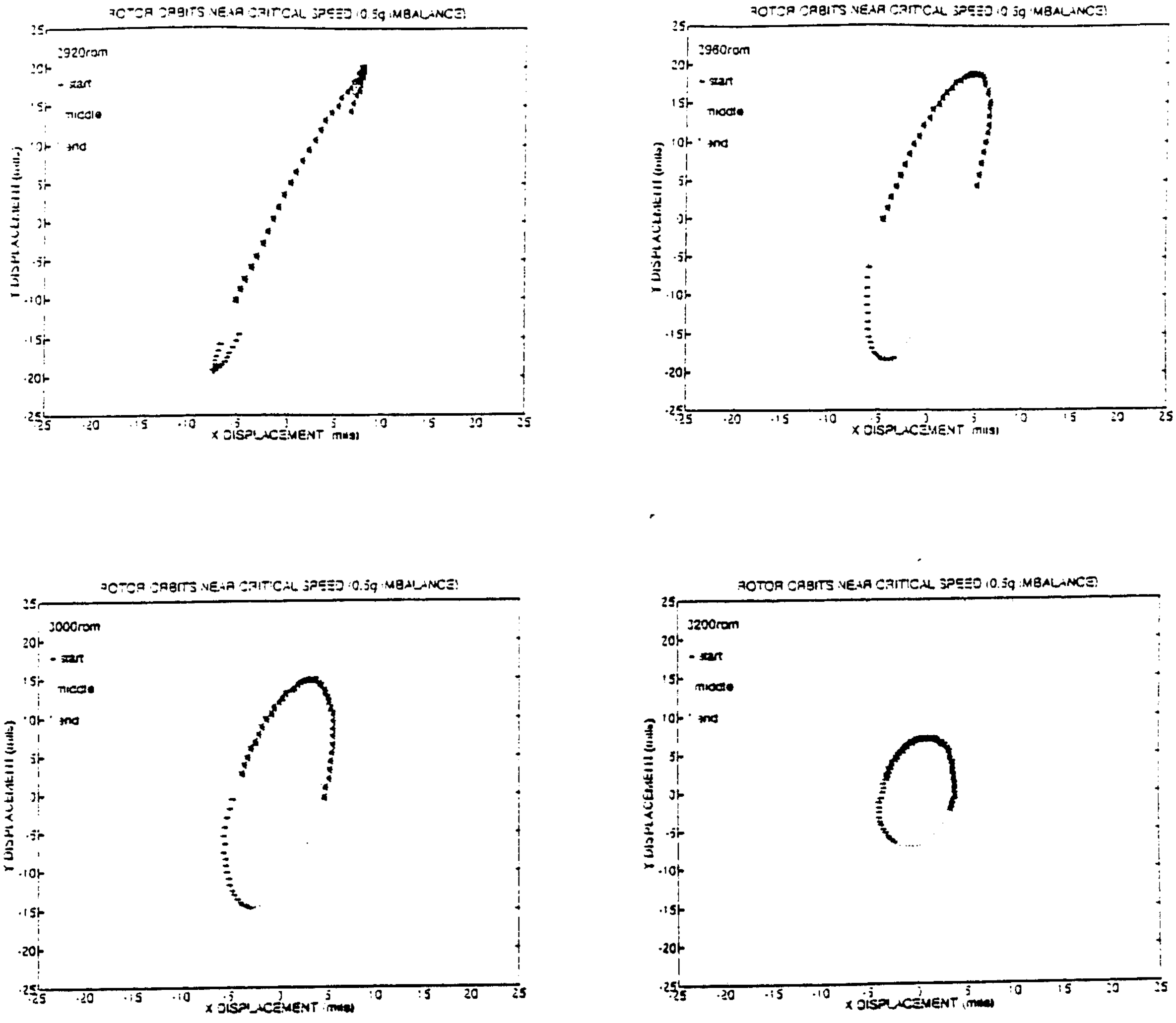

Figure 32. Rotor Orbits 0.5 Gram Imbalance Good Bearing. Speeds from 2920 to 3200 rpm.

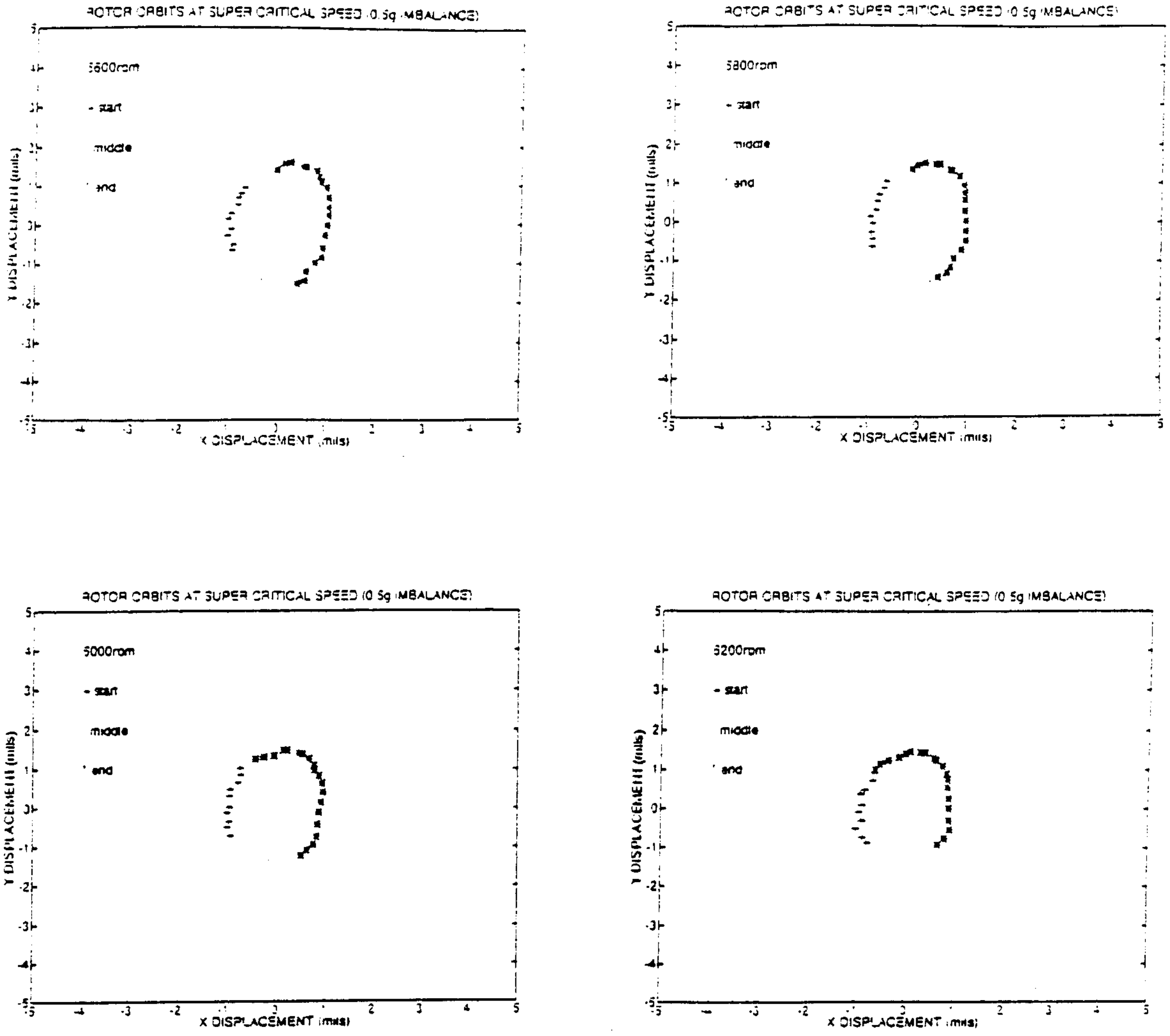

Figure 33. Rotor Orbits 0.5 Gram Imbalance Good Bearing. Speeds from 5600 to 6200 rpm.

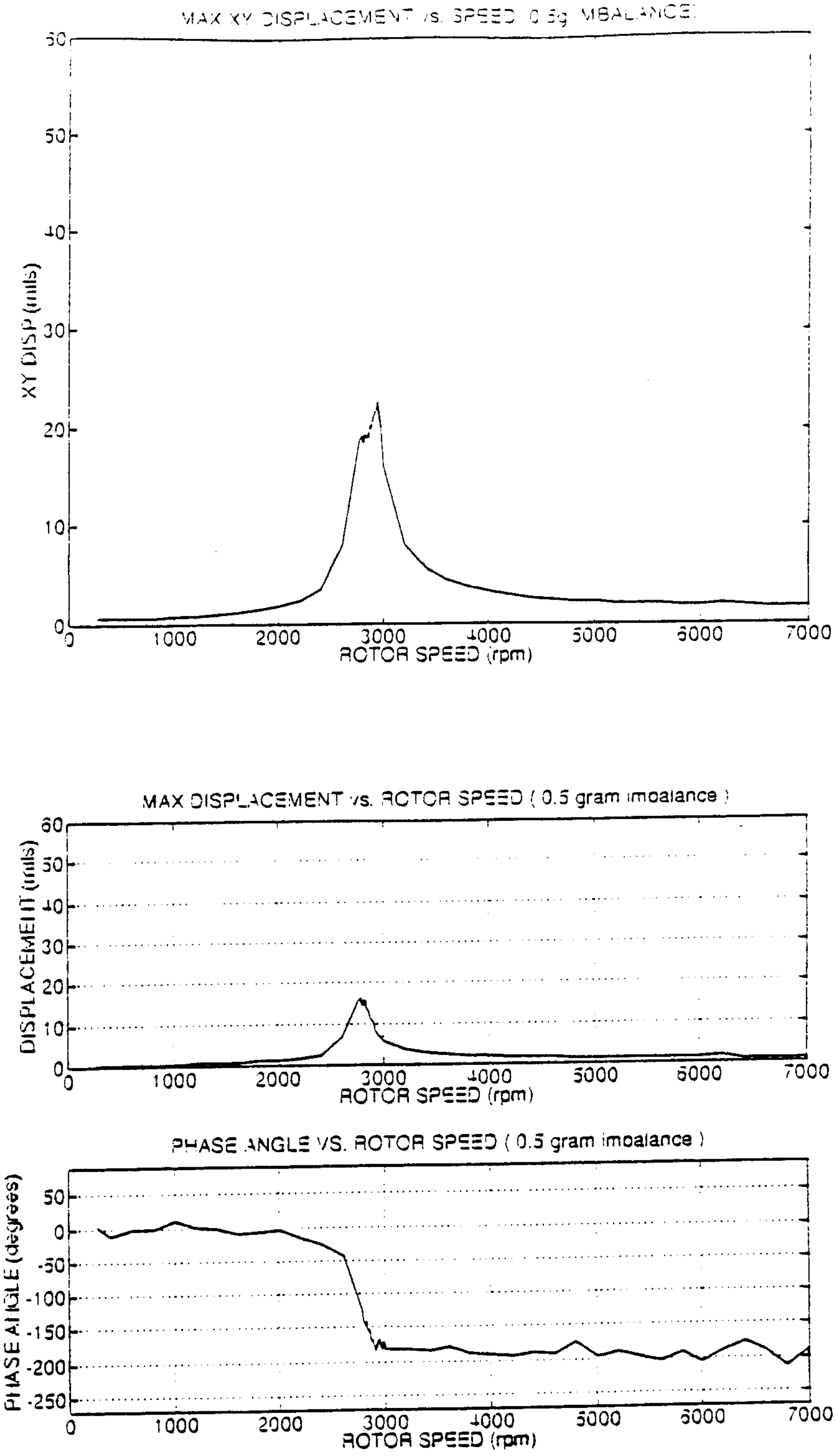

Figure 34. Maximum Displacements and Bode Plot 0.5 Gram Imbalance Good Bearing

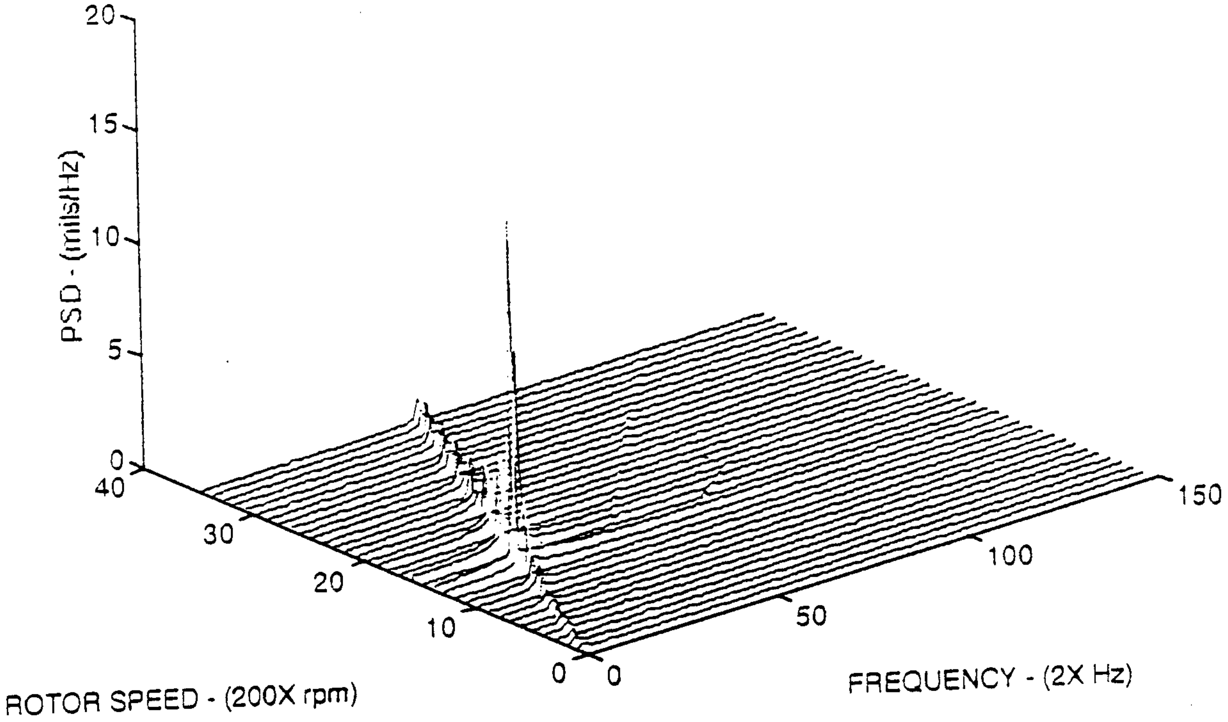

Figure 35. Cascade Plot 0.5 Gram Imbalance Good Bearing.

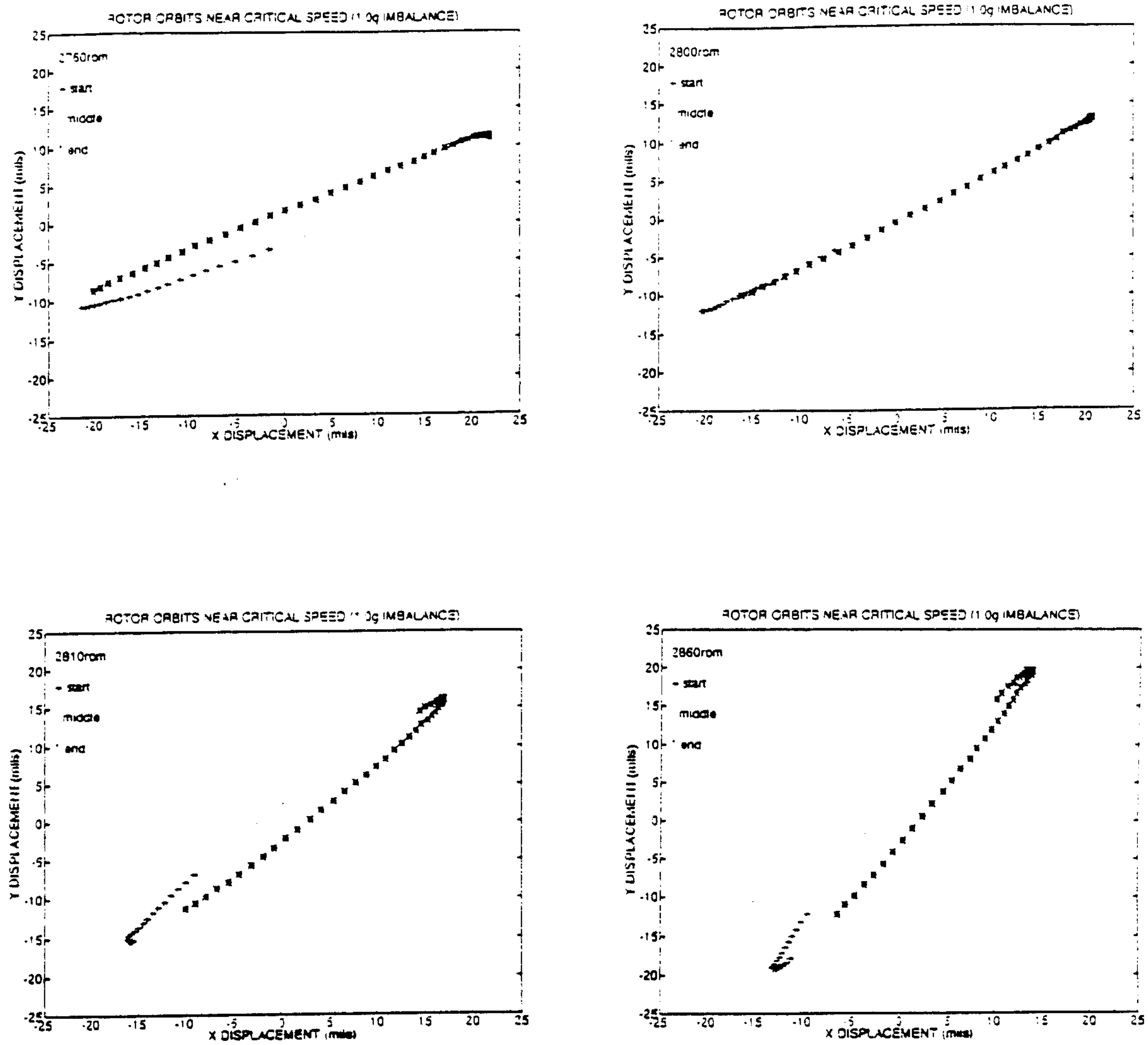

Figure 36. Rotor Orbits 1.0 Gram Imbalance Good Bearing. Speeds from 2760 to 2860 rpm.

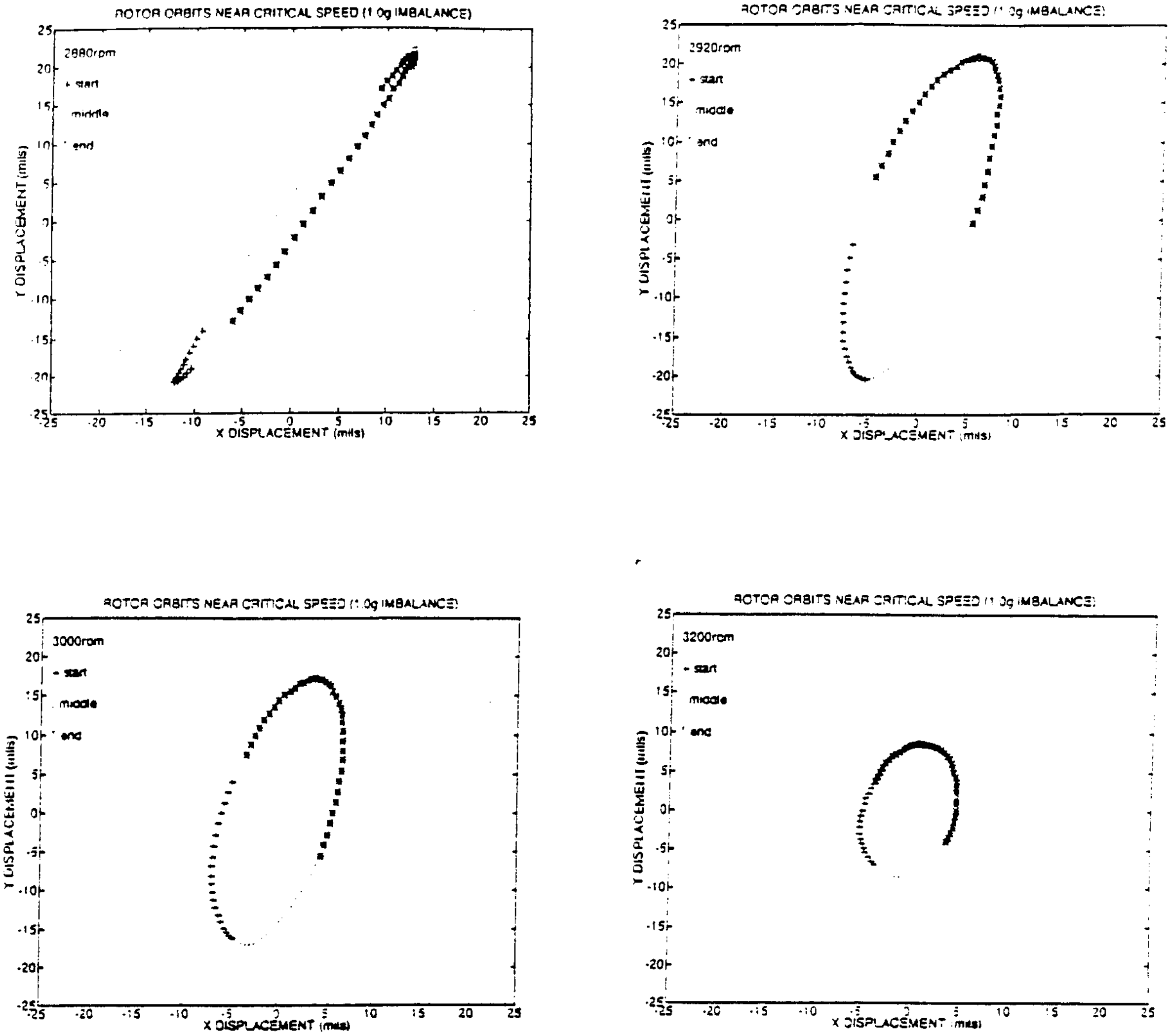

Figure 37. Rotor Orbits 1.0 Gram Imbalance Good Bearing. Speeds from 2880 to 3200 rpm.

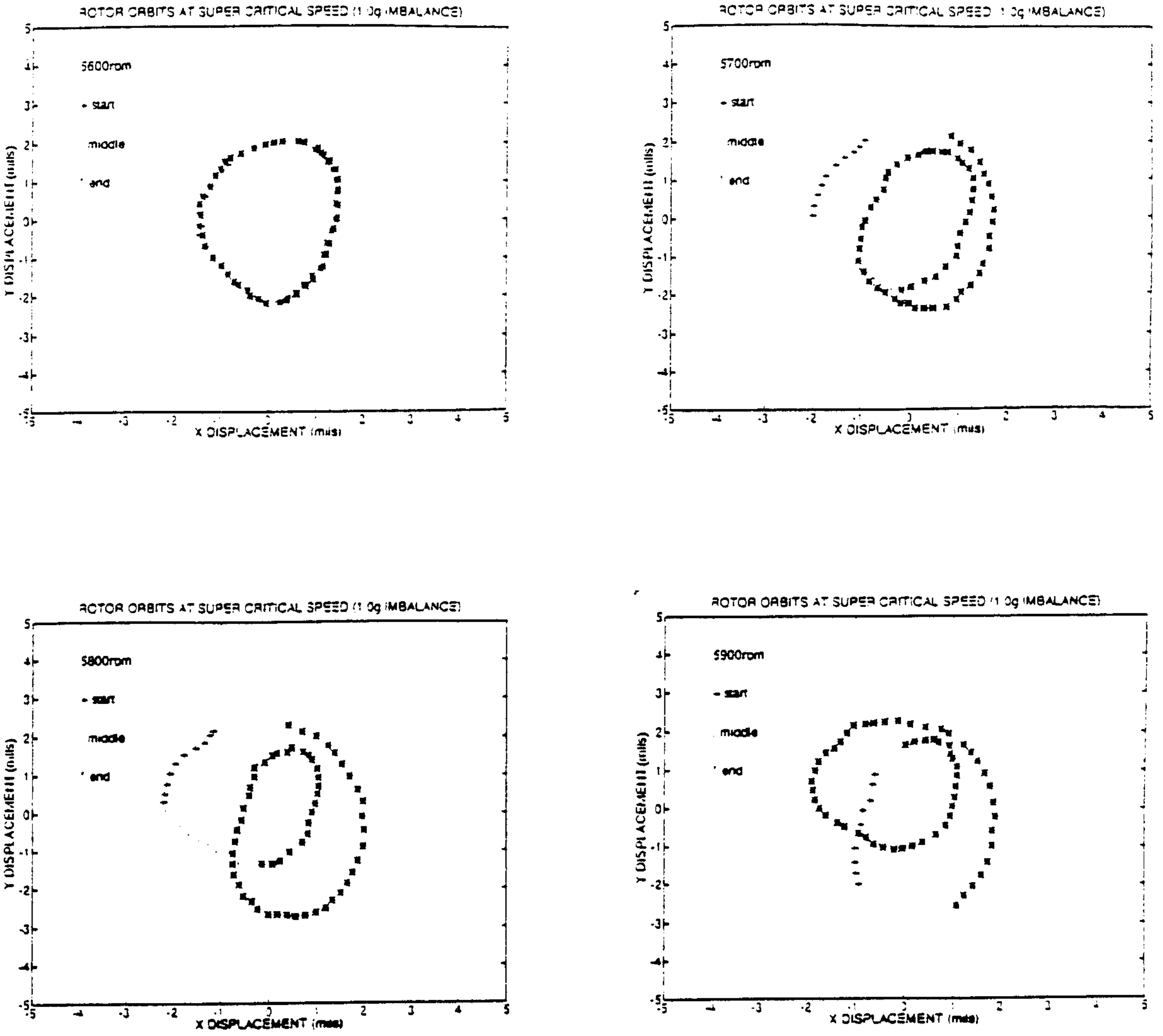

Figure 38. Rotor Orbits 1.0 Gram Imbalance Good Bearing. Speeds from 5600 to 5900 rpm.

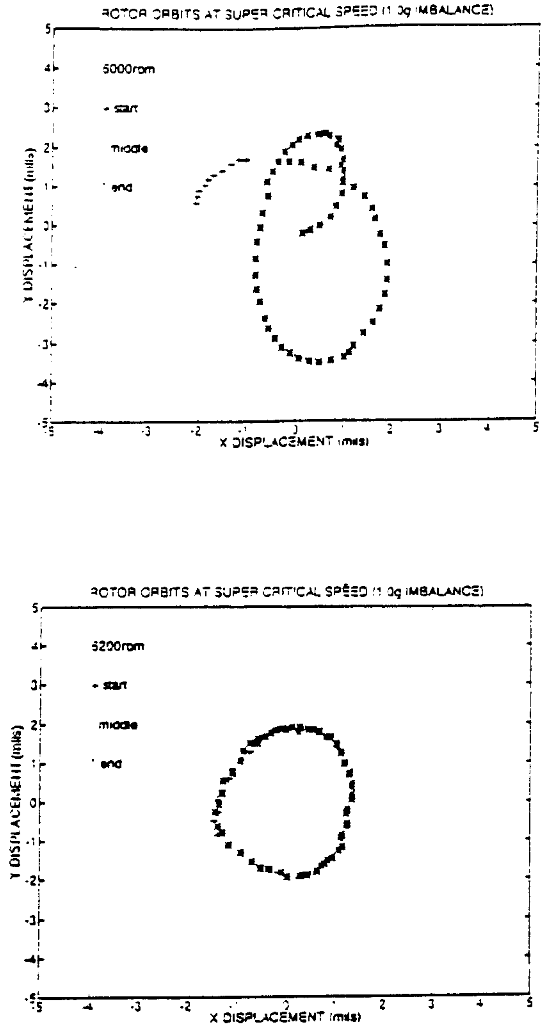

Figure 39. Rotor Orbits 1.0 Gram Imbalance Good Bearing. Speeds from 6000 to 6200 rpm.

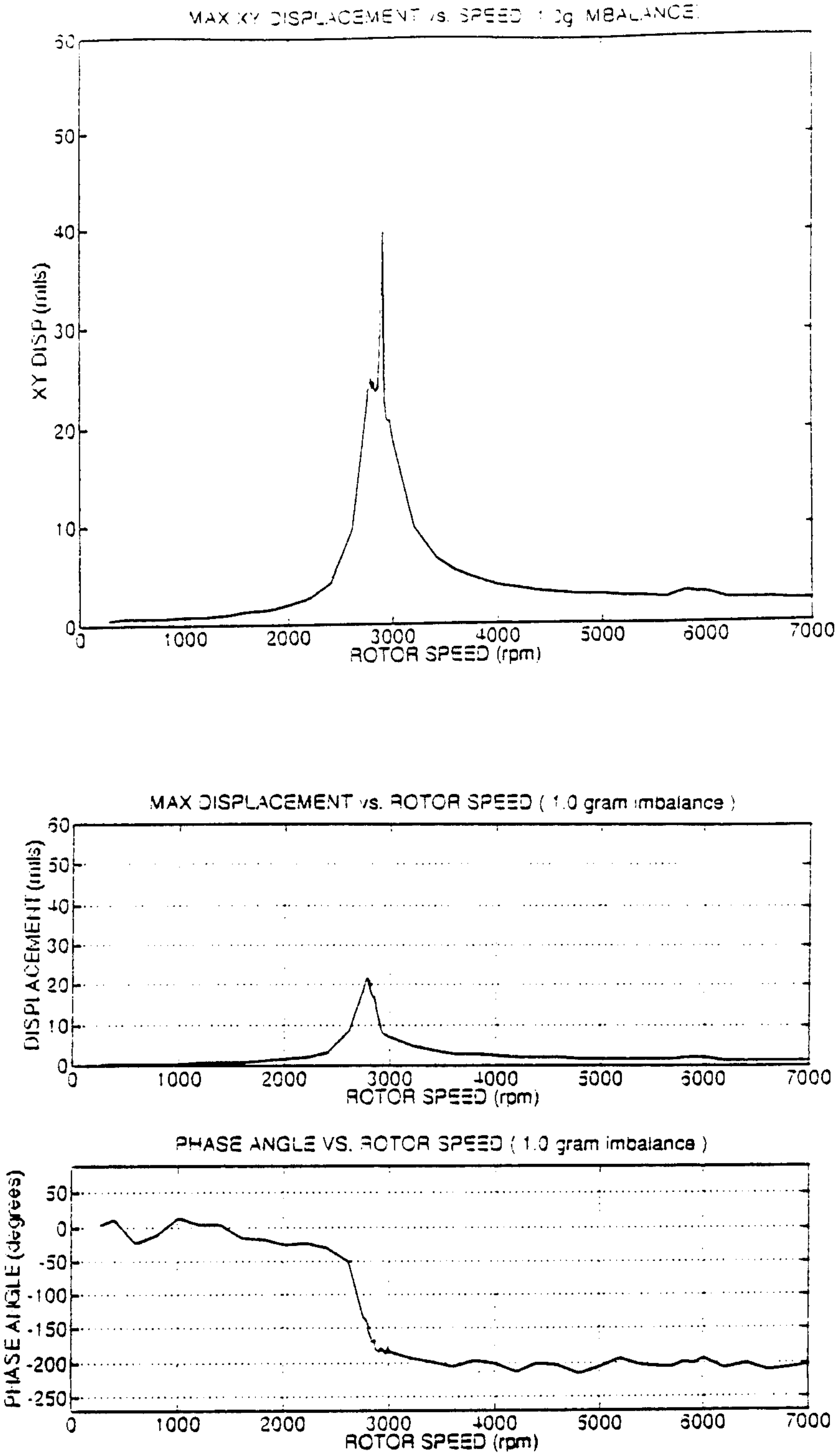

Figure 40. Maximum Displacements and Bode Plot 1.0 Gram Imbalance Good Bearing.

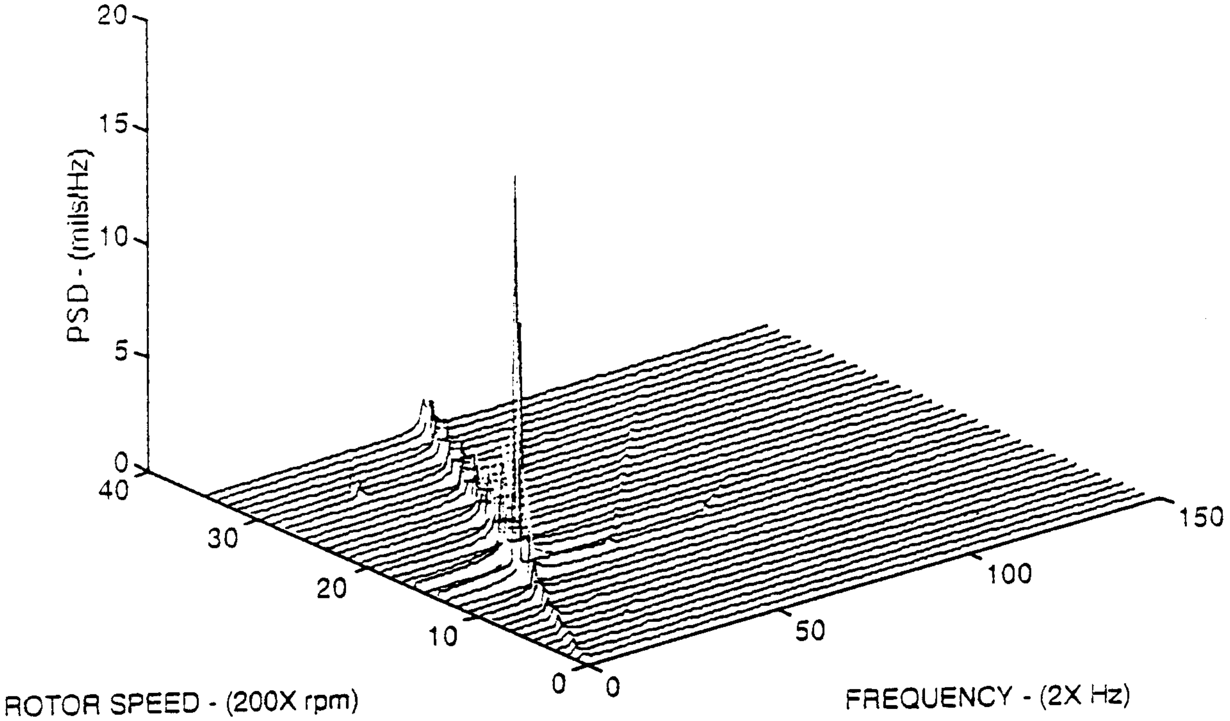

Figure 41. Cascade Plot 1.0 Gram Imbalance Good Bearing

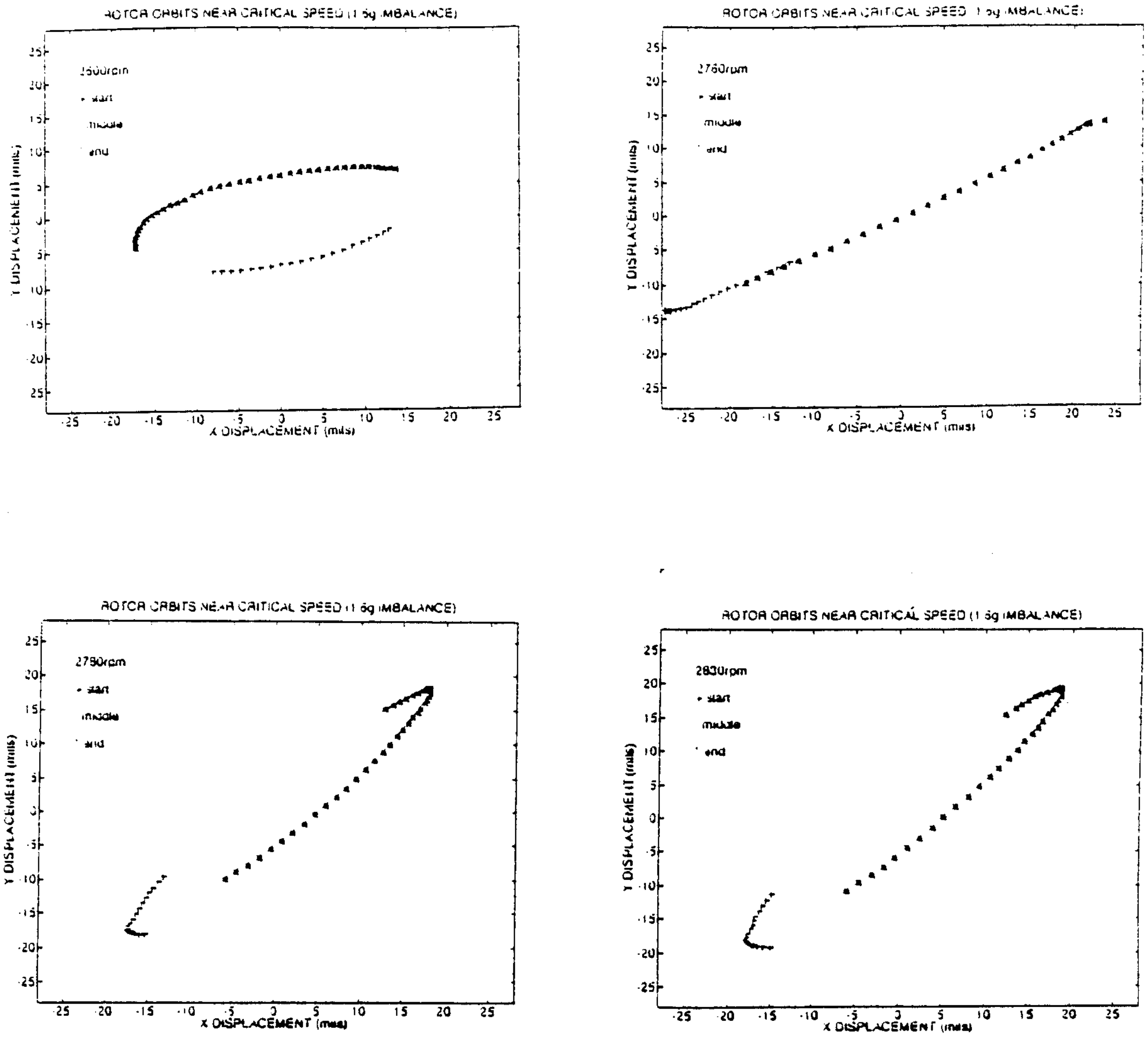

Figure 42. Rotor Orbits 1.6 Gram Imbalance Good Bearing. Speeds from 2600 to 2830 rpm.

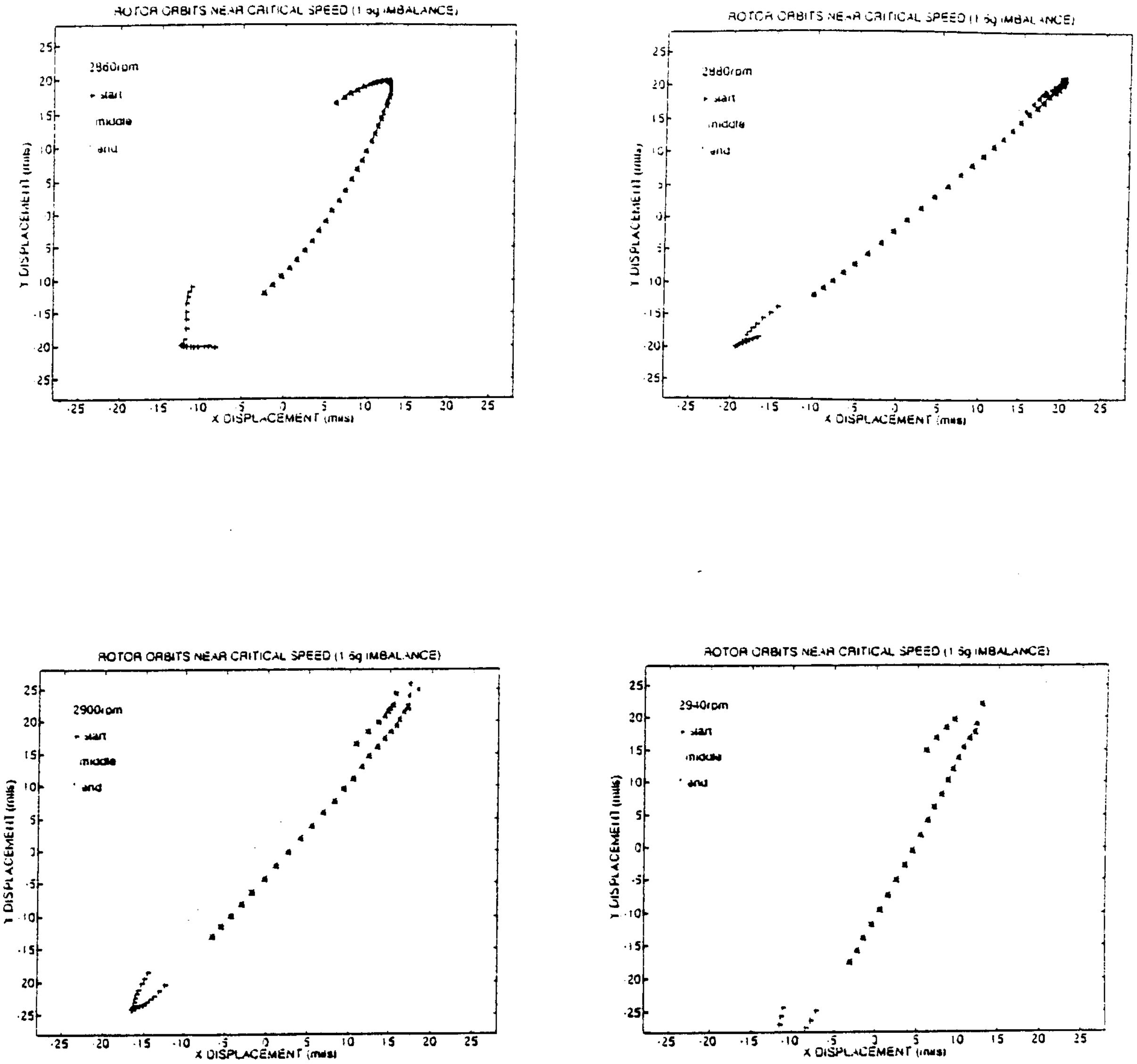

Figure 43. Rotor Orbits 1.6 Gram Imbalance Good Bearing. Speeds from 2860 to 2940 rpm.

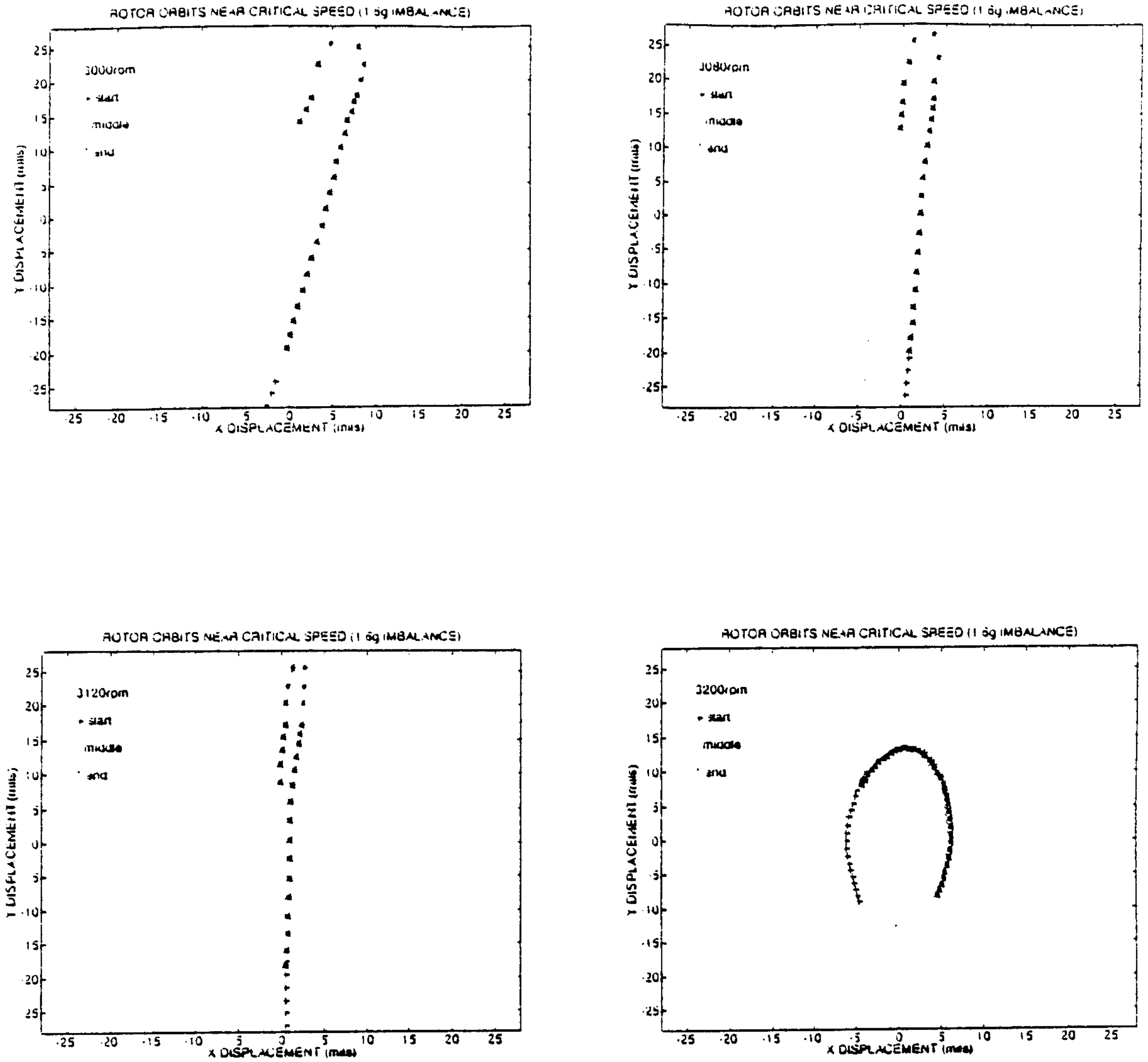

Figure 44. Rotor Orbits 1.6 Gram Imbalance Good Bearing. Speeds from 3000 to 3200 rpm.

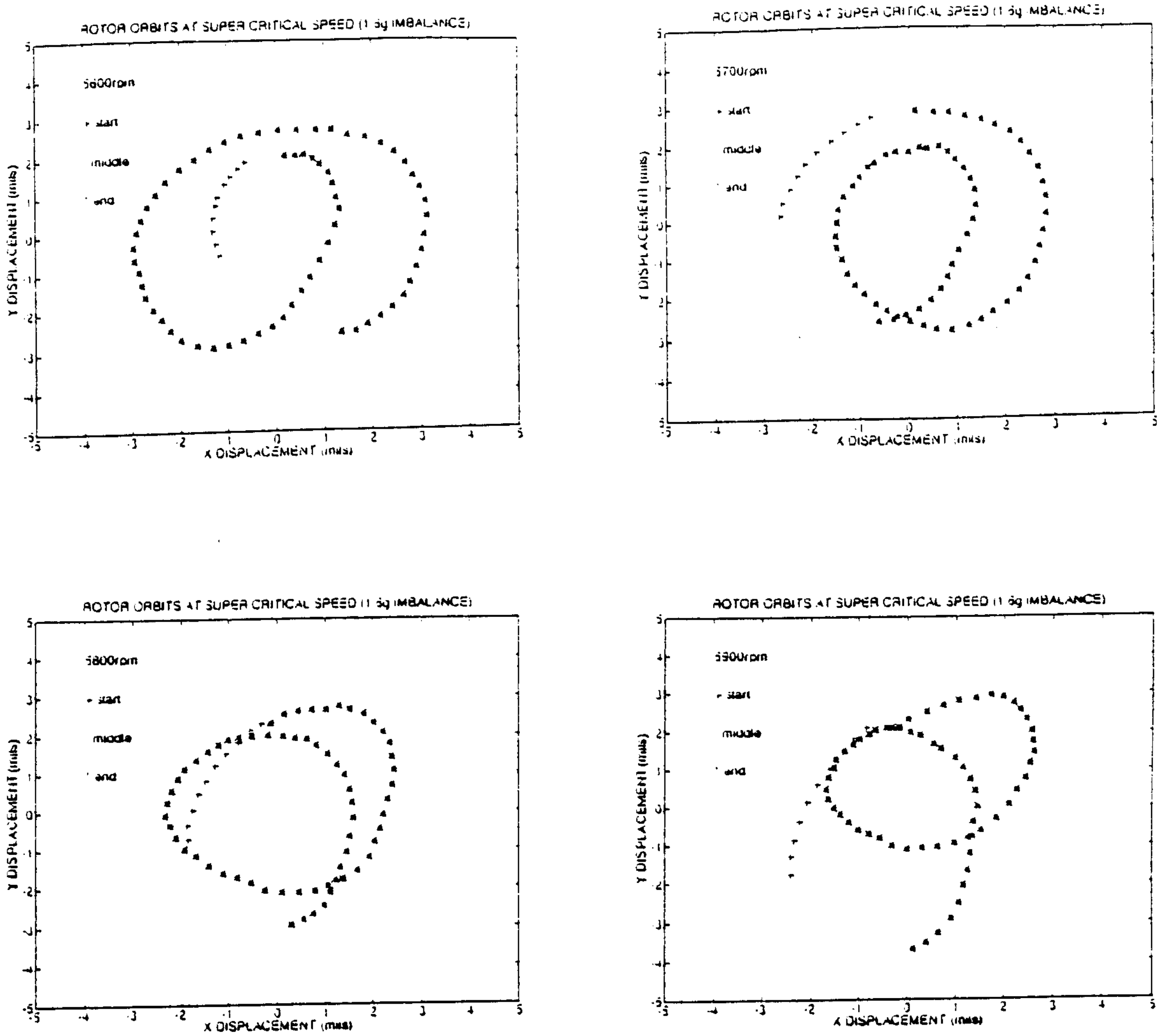

Figure 45. **Rotor Orbits 1.6 Gram Imbalance Good Bearing. Speeds from 5600 to 5900 rpm.**

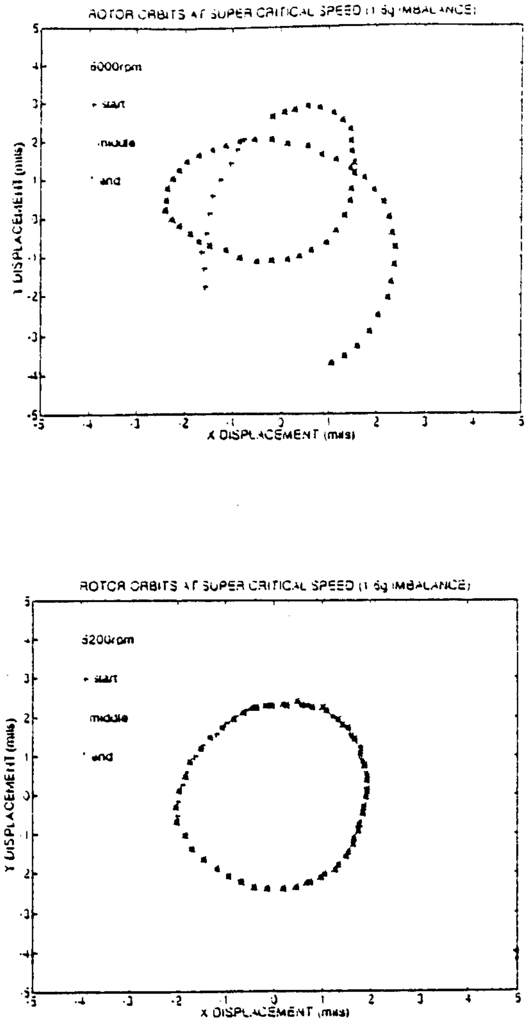

Figure 46. Rotor Orbits 1.6 Gram Imbalance Good Bearing. Speeds from 6000 to 6200 rpm.

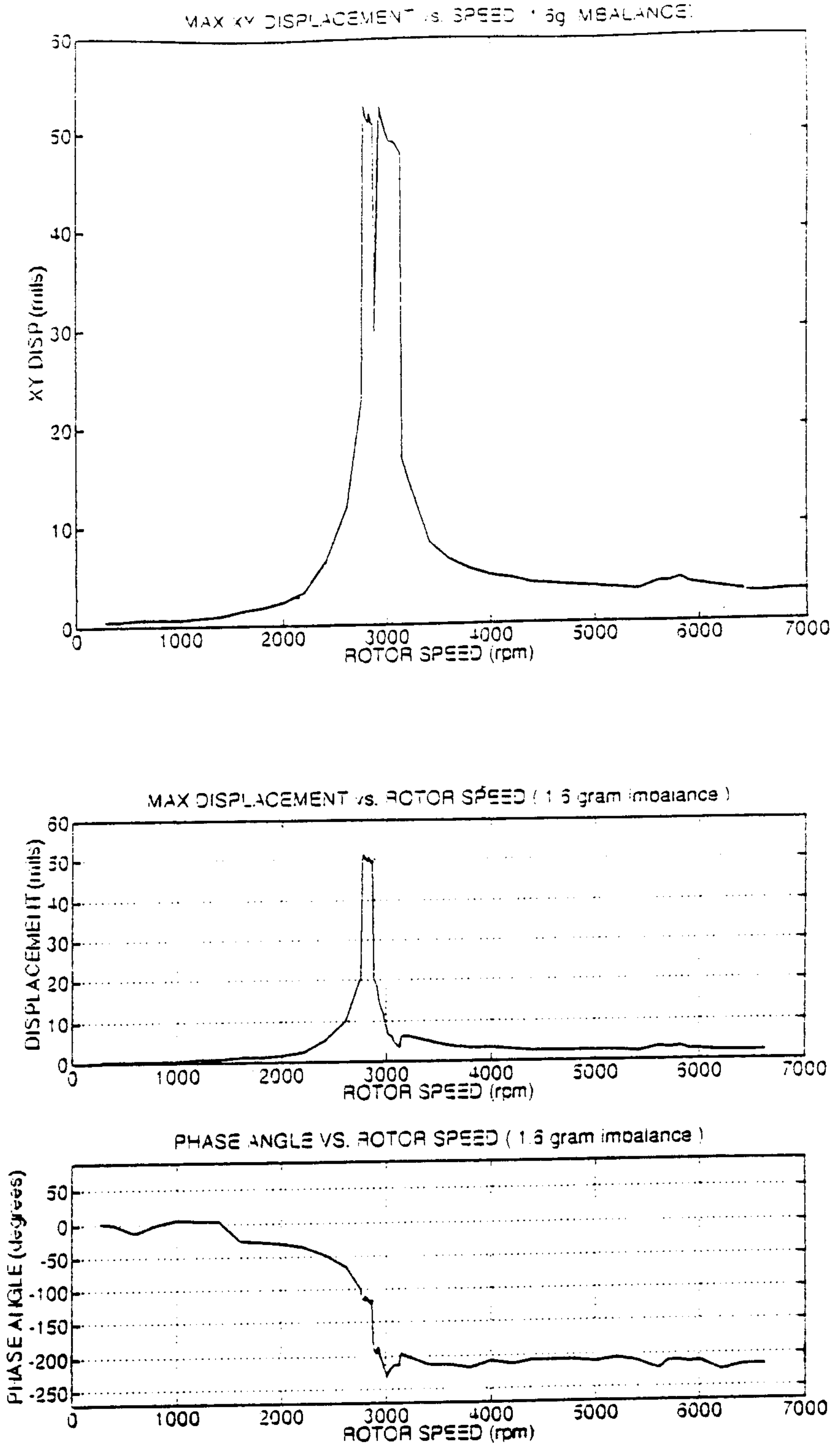

Figure 47. Maximum Displacements and Bode Plot 1.6 Gram Imbalance Good Bearing.

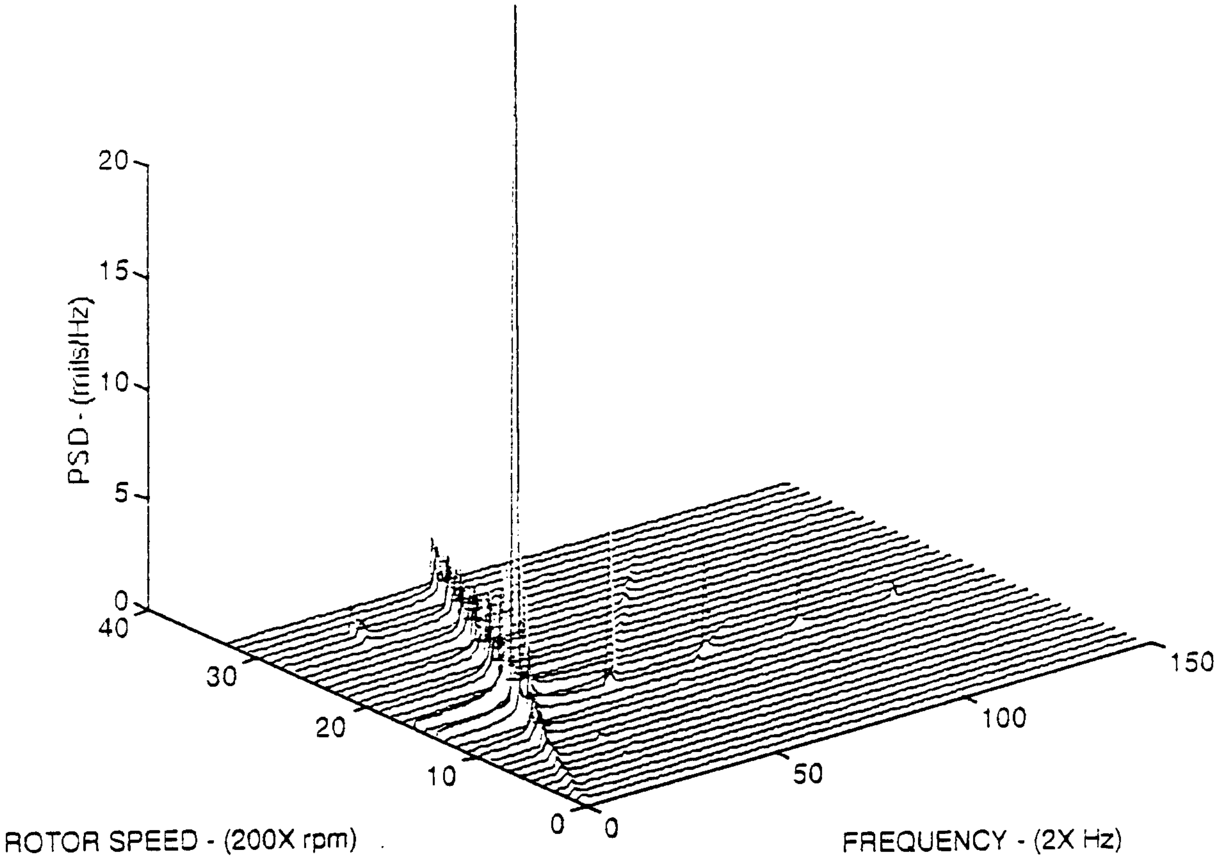

Figure 48. Cascade Plot 1.6 Gram Imbalance Good Bearing.

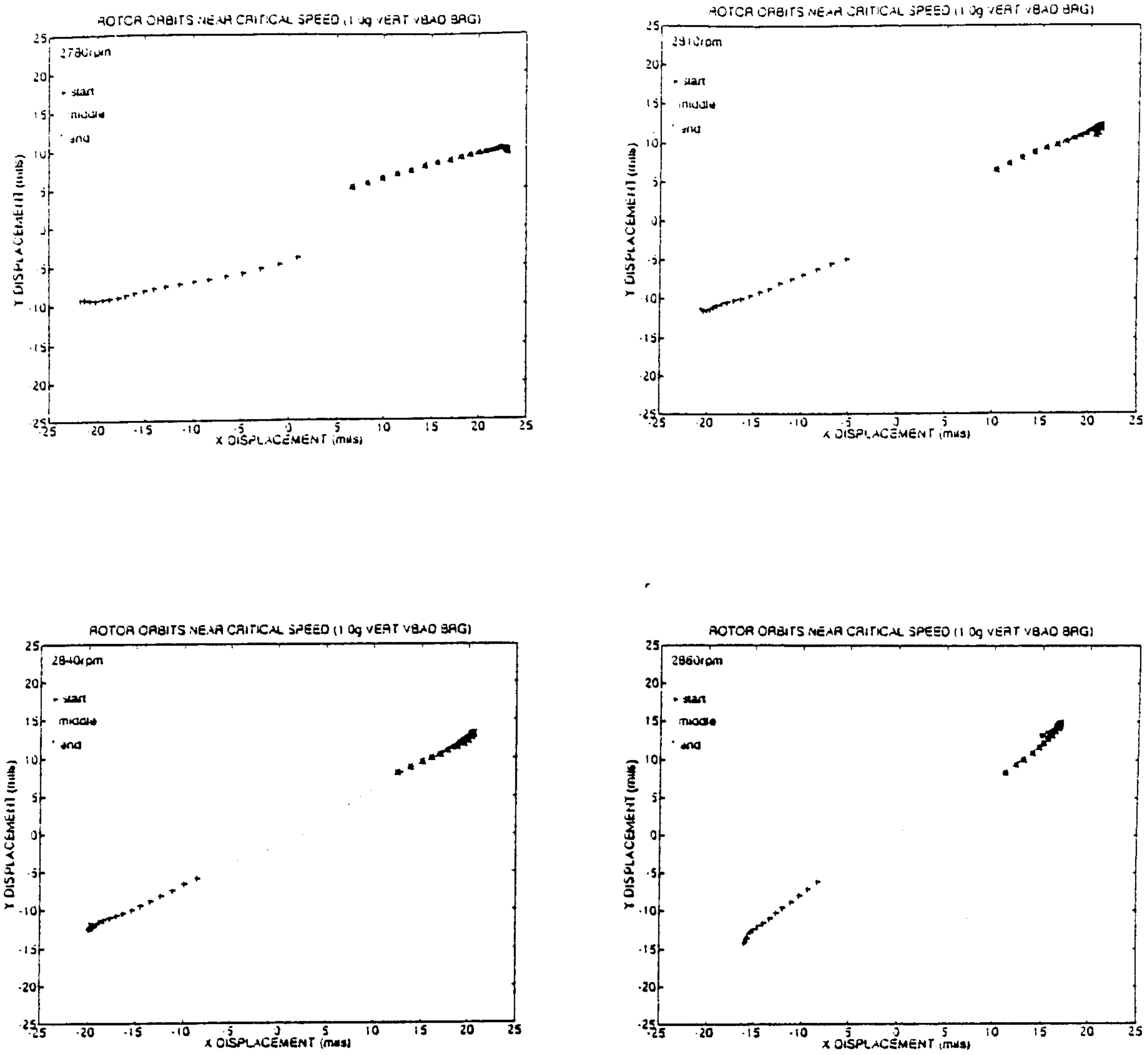

Figure 49. Rotor Orbits 1.0 Gram Imbalance Elongated Bearing with Elongation In the Vertical Direction. Speeds from 2780 to 2860 rpm.

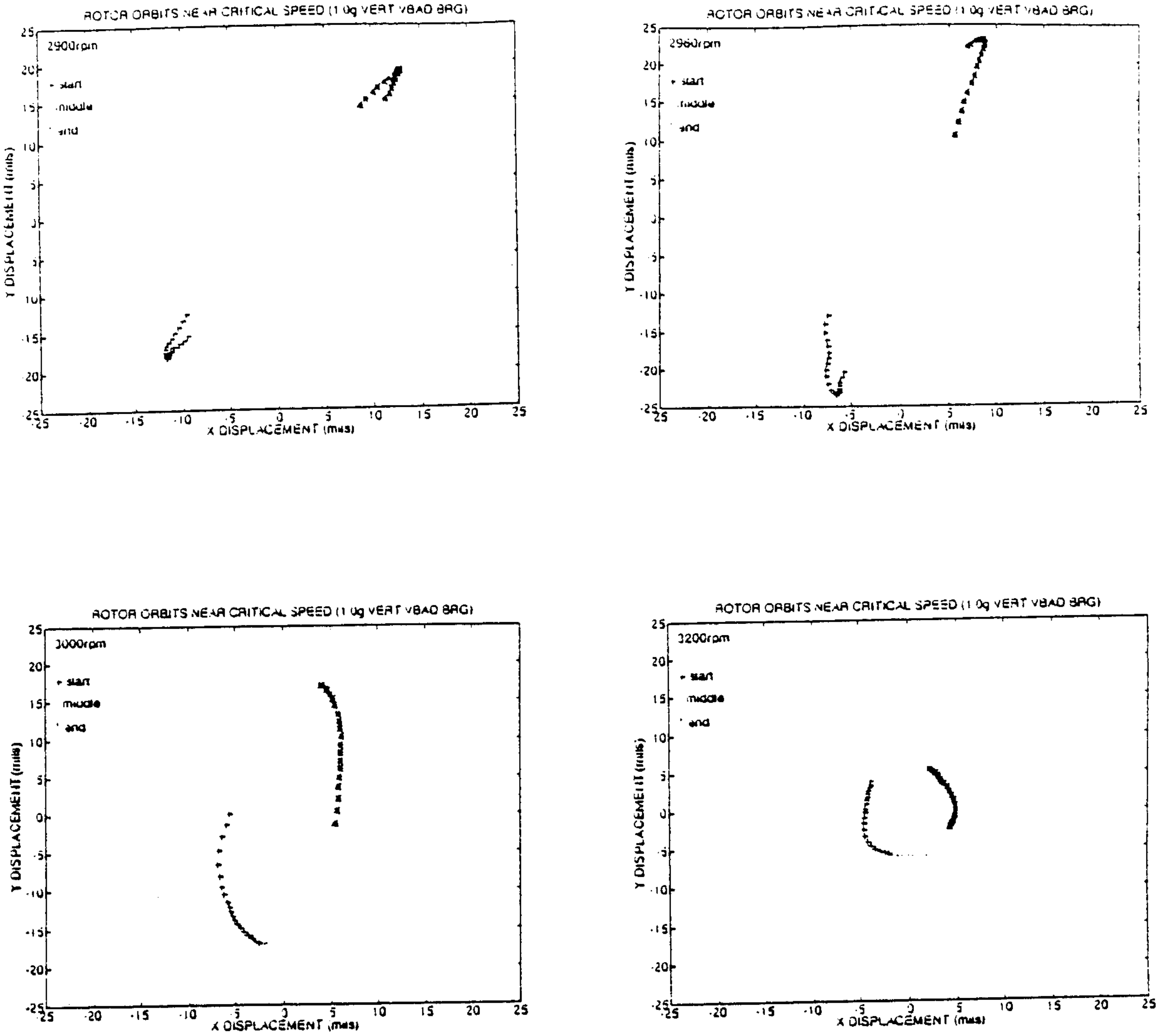

Figure 50. Rotor Orbits 1.0 Gram Imbalance Elongated Bearing with Elongation In the Vertical Direction. Speeds from 2900 to 3200 rpm.

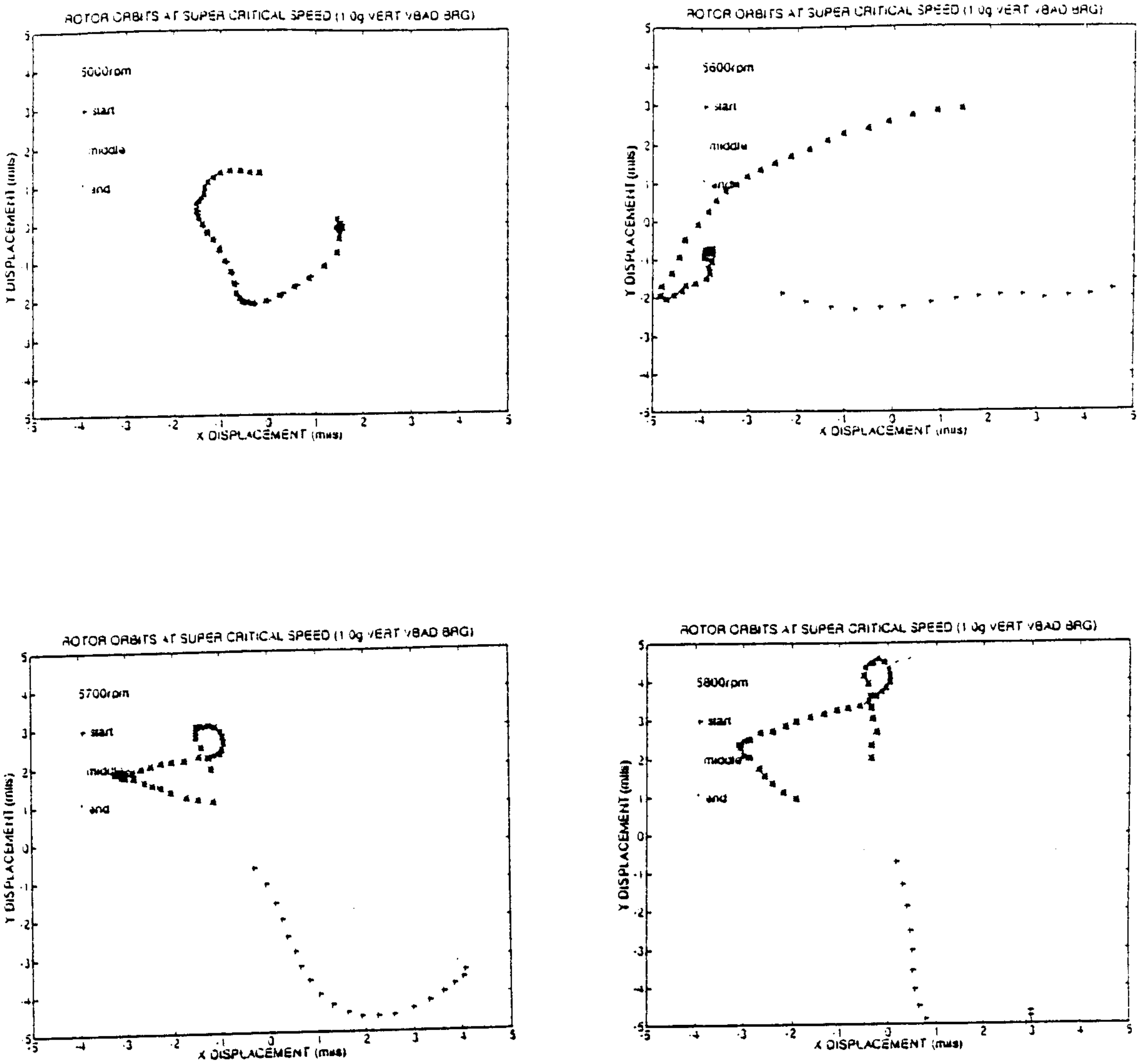

Figure 51. Rotor Orbits 1.0 Gram Imbalance Elongated Bearing with Elongation In the Vertical Direction. Speeds from 5000 to 5800 rpm.

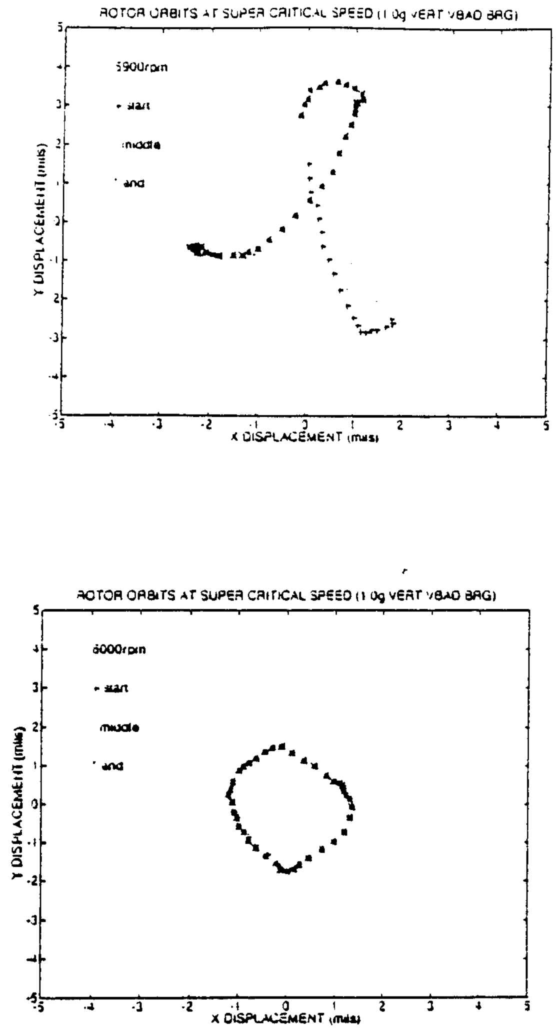

Figure 52. Rotor Orbits 1.0 Gram Imbalance Elongated Bearing with Elongation In the Vertical Direction. Speeds from 5900 to 6000 rpm.

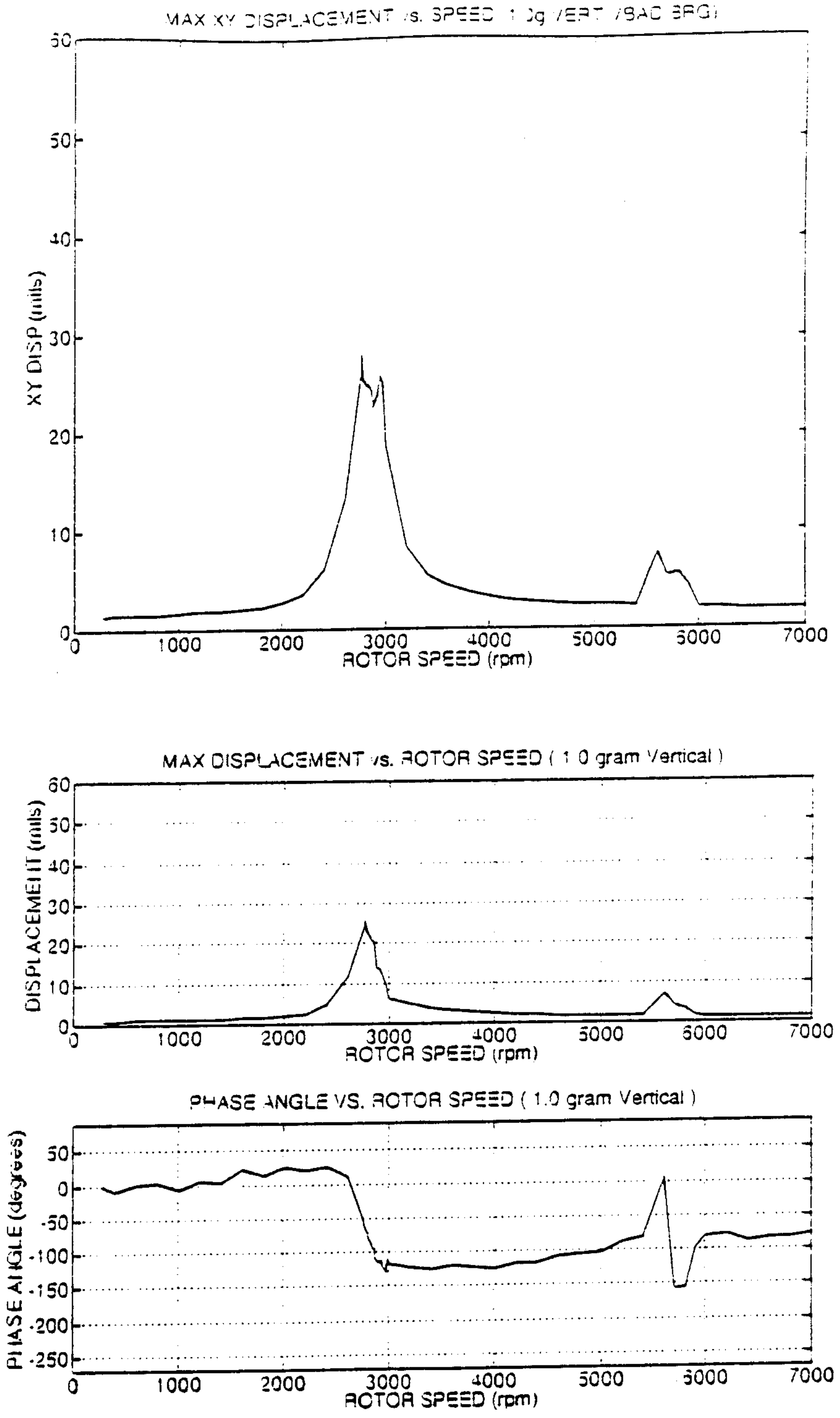

Figure 53. Maximum Displacements and Bode Plot 1.0 Gram Imbalance Elongated Bearing with Elongation In the Vertical Direction.

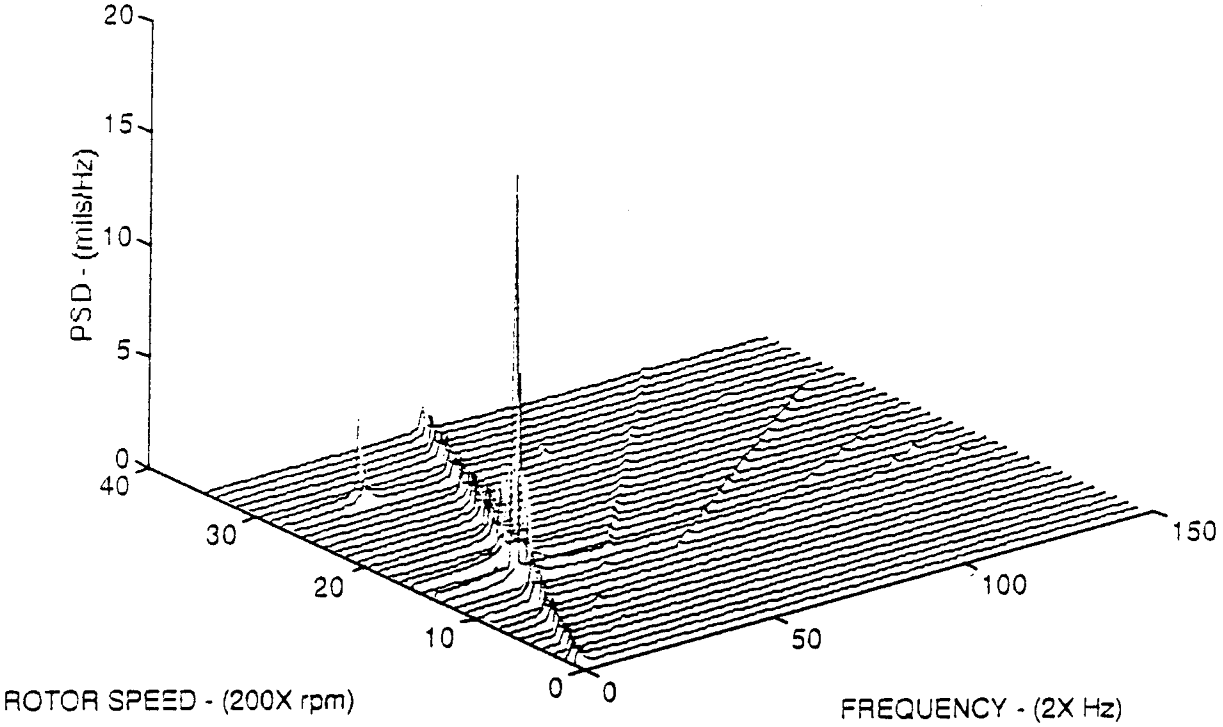

Figure 54. Cascade Plot 1.0 Gram Imbalance Elongated Bearing with Elongation In the Vertical Direction.

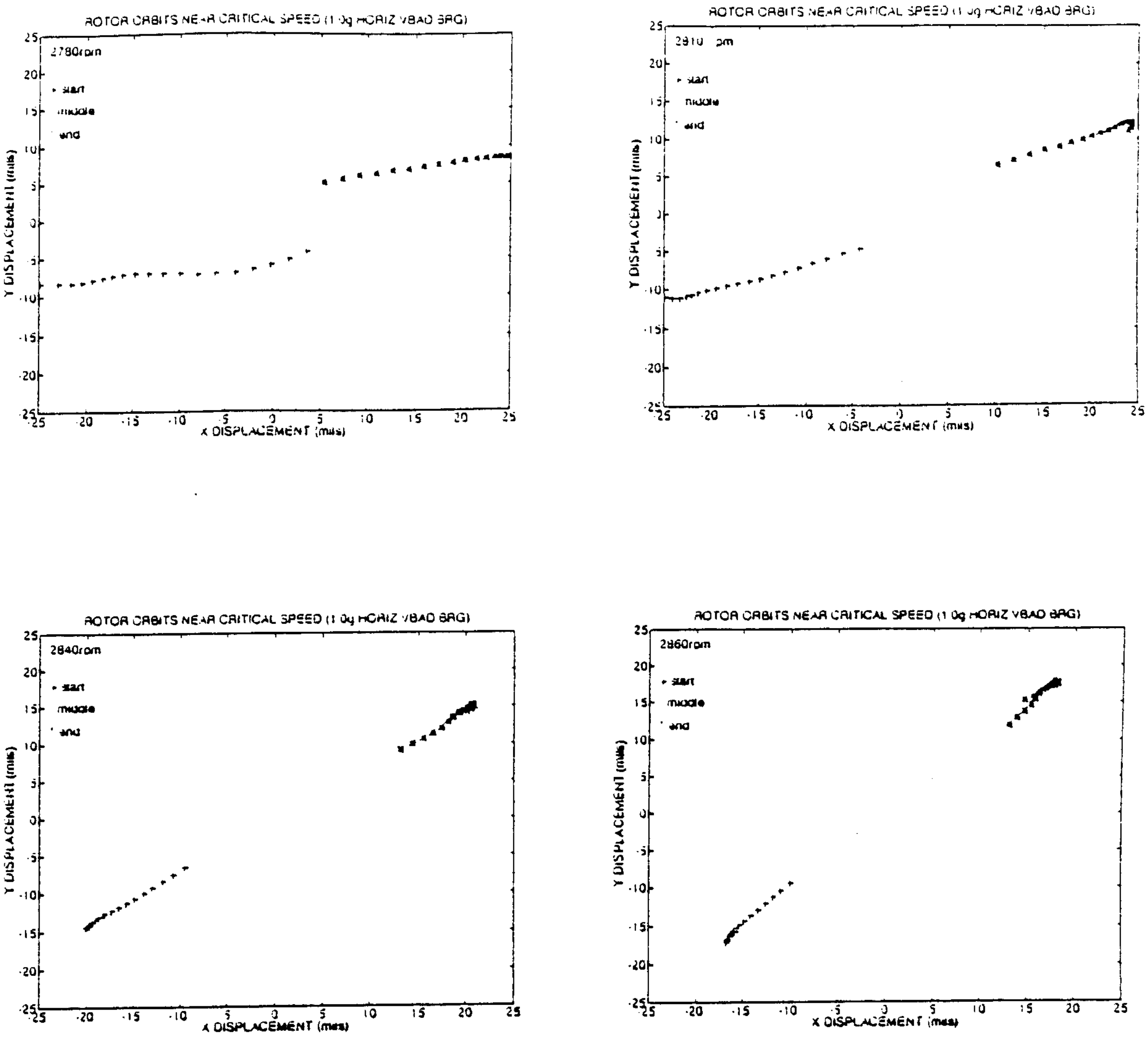

Figure 55. Rotor Orbits 1.0 Gram Imbalance Elongated Bearing with Elongation In the Horizontal Direction. Speeds from 2780 to 2860 rpm.

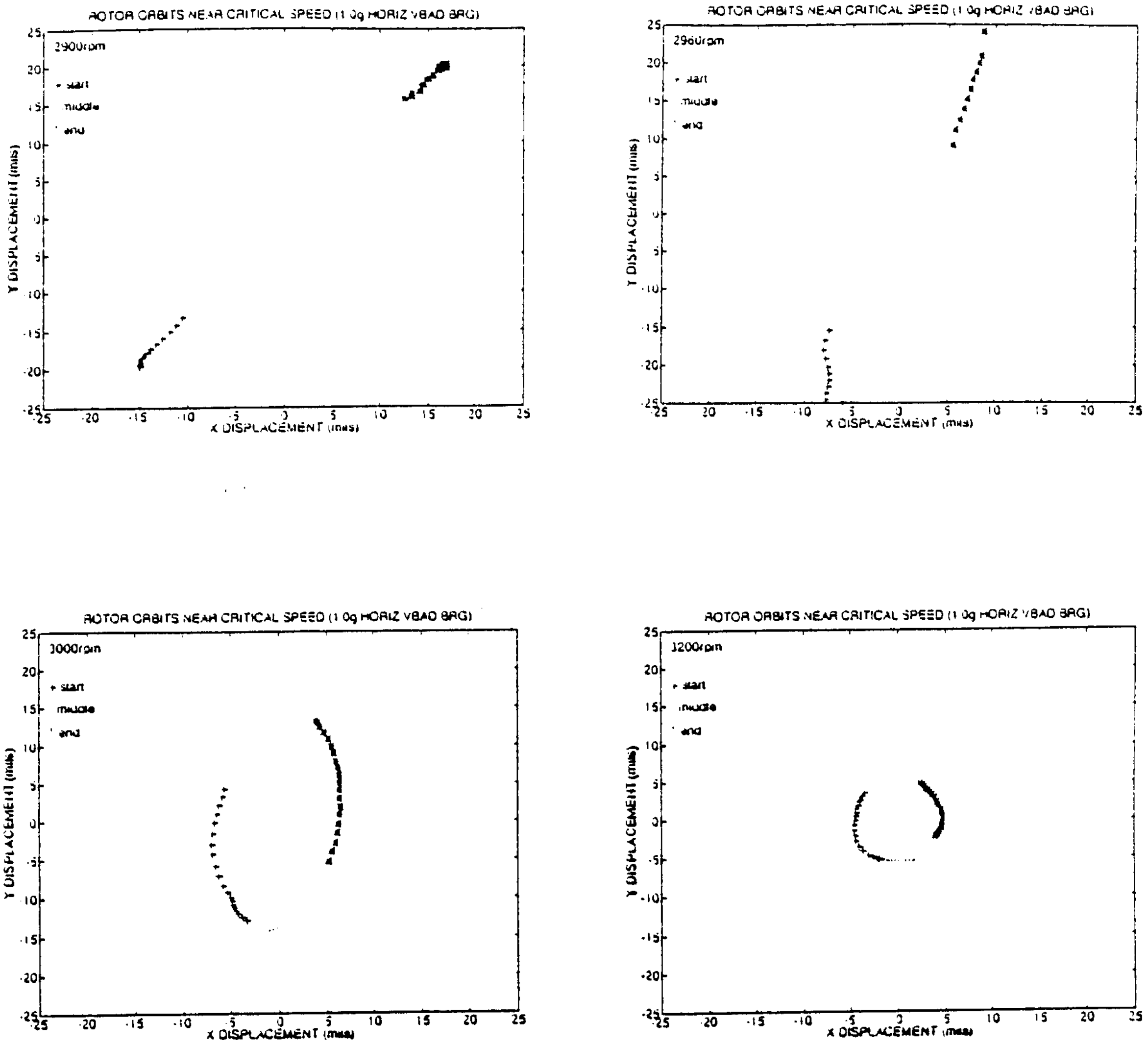

Figure 56. Rotor Orbits 1.0 Gram Imbalance Elongated Bearing with Elongation In the Horizontal Direction. Speeds from 2900 to 3200 rpm.

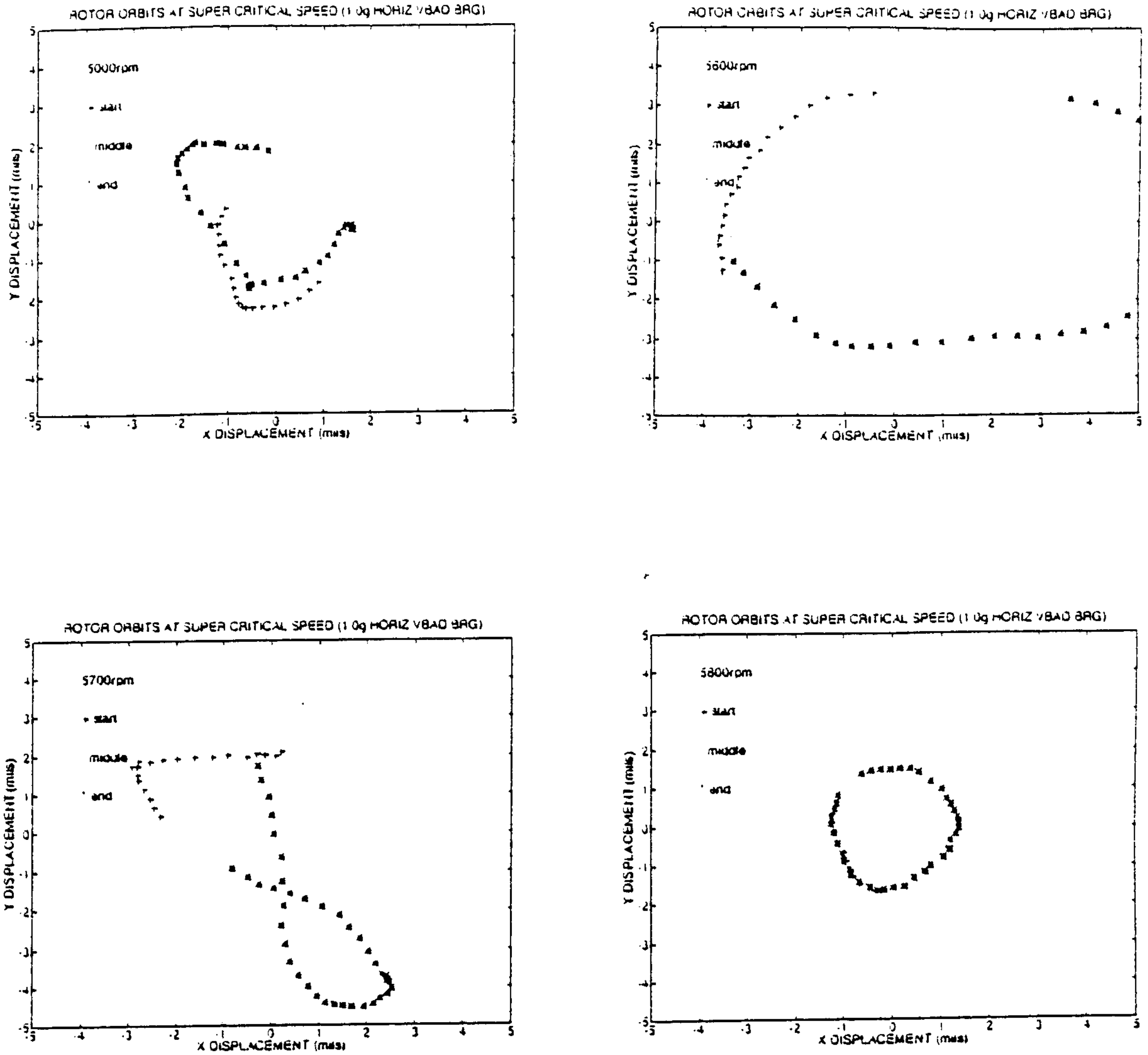

Figure 57. Rotor Orbits 1.0 Gram Imbalance Elongated Bearing with Elongation In the Horizontal Direction. Speeds from 5000 to 5800 rpm.

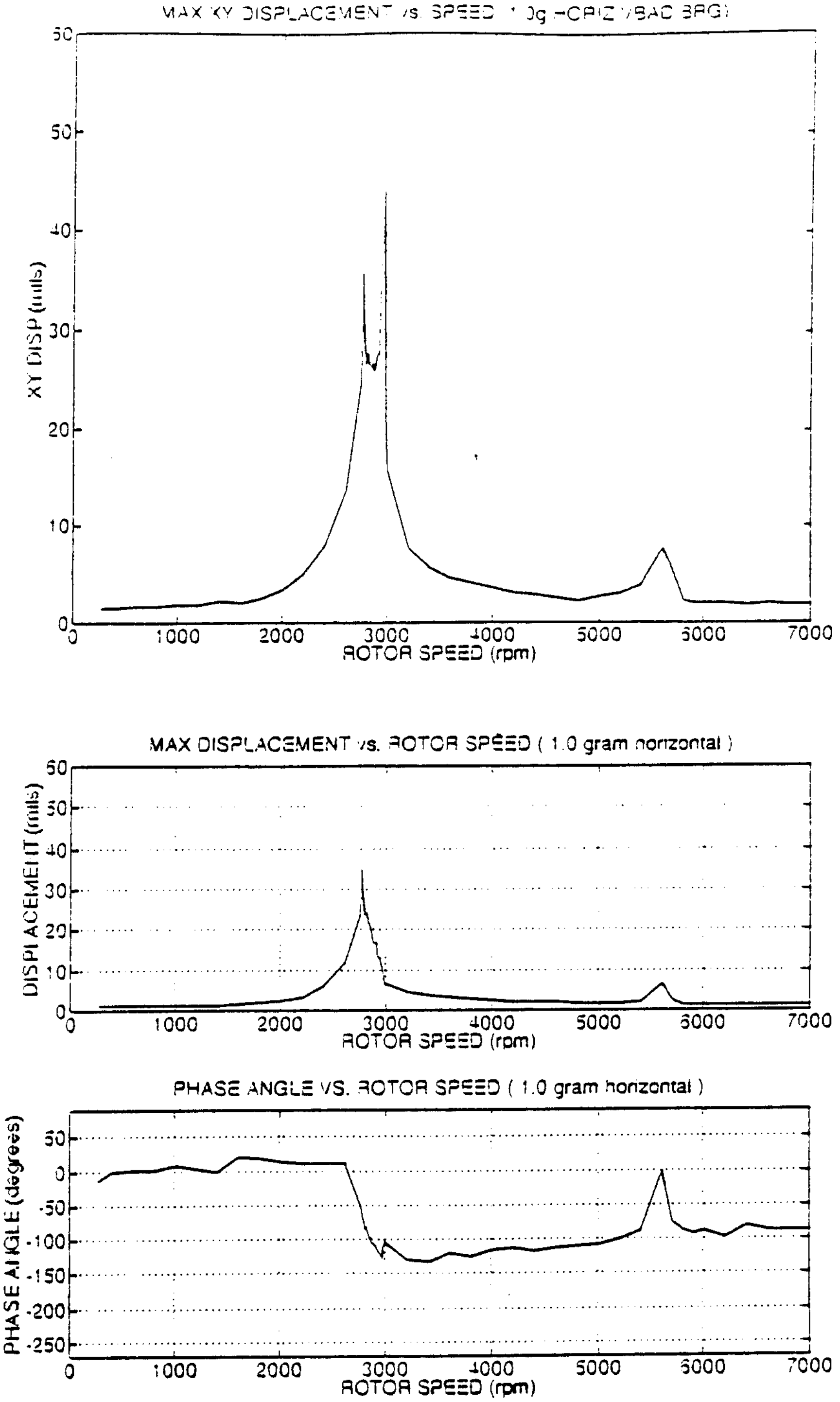

Figure 58. Maximum Displacements and Bode Plot 1.0 Gram Imbalance Elongated Bearing with Elongation In the Horizontal Direction.

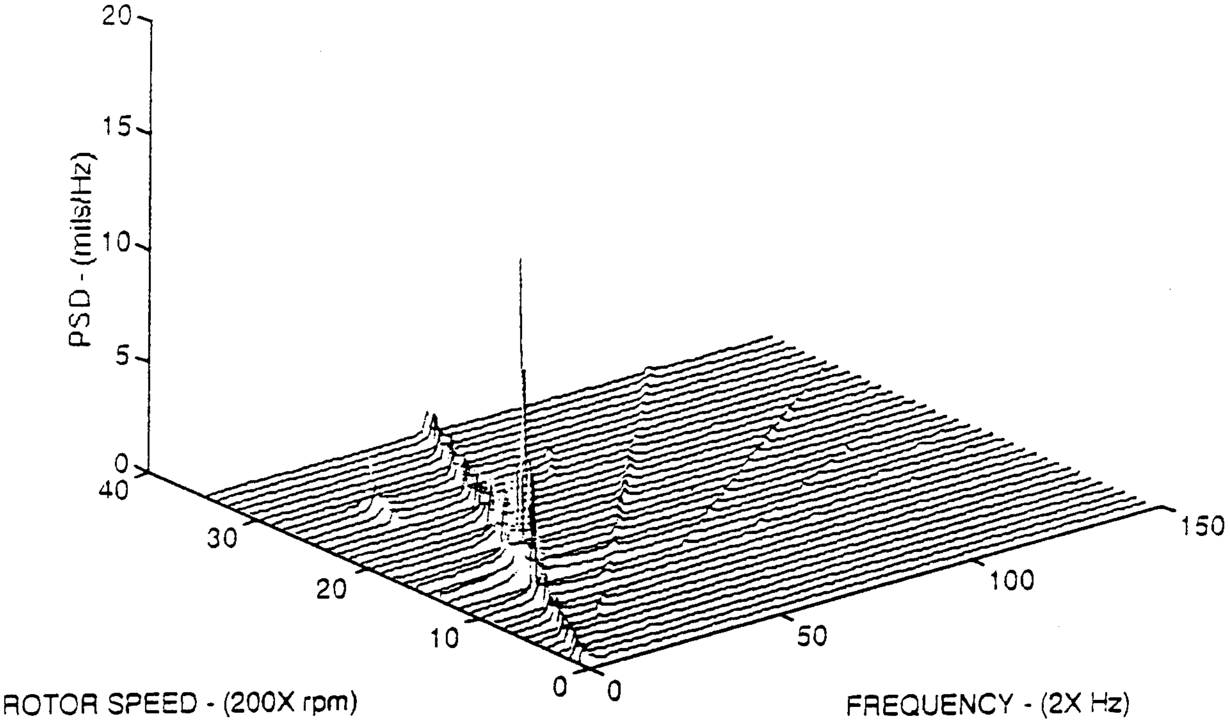

Figure 59. Cascade Plot 1.0 Gram Imbalance Elongated Bearing with Elongation In the Horizontal Direction.

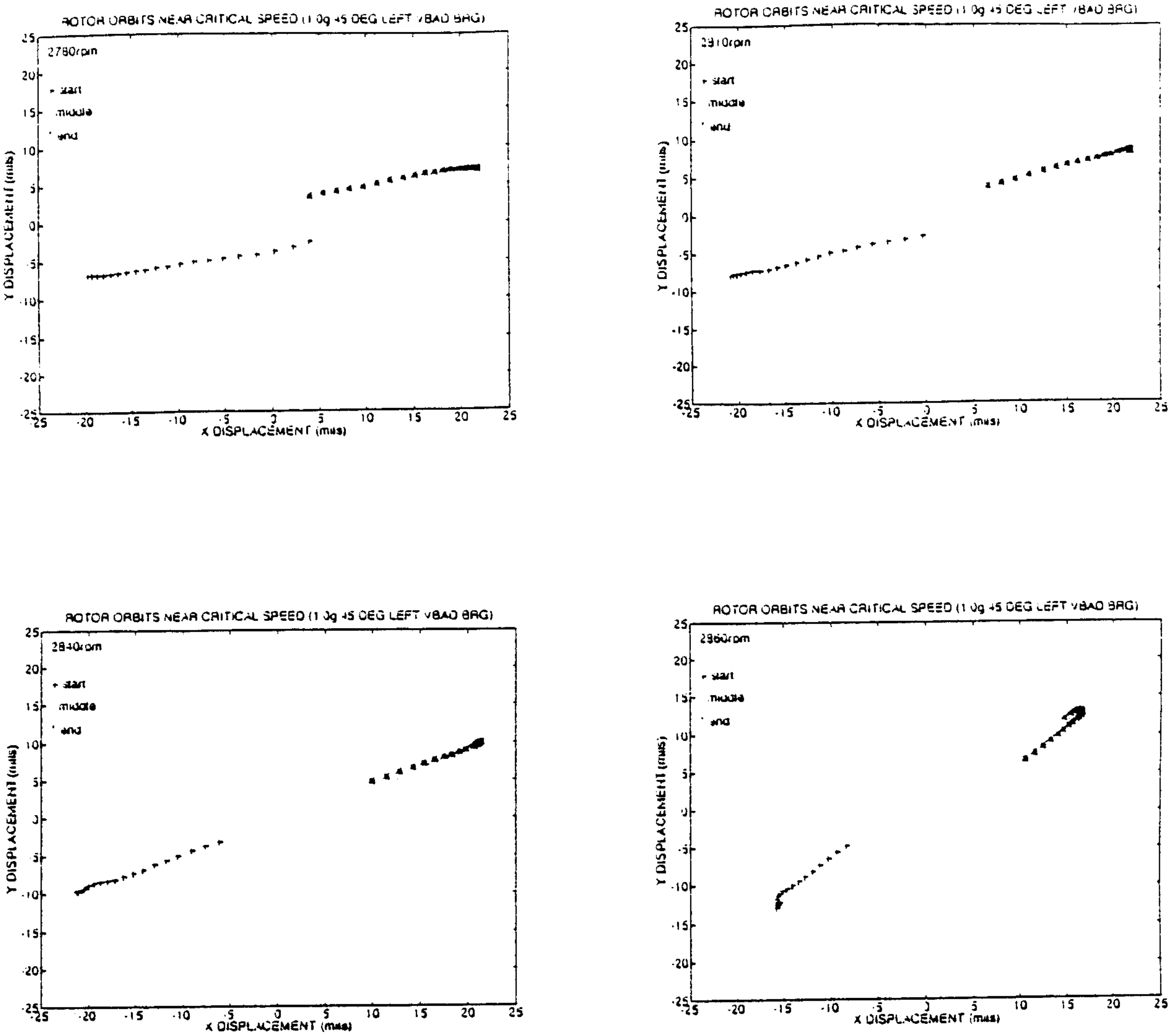

Figure 60. Rotor Orbits 1.0 Gram Imbalance Elongated Bearing with Elongation In the Direction of the Resonant Displacement (45 Degrees off vertical). Speeds from 2780 to 2860 rpm.

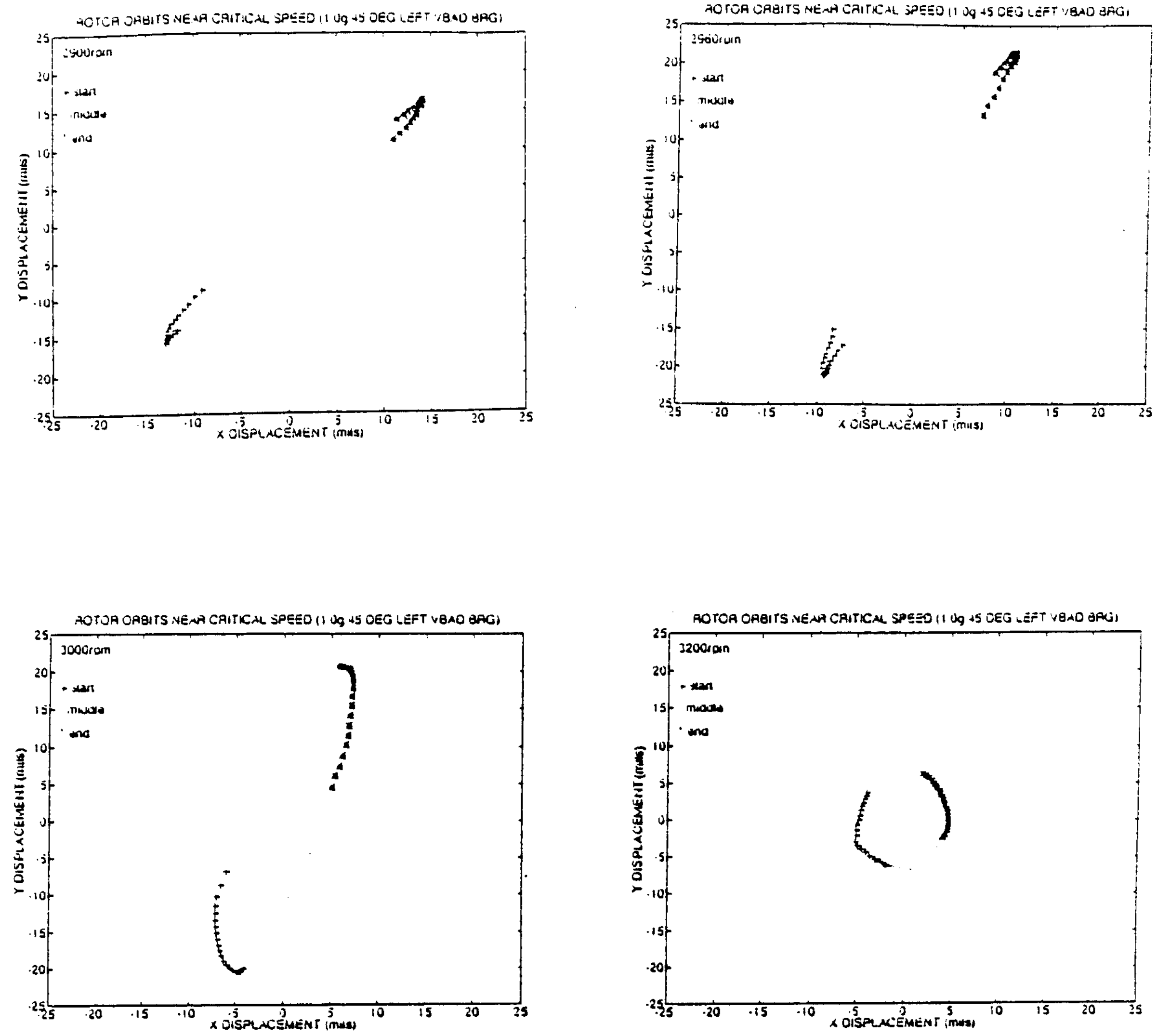

Figure 61. Rotor Orbits 1.0 Gram Imbalance Elongated Bearing with Elongation In the Direction of the Resonant Displacement (45 Degrees off vertical). Speeds from 2900 to 3200 rpm.

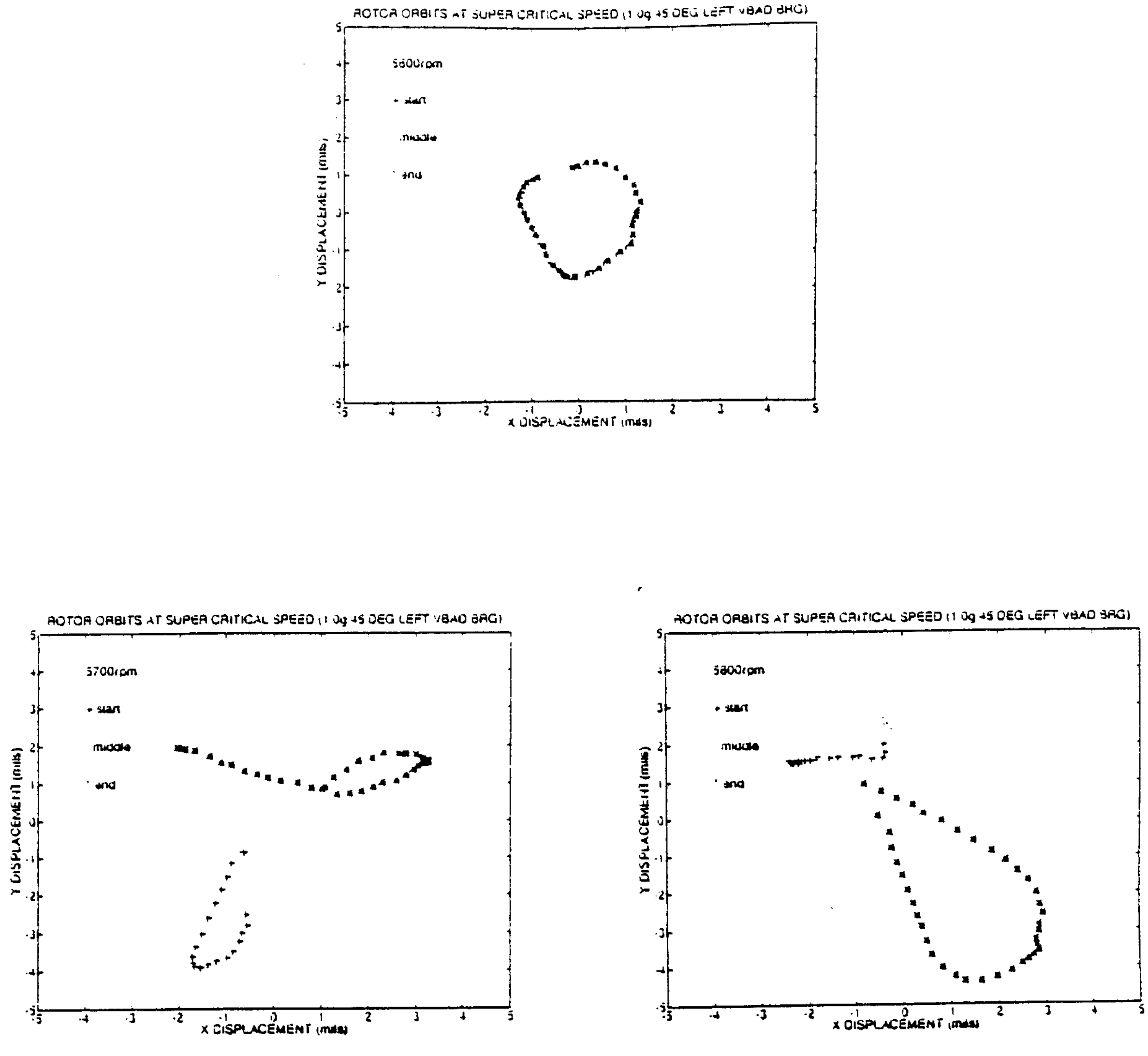

Figure 62. Rotor Orbits 1.0 Gram Imbalance Elongated Bearing with Elongation In the Direction of the Resonant Displacement (45 Degrees off vertical). Speeds from 5600 to 5800 rpm.

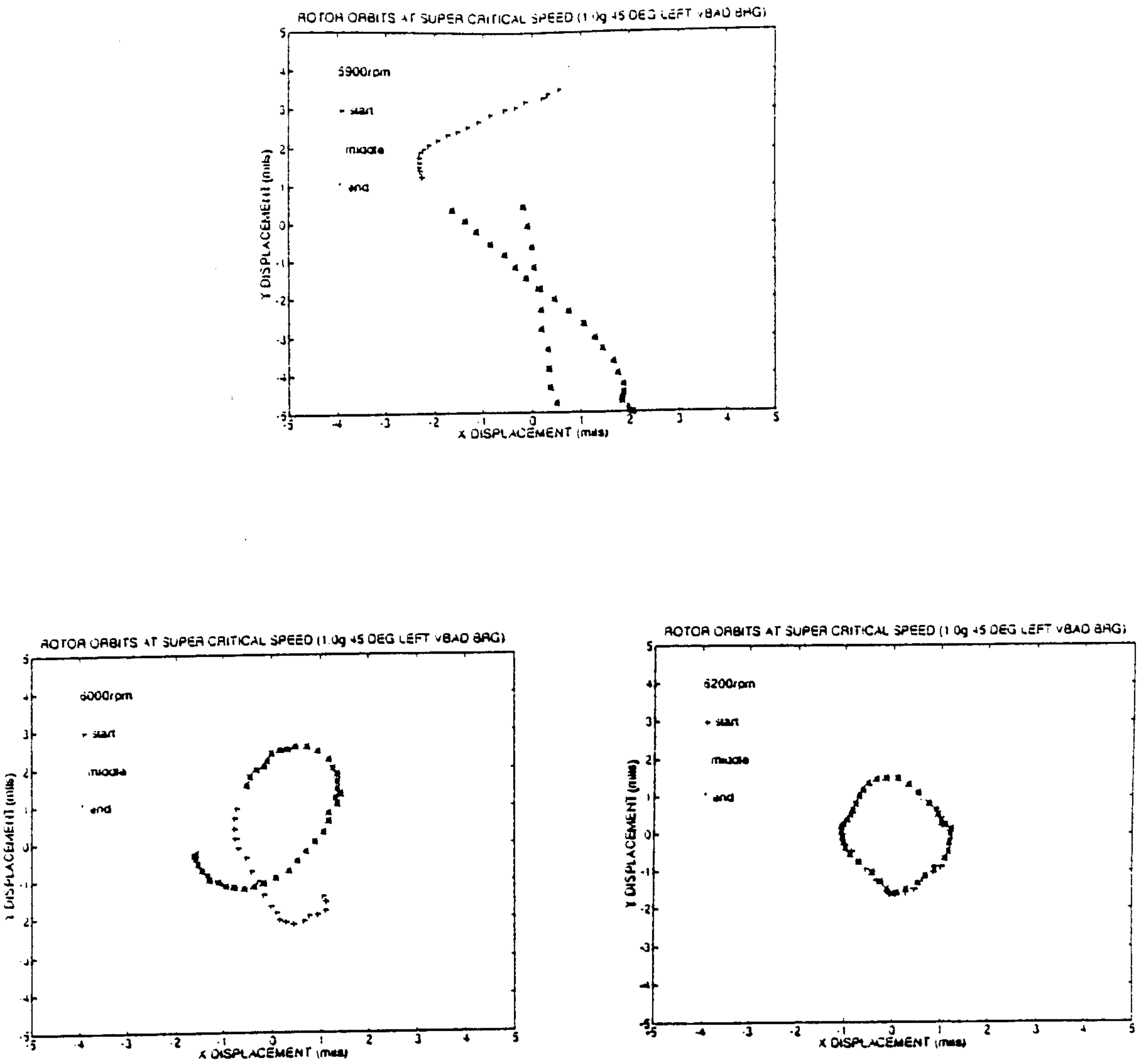

Figure 63. Rotor Orbits 1.0 Gram Imbalance Elongated Bearing with Elongation In the Direction of the Resonant Displacement (45 Degrees off vertical). Speeds from 5900 to 6200 rpm.

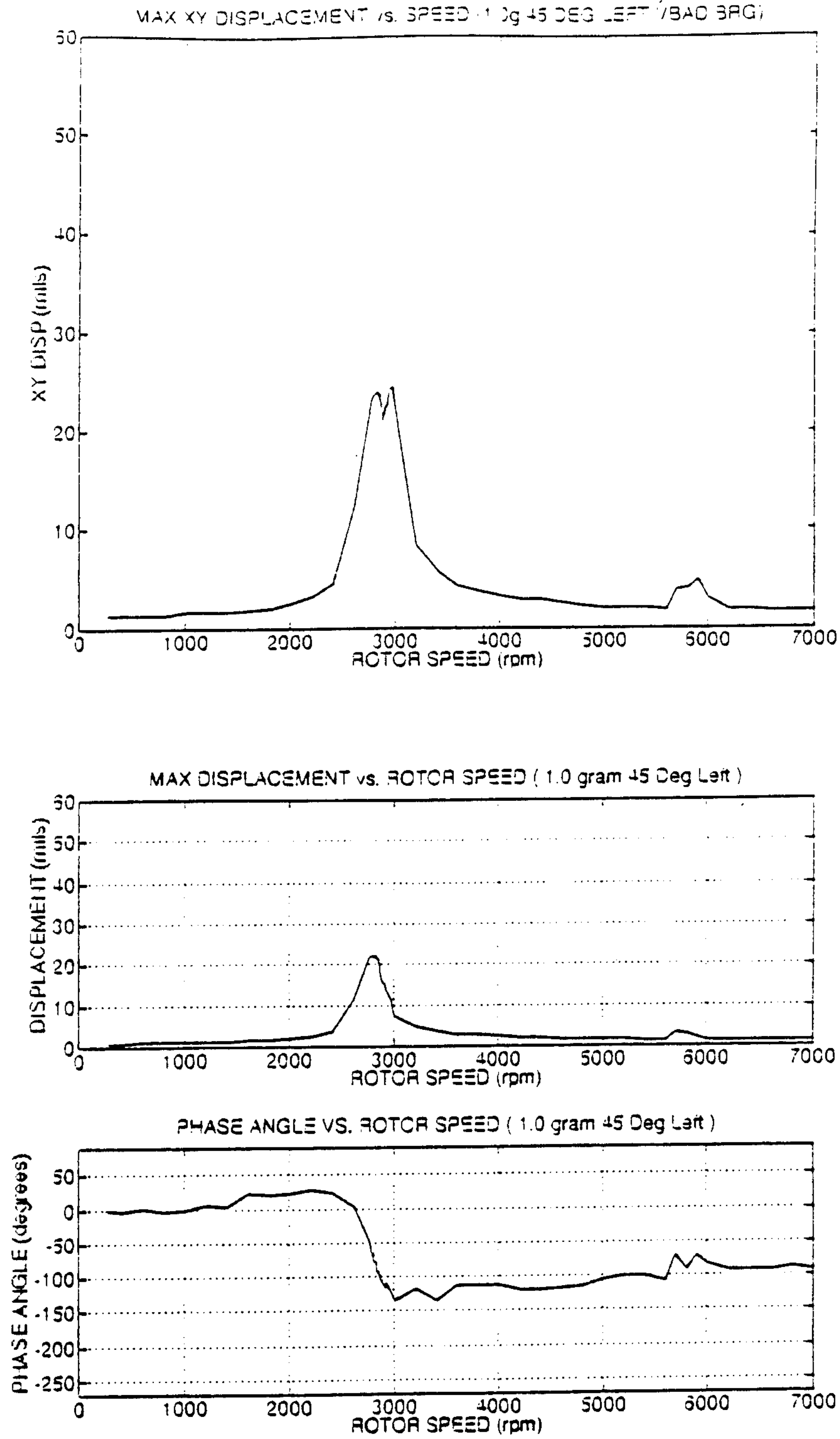

Figure 64. **Maximum Displacements and Bode Plot for 1.0 Gram Imbalance Elongated Bearing with Elongation In the Direction of the Resonant Displacement (45 Degrees off vertical).**

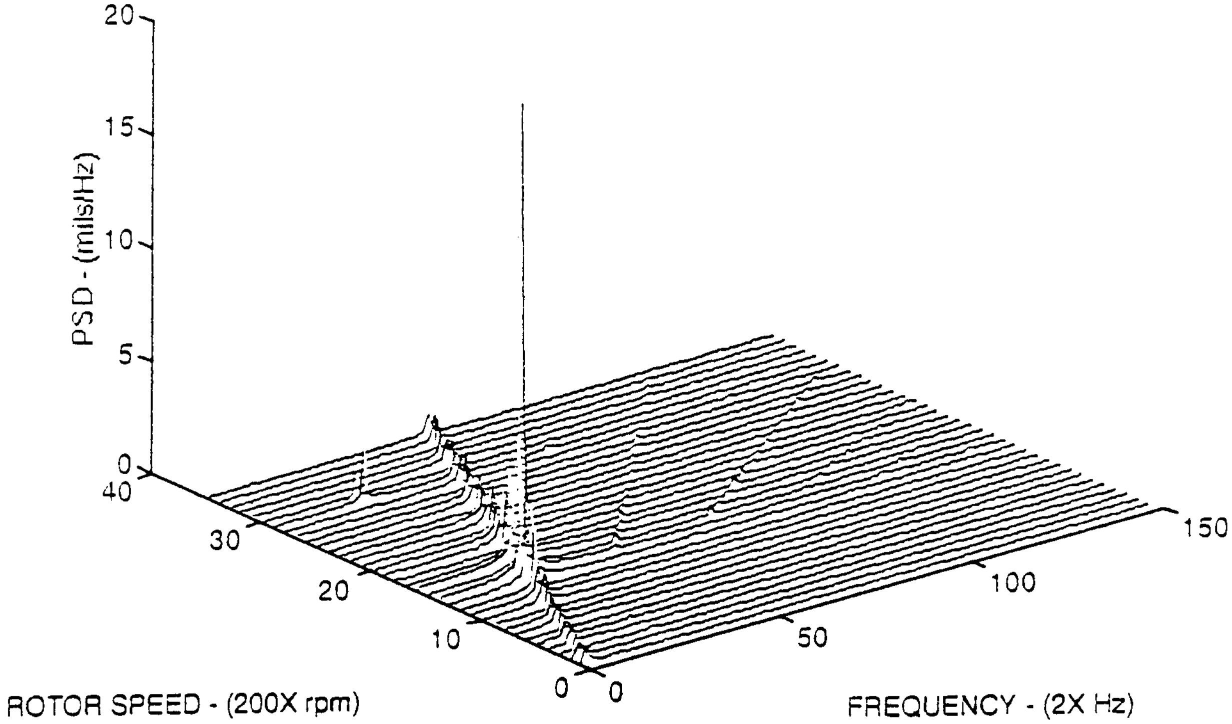

Figure 65. Cascade Plot 1.0 Gram Imbalance Elongated Bearing with Elongation In the Direction of the Resonant Displacement (45 Degrees off vertical).

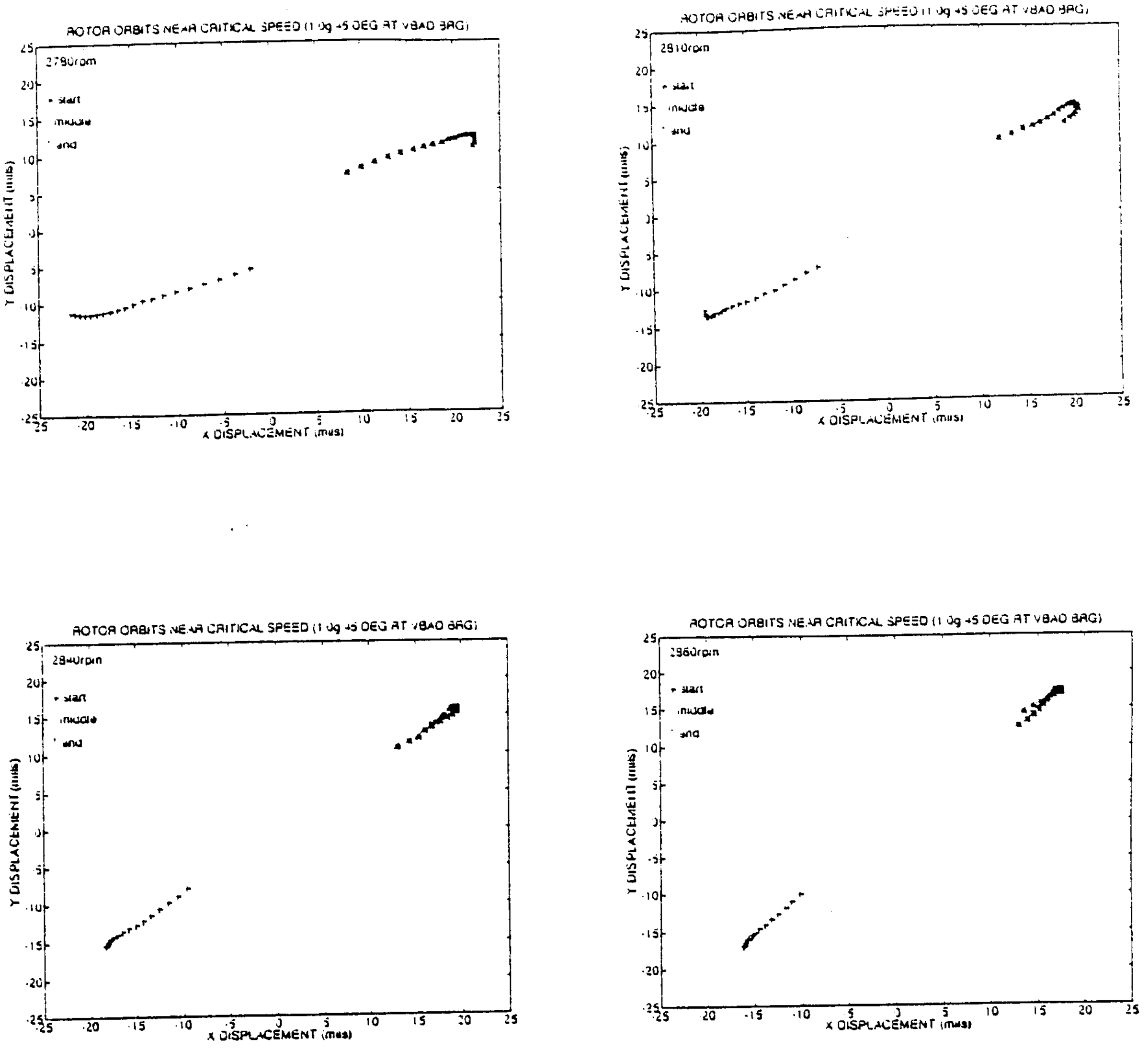

Figure 66. Rotor Orbits 1.0 Gram Imbalance Elongated Bearing with Elongation Perpendicular to Direction of Resonant Displacement (45 Degrees off Vertical). Speeds from 2780 to 2860 rpm.

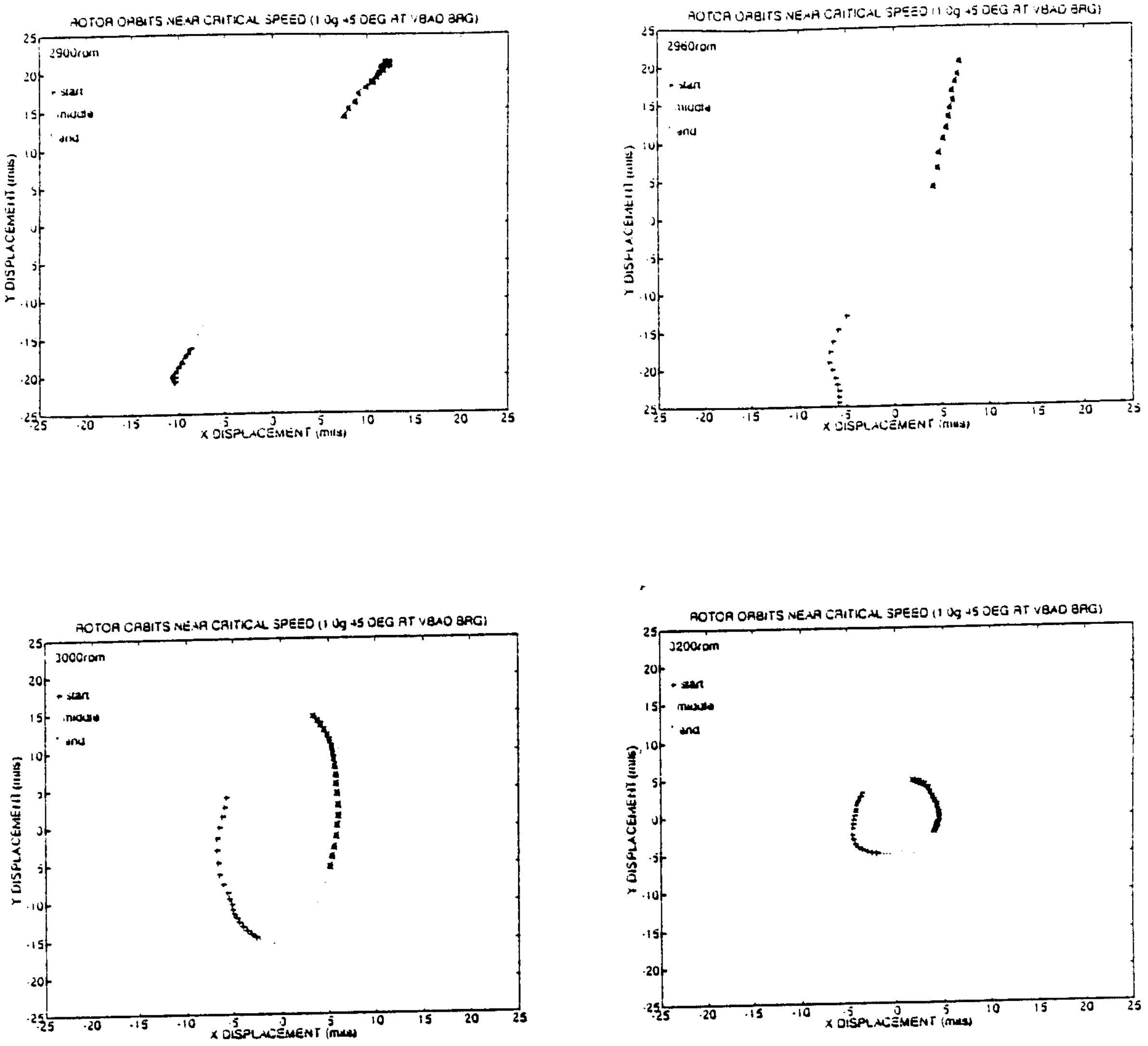

Figure 67. Rotor Orbits 1.0 Gram Imbalance Elongated Bearing with Elongation Perpendicular to Direction of Resonant Displacement (45 Degrees off Vertical). Speeds from 2900 to 3200 rpm.

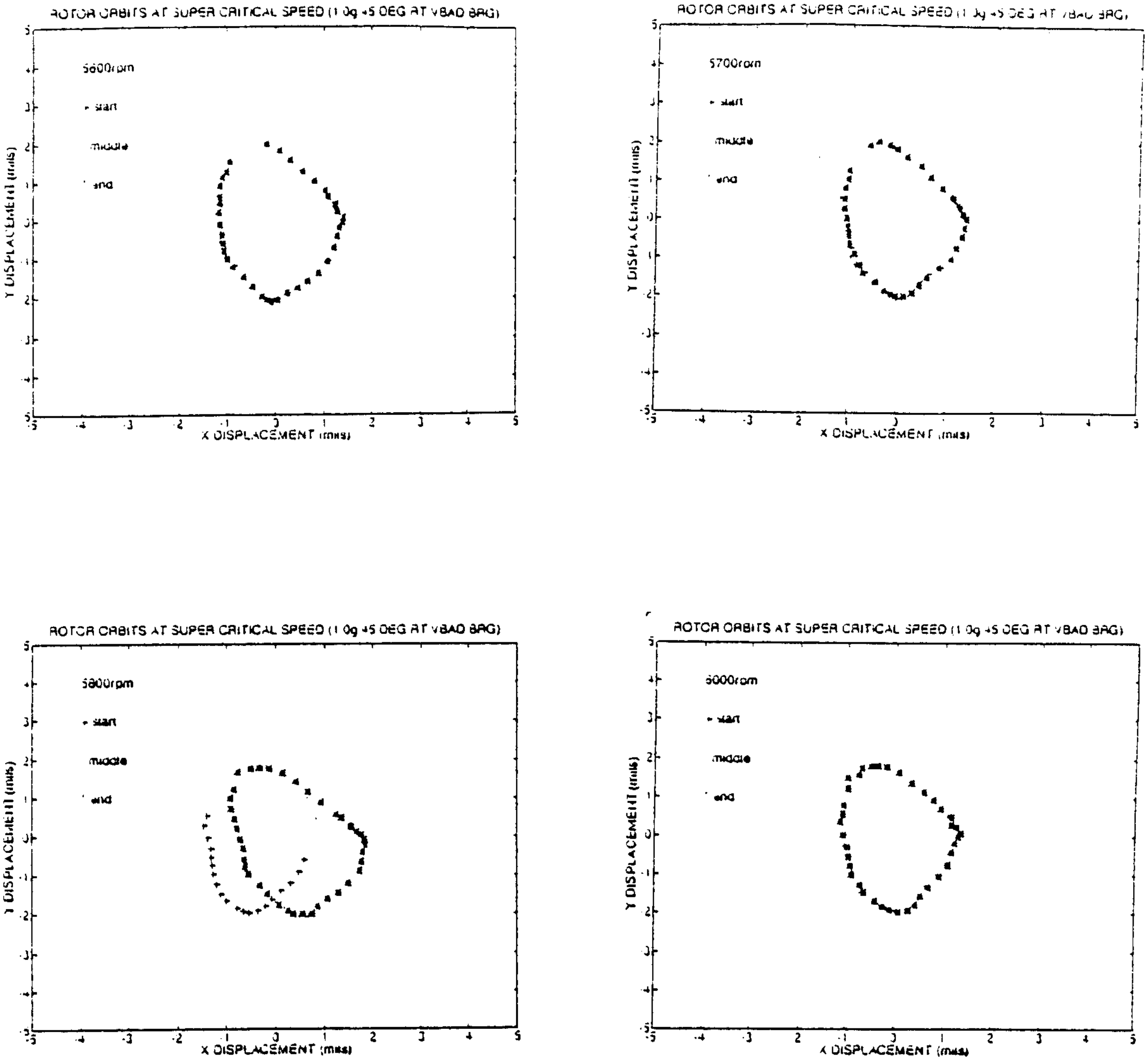

Figure 68. Rotor Orbits 1.0 Gram Imbalance Elongated Bearing with Elongation Perpendicular to Direction of Resonant Displacement (45 Degrees off Vertical). Speeds from 5600 to 6000 rpm.

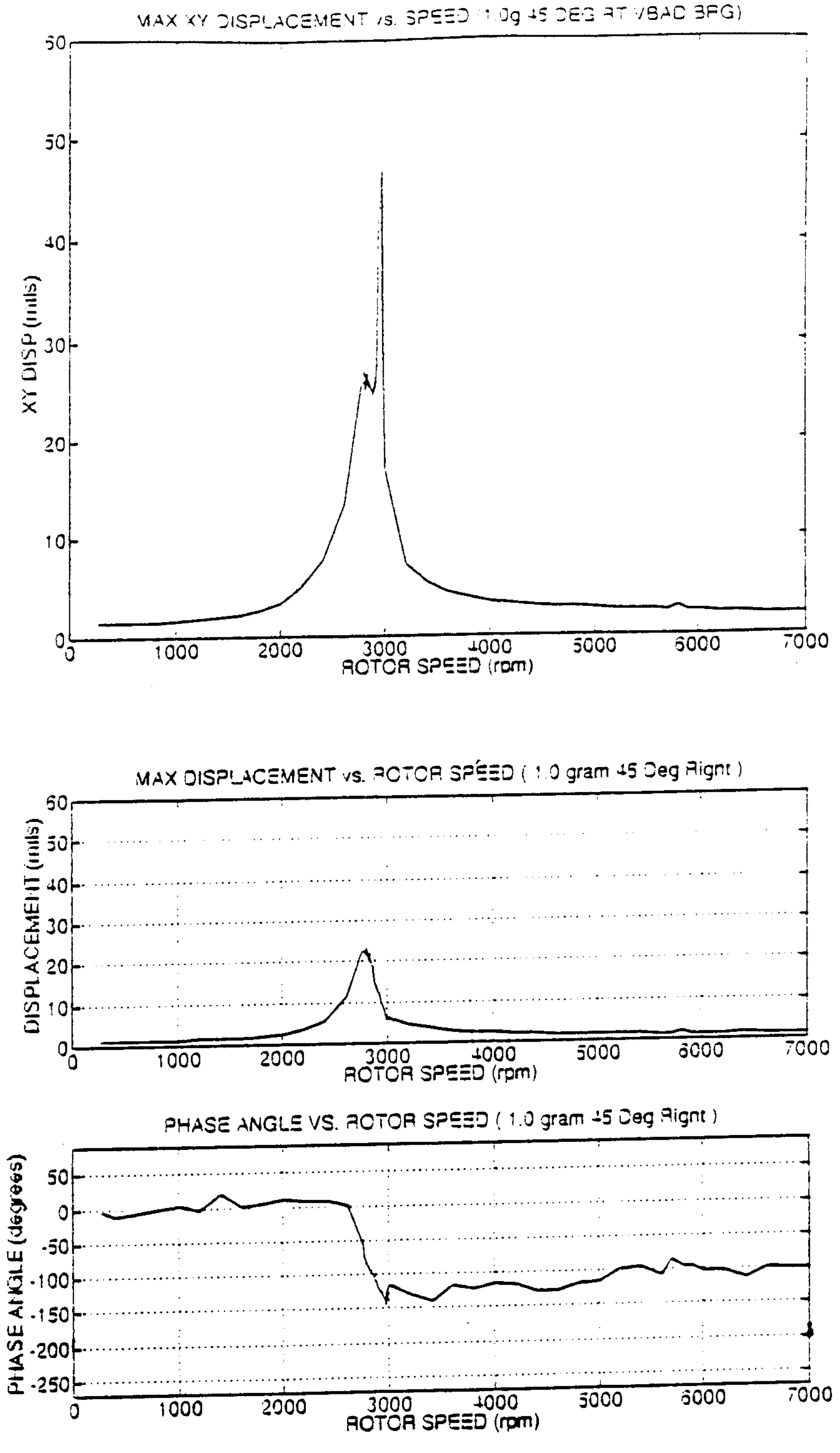

Figure 69. **Maximum Displacements and Bode Plot for 1.0 Gram Imbalance Elongated Bearing with Elongation Perpendicular to Direction of Resonant Displacement (45 Degrees off Vertical).**

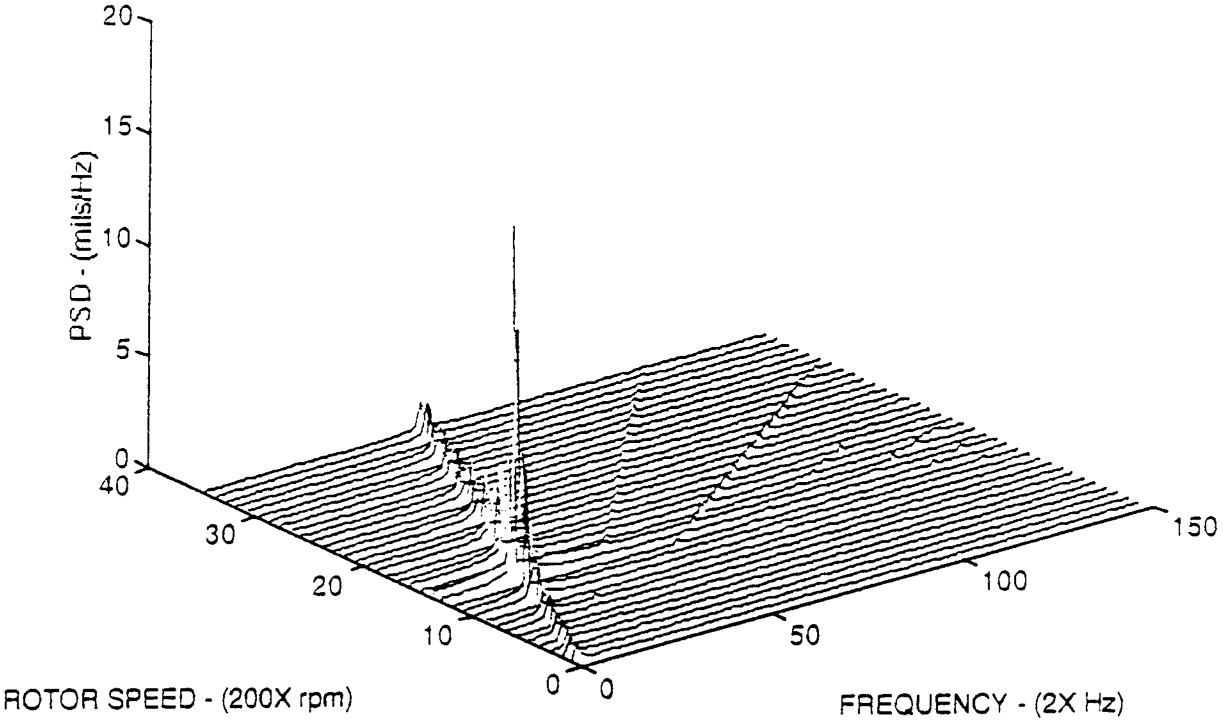

Figure 70. Cascade Plot 1.0 Gram Imbalance Elongated Bearing with Elongation Perpendicular to Direction of Resonant Displacement (45 Degrees off Vertical).

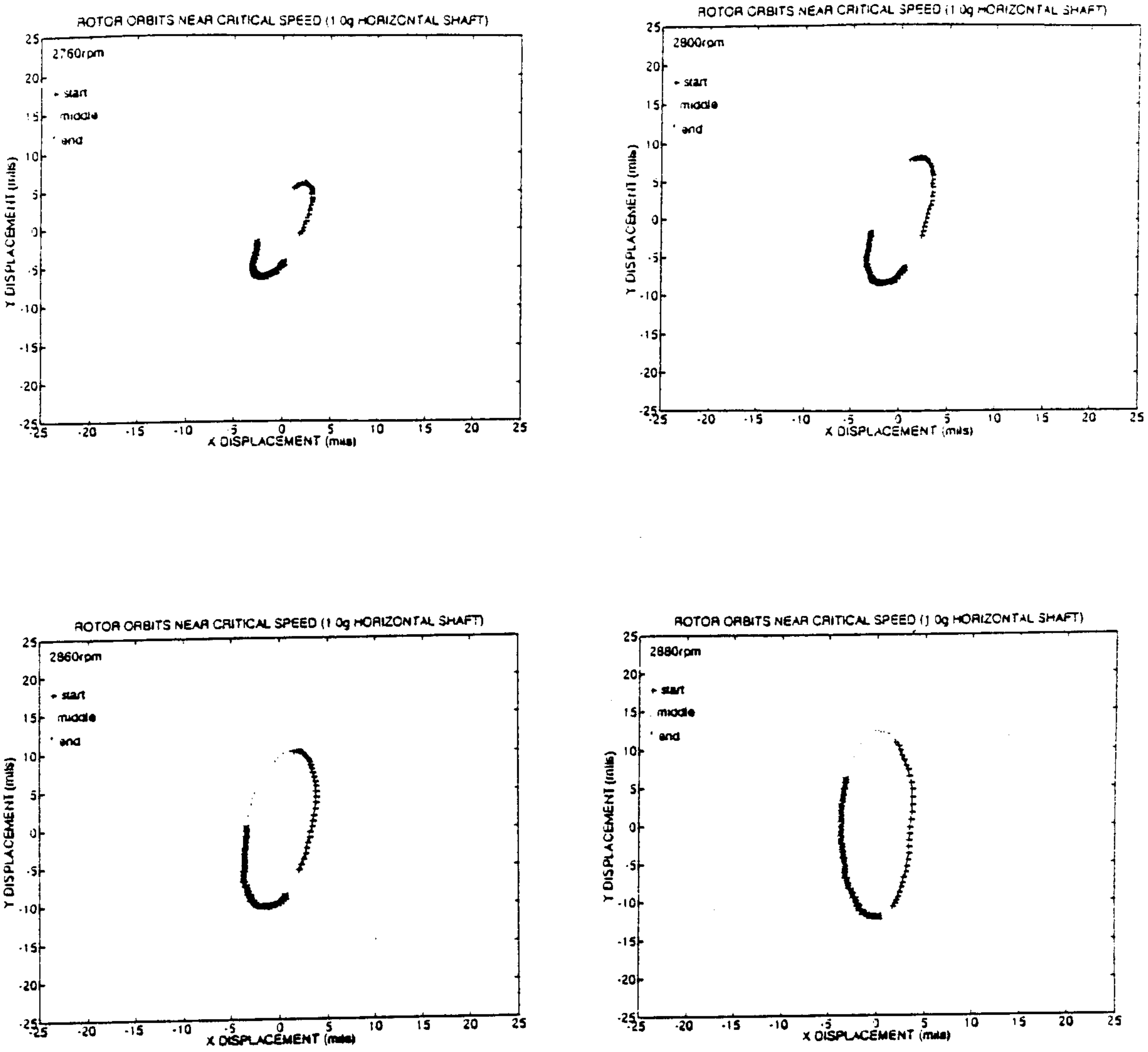

Figure 71. Rotor Orbits 1.0 Gram Imbalance Shaft Mounted Horizontal. Speeds from 2760 to 2880 rpm.

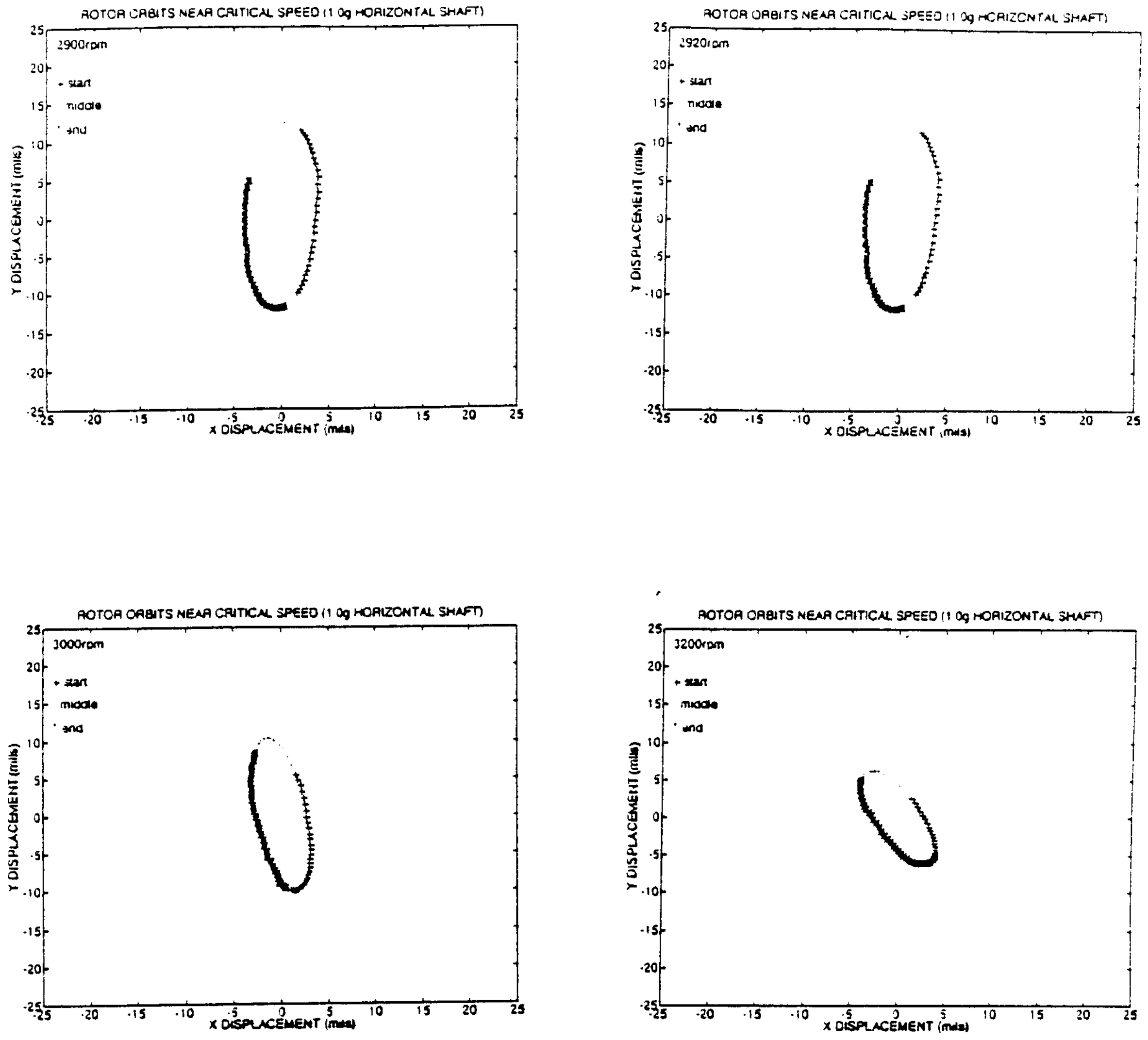

Figure 72. Rotor Orbits 1.0 Gram Imbalance Shaft Mounted Horizontal. Speeds from 2900 to 3200 rpm.

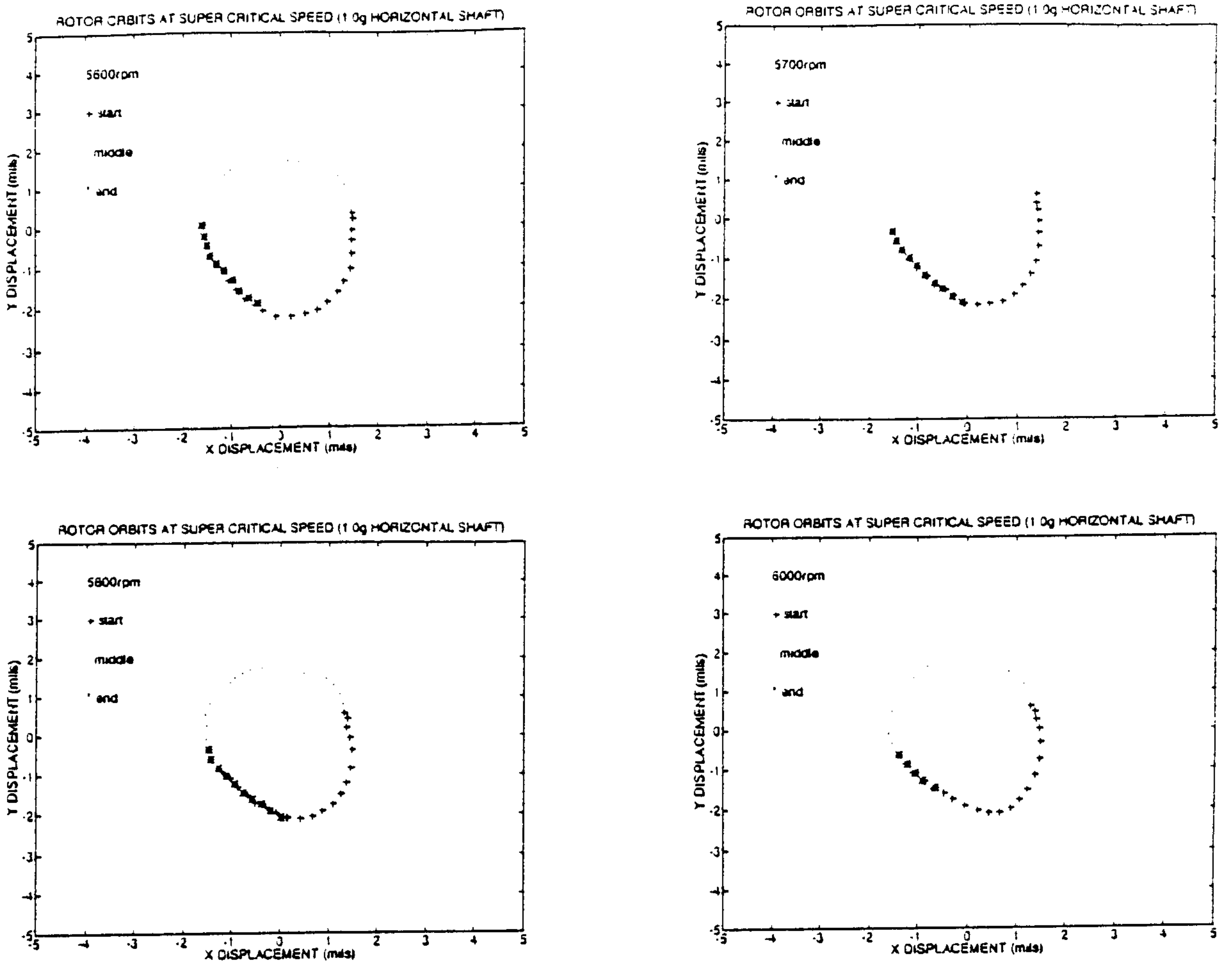

Figure 73. Rotor Orbits 1.0 Gram Imbalance Shaft Mounted Horizontal. Speeds from 5600 to 6000 rpm.

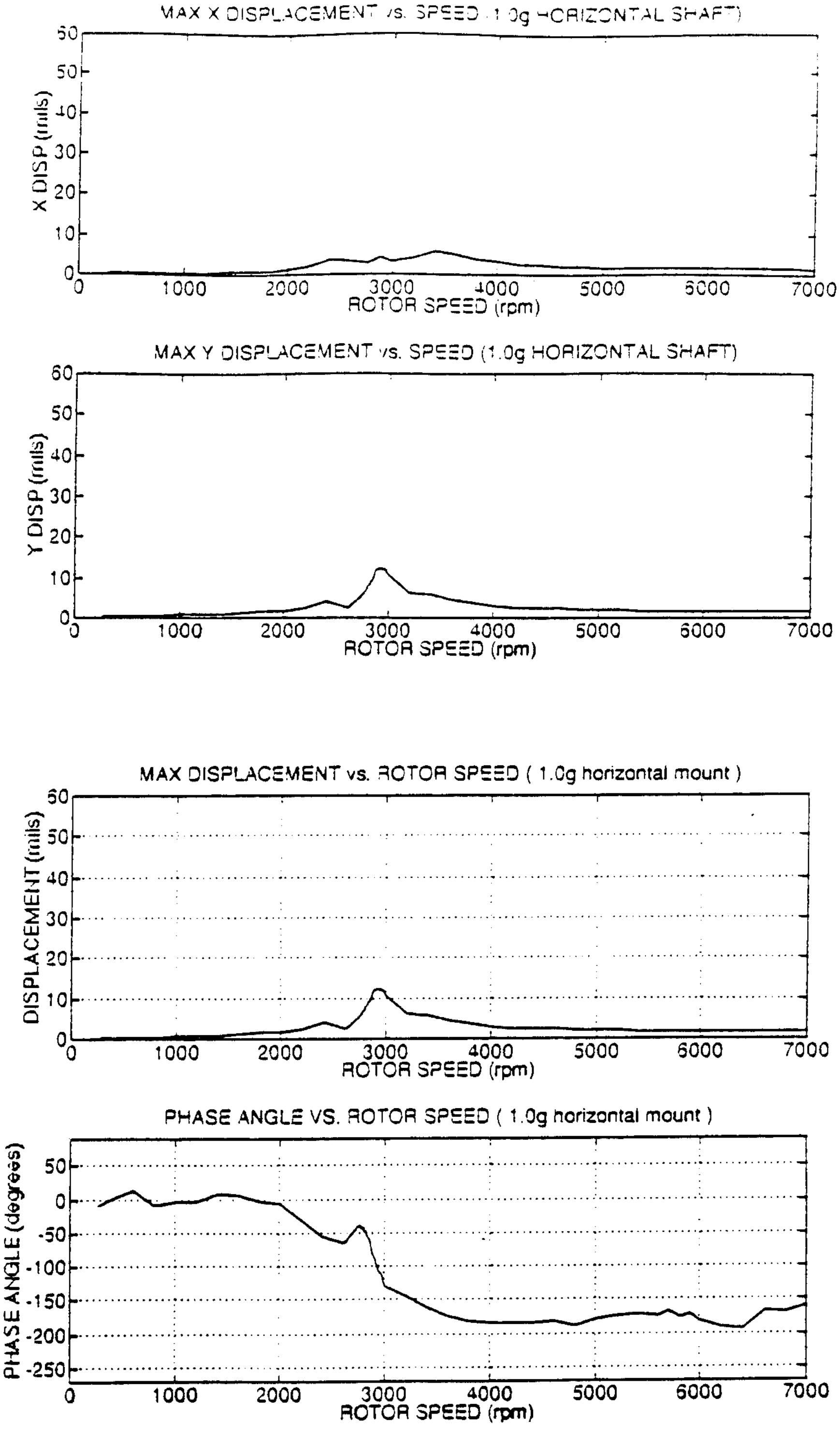

Figure 74. Maximum Displacements and Bode Plot for 1.0 Gram Imbalance Shaft Mounted Horizontal.

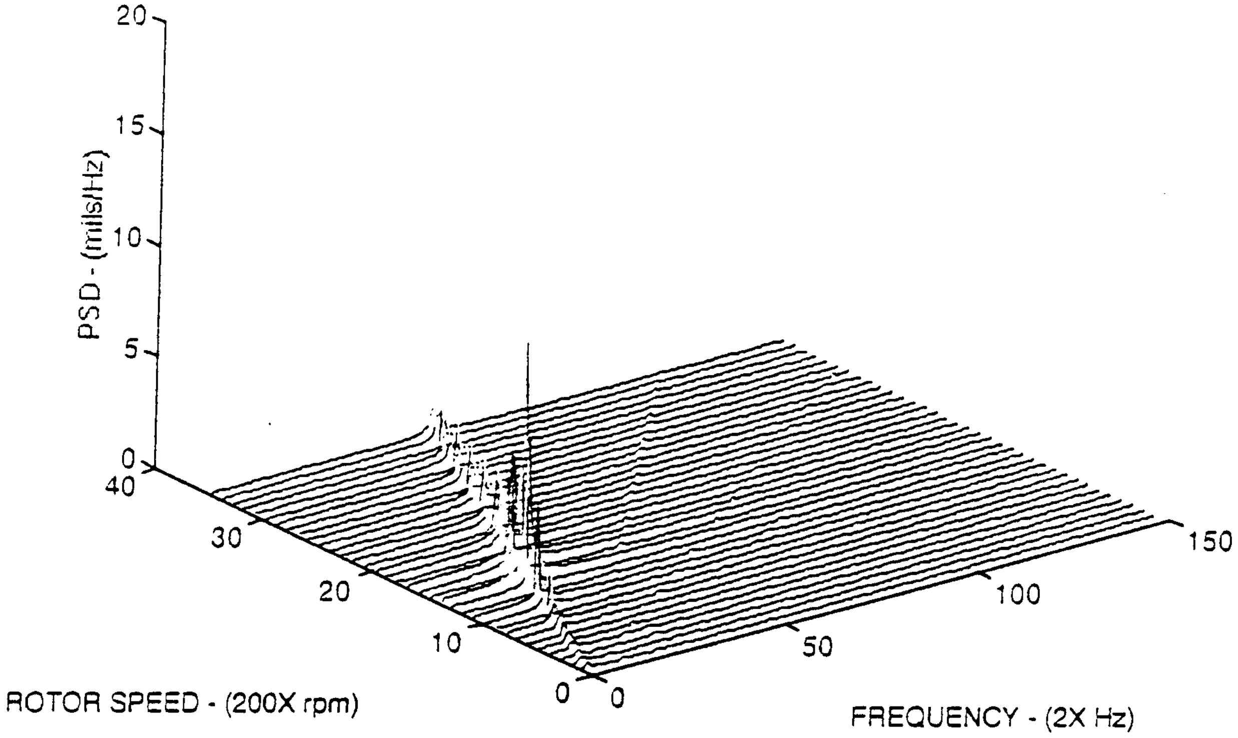

Figure 75. Cascade Plot 1.0 Gram Imbalance Shaft Mounted Horizontal.

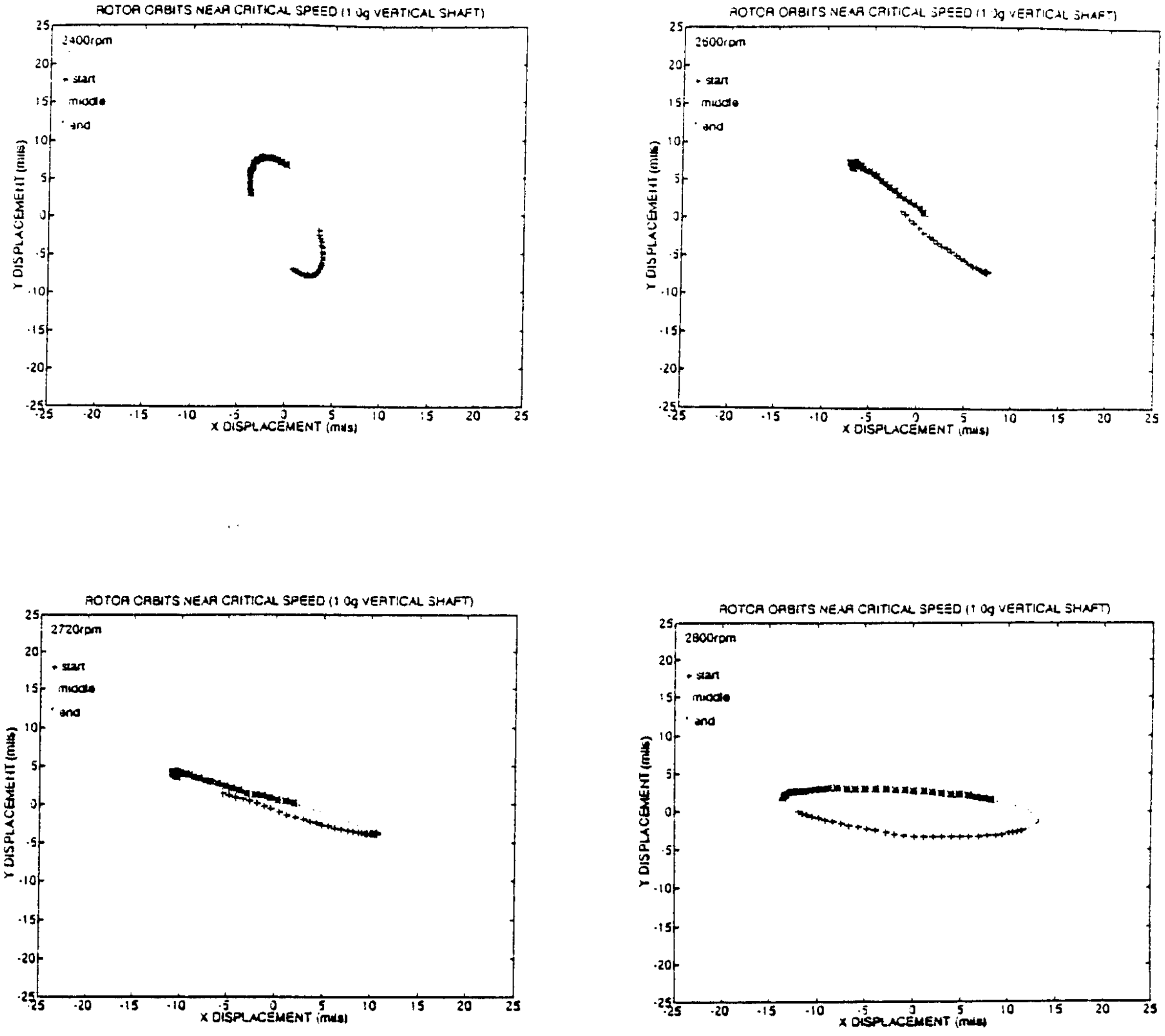

Figure 76. Rotor Orbits 1.0 Gram Imbalance Shaft Mounted Vertical. Speeds from 2400 to 2800 rpm.

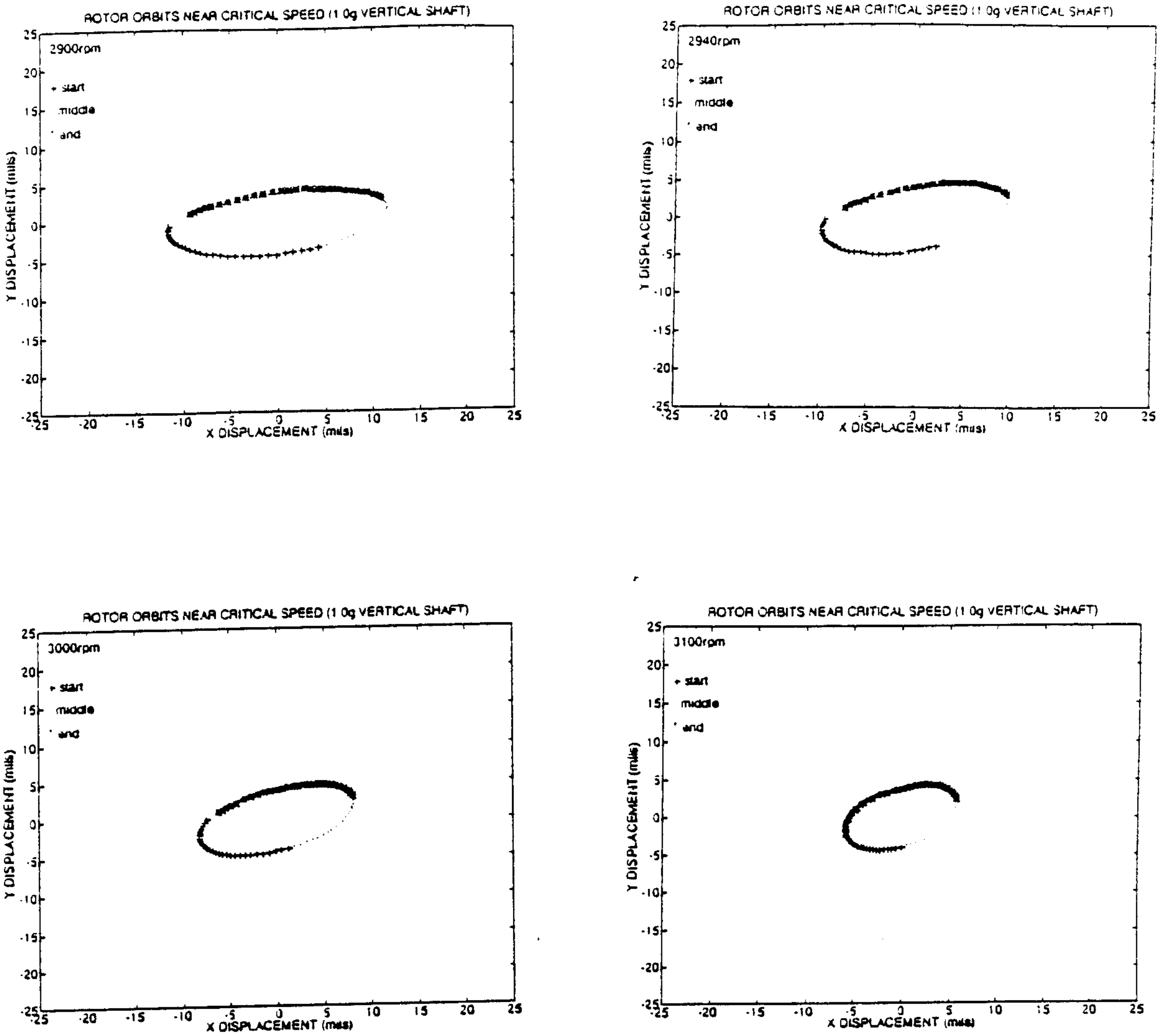

Figure 77. Rotor Orbits 1.0 Gram Imbalance Shaft Mounted Vertical. Speeds from 2900 to 3100 rpm.

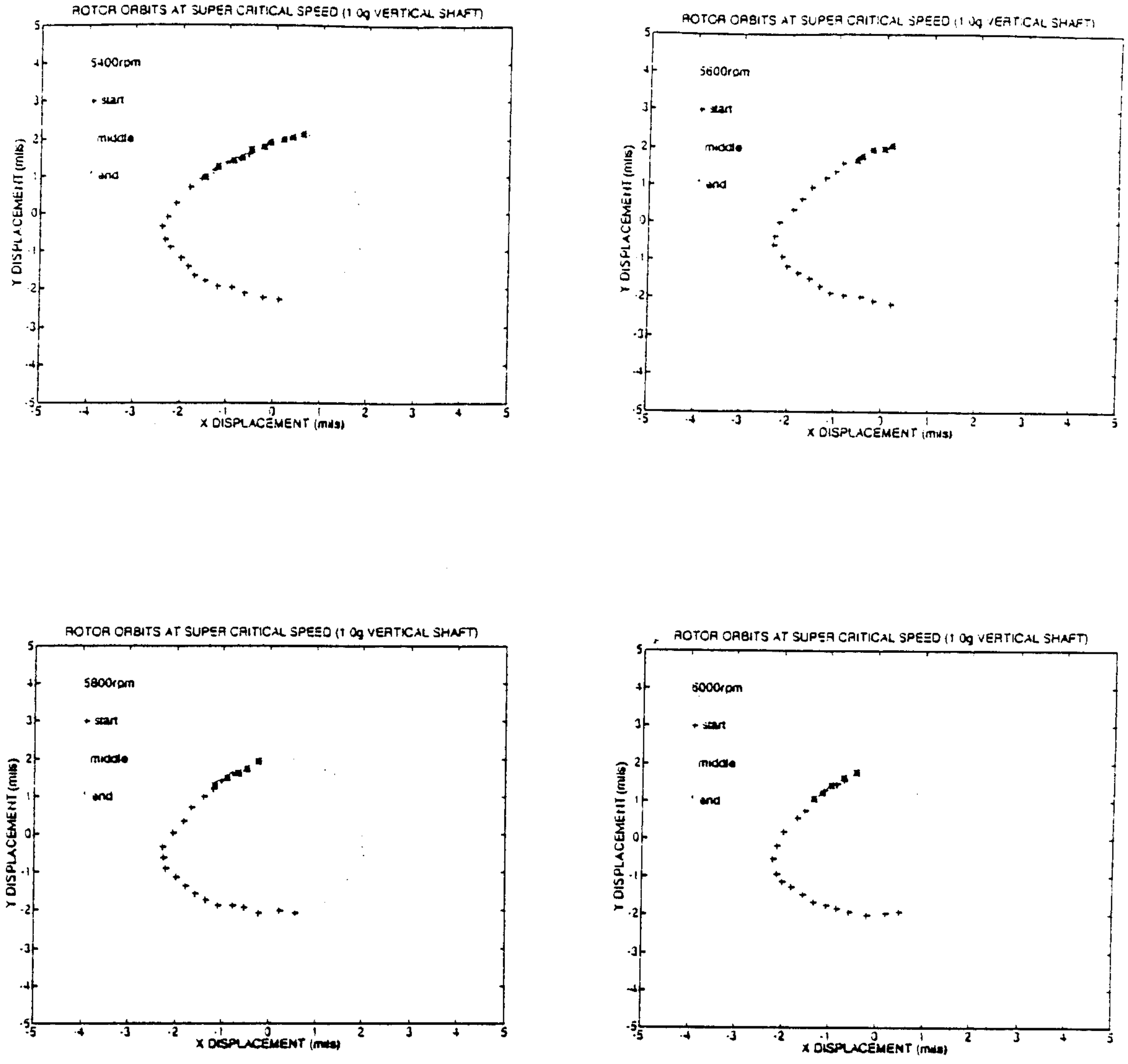

Figure 78. Rotor Orbits 1.0 Gram Imbalance Shaft Mounted Vertical. Speeds from 5400 to 6000 rpm.

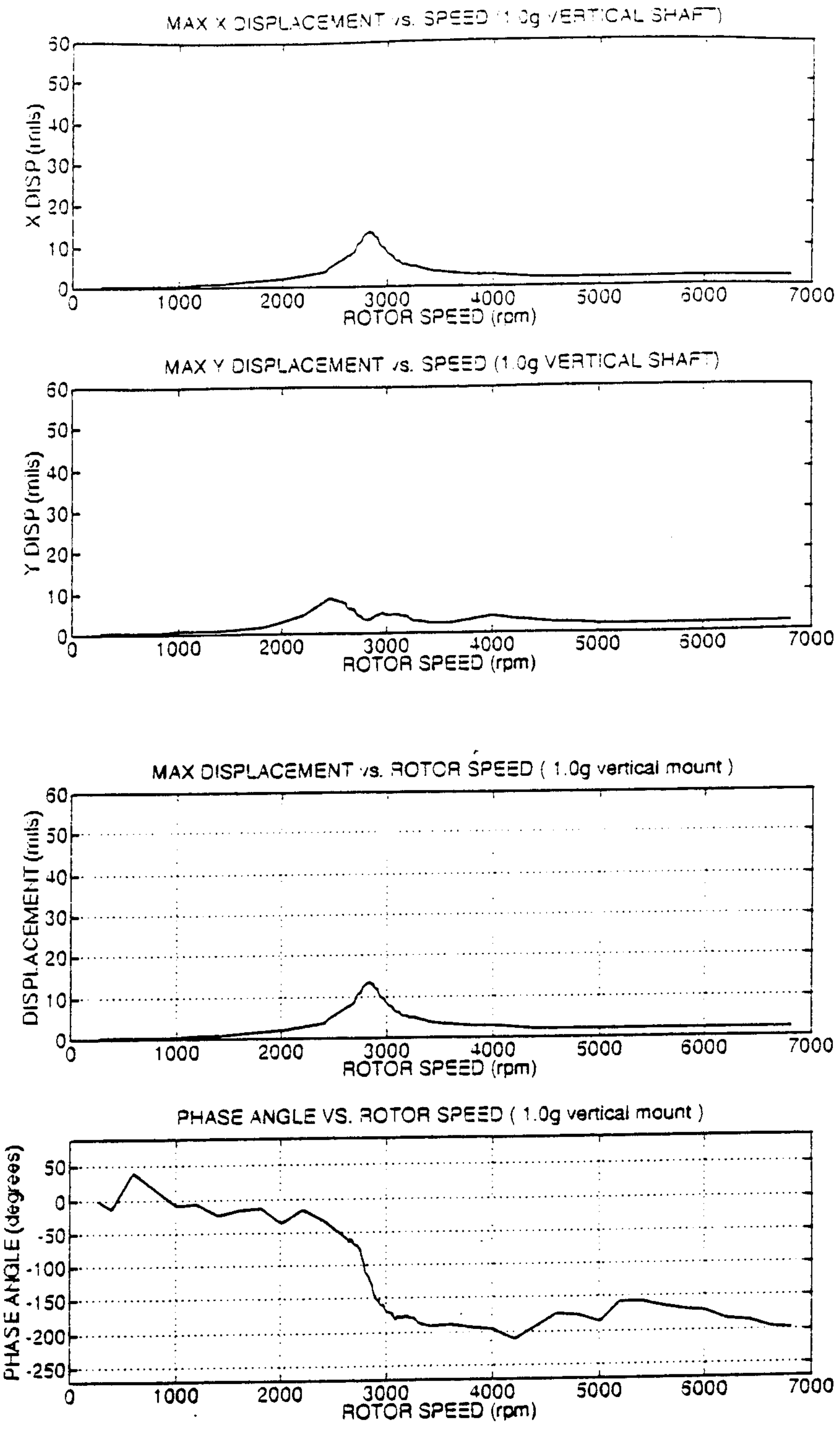

Figure 79. **Maximum Displacements and Bode Plot for 1.0 Gram Imbalance Shaft Mounted Vertical.**

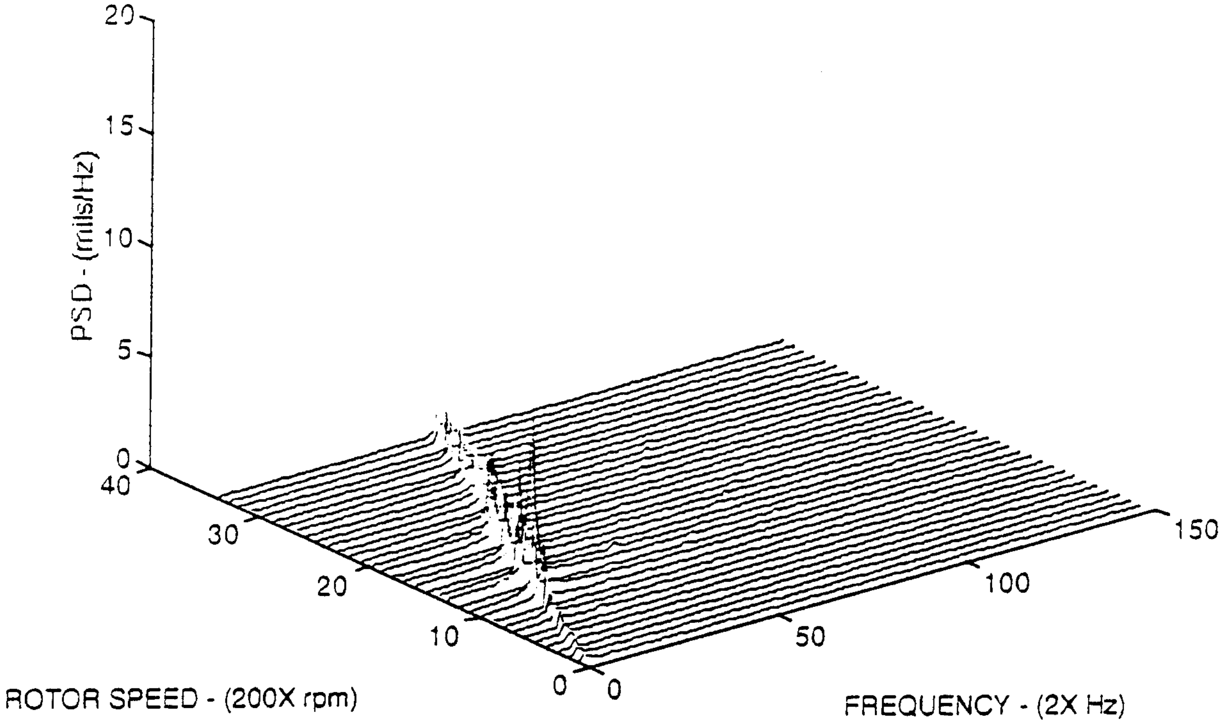

Figure 80. Cascade Plot 1.0 Gram Imbalance Shaft Mounted Vertical.

LIST OF REFERENCES

[Ref. 1] Simei, F.A., "Development of an Experimental Facility for Analysis of Rotordynamic Phenomena," Thesis, March 1994.

[Ref. 2] Vance, J.M., *Rotordynamics of Turbomachinery*, pp. 130-131, John Wiley & Sons, 1988.

[Ref. 3] Rankine, W.A., "On the Centrifugal Force of Rotating Shafts," *London Engineer*, v.27, p.249, 1869.

[Ref. 4] Jeffcott, H. H., "The Lateral Vibration of Loaded Shafts in the Neighborhood of a Whirling Speed - The Effect of Want of Balance," *London Philosophical Magazine,* v. 37, pp. 304-314, 1919.

[Ref. 5] Muszynska, A., "Fundamental Response of a Rotor," report No.1, 1986.

[Ref. 6] James, M. L., and others, V*ibration of Mechanical and Structural Systems,* pp. 89-94, Harper & Row, Publishers, Inc., 1989.

INITIAL DISTRIBUTION LIST

		No. Copies
1.	Defense Technical Information Center Cameron Station Alexandria, Virginia 22304-6145	2
2.	Library, Code 052 Naval Postgraduate School Monterey, California 93943-5101	2
3.	Department Chairman, Code ME Department of Mechanical Engineering Naval Postgraduate School Monterey, California 93943-5000	1
4.	Professor Knox T. Millsaps Jr., Code ME/MI Department of Mechanical Engineering Naval Postgraduate School Monterey, California 93943-5000	4
5.	LT Curtis E. Vejvoda 549 Bonita Dr. Tulare, California 93274	2
6.	Curricular Officer, Code 34 Department of Mechanical Engineering Naval Postgraduate School Monterey, California 93943-5100	1
7.	Naval Sea Systems Command Director, Engines Division (SEA S6X3) Washington D.C. 20362	1
8.	Bentley Nevada Corporation Mr. Don Bentley P.O. Box 157 Minden, Nevada 89423	1

9. Dr. John Vance 1
Department of Mechanical Engineering
Texas A & M University
College Station, Texas 77843-3123